Swansea University E-Theses

Characterisation of CVD diamond for electronic device applications.

Walters, Adrian Stuart

How to cite:

Walters, Adrian Stuart (2002) *Characterisation of CVD diamond for electronic device applications..* thesis, Swansea University.
http://cronfa.swan.ac.uk/Record/cronfa43115

Use policy:

This item is brought to you by Swansea University. Any person downloading material is agreeing to abide by the terms of the repository licence: copies of full text items may be used or reproduced in any format or medium, without prior permission for personal research or study, educational or non-commercial purposes only. The copyright for any work remains with the original author unless otherwise specified. The full-text must not be sold in any format or medium without the formal permission of the copyright holder. Permission for multiple reproductions should be obtained from the original author.

Authors are personally responsible for adhering to copyright and publisher restrictions when uploading content to the repository.

Please link to the metadata record in the Swansea University repository, Cronfa (link given in the citation reference above.)

http://www.swansea.ac.uk/library/researchsupport/ris-support/

Characterisation of CVD Diamond for Electronic Device Applications

By

Adrian Stuart Walters, B.Eng. (Hons.), M.Phil.

A Thesis Submitted to the University of Wales for admittance to the Degree of Doctor of Philosophy

Department of Materials Engineering
University of Wales, Swansea

2002

ProQuest Number: 10821507

All rights reserved

INFORMATION TO ALL USERS
The quality of this reproduction is dependent upon the quality of the copy submitted.

In the unlikely event that the author did not send a complete manuscript
and there are missing pages, these will be noted. Also, if material had to be removed,
a note will indicate the deletion.

ProQuest 10821507

Published by ProQuest LLC (2018). Copyright of the Dissertation is held by the Author.

All rights reserved.
This work is protected against unauthorized copying under Title 17, United States Code
Microform Edition © ProQuest LLC.

ProQuest LLC.
789 East Eisenhower Parkway
P.O. Box 1346
Ann Arbor, MI 48106 – 1346

UNIVERSITY OF
LIBRARY
WALES SWANSEA

DECLARATIONS

Statement 1 – This work has not previously been accepted in substance for any degree and is not concurrently submitted in candidature for any degree.

Signed .... (A. Walters – candidate)
Date 30.4.02..........

Statement 2 – This thesis is the result of my own investigations, except where otherwise stated. Other sources are acknowledged by explicit references. A bibliography is appended.

Signed .... (A. Walters – candidate)
Date 30.4.02..........

Statement 3 – I hereby give consent for my thesis if accepted, to be available for photocopying and inter-library loan, and for the title and summary to be made available to outside organisations.

Signed .... (A. Walters – candidate)
Date 30.4.02..........

ACKNOWLEDGEMENTS

First, I would like to thank my supervisor, Prof. Joe Marshall, without whom the project would not have been possible. His support, guidance and inspiration have been invaluable throughout the course of this program.

Next, I must pay tribute to De Beers Industrial Diamond Division Limited, who have not only provided more than ample quantities of CVD diamond material but have also funded the research contained in this thesis. In particular, I would like to mention Dr Andrew Whitehead, my principle contact at De Beers.

Finally, special thanks to Mum, Dad and Sara, for all your support and encouragement throughout my studies, without which this document surely would not exist.

ABSTRACT

The unique combination of physical properties displayed by the arrangement of carbon atoms recognised as diamond has fascinated scientists for hundreds of years. The electronic properties in particular are significantly superior to conventional semiconducting materials in most instances. Sadly, the currently limited supply of device quality single crystal material makes commercial production of diamond based electronic components unviable at present. Nevertheless, recent advances in the production of synthetic diamond via chemical vapour deposition (CVD) have stimulated great interest in this as a source of electronic grade material. However, in optimising the material for device applications detailed information is often required concerning the properties of the localised defect states located within the energy gap. Although there is currently significant data concerning the mid-gap states, little has been published with respect to the shallower centres that are often responsible for limiting carrier drift mobility and associated electronic properties. This study presents the first detailed exploration of the presence and influence of such shallow states from the analysis of transient photoconductivity (TPC) measurements. It is demonstrated that such procedures provide a powerful method for the study of the localised states in CVD diamond and related materials. In particular, measurements show that even in very good quality CVD diamond films, an energetically broad but structured collection of localised states exists. The energy distributions of these localised states have been calculated by employing techniques developed, refined and proven in prior studies of disordered semiconductors. During the course of the TPC studies it was observed that specimens exposed to an applied field can accumulate a significant space-charge related residual field. Clearly, this could have a considerable impact to the operation of many potential devices. Consequently, a new variant of the TPC system was developed to allow the decay of this field to be monitored as a function of time following the removal of the applied voltage. Such data provide further information concerning the localised state distribution in which the space-charge is trapped, and are demonstrated to be at least qualitatively consistent with the distributions calculated from the TPC measurements.

CONTENTS

TITLE I

DECLARATIONS II

ACKNOWLEDGEMENTS III

ABSTRACT IV

CONTENTS V

1 INTRODUCTION **1-1**

References *1-4*

2 DIAMOND - PROPERTIES, PRODUCTION & APPLICATIONS **2-1**

2.1 History of Diamond *2-1*

2.2 Chemistry of Diamond *2-2*

2.3 Structure of Diamond *2-2*

2.4 Physical Properties of Diamond *2-8*

2.5 Early Attempts at Diamond Synthesis *2-17*

2.6 High-Pressure High-Temperature (HPHT) Diamond Synthesis *2-21*

2.7 Chemical Vapour Deposition (CVD) Diamond *2-25*

References *2-35*

3 ELECTRONIC TRANSPORT IN SEMICONDUCTORS **3-1**

3.1 Introduction to Band Theory *3-1*

3.2 Conduction in Crystalline Semiconductors *3-5*

3.3 Direct and Indirect Band Gap Semiconductors *3-6*

3.4 Recombination and Trapping *3-8*

3.5 Band Structure of Non-Crystalline Semiconductors *3-9*

3.6 Conduction in Non-Crystalline Semiconductors *3-12*

References *3-17*

4 CHARACTERISATION AND ANALYSIS TECHNIQUES **4-1**

4.1 Transient Photoconductivity in Crystalline Semiconductors *4-1*

4.2 Transient Photoconductivity in Non-Crystalline Semiconductors *4-5*

4.3 Interpretation Techniques *4-7*

References *4-12*

5 EXPERIMENTAL PROCEDURES **5-1**

5.1 Specimen Preparation *5-1*

5.2 Transient Photoconductivity Measurements *5-2*

5.3 Residual Space-Charge Field Measurements *5-4*

References *5-6*

6 EXPERIMENTAL RESULTS **6-1**

6.1 Transient Photoconductivity Results *6-1*

6.2 Residual Space-Charge Field Results *6-17*

References *6-18*

7 DISCUSSION **7-1**

7.1 Transient Photo-Response *7-1*

7.2 Residual Field *7-16*

References *7-22*

8 CONCLUSIONS **8-1**

References *8-4*

9 SCOPE FOR FURTHER INVESTIGATION **9-1**

References *9-5*

APPENDIX 1: List of Publications **A1-1**

BIBLIOGRAPHY **B-1**

1 INTRODUCTION

The analysis of transient photoconductivity data by various techniques (described in subsequent sections) has now been developed to such an extent that detailed information regarding the electronic properties of a semiconducting material can be obtained. Of particular importance, data can be extracted regarding charge carrier mobilities and lifetimes and the nature, concentration and distribution of localised states that control these parameters [1]. Using the time-of-flight (TOF) method [2], excess free charge carriers are generated close to the surface of the semiconductor, usually by illumination from a suitable source (e.g. a dye-laser) and their progress through the material is observed by recording the photocurrent decay. Information concerning the interaction of these carriers with the defect-related localised states (of varying depth and spatial location) during transit is contained within the decay of the transient photocurrent. As a result, transient photoconductivity measurements using the TOF configuration are now an accepted method for determining carrier mobility, capture cross-section and the density/distribution of localised states [3]. Additionally, electrons or holes can be investigated separately, depending on the polarity of the applied field.

The results of this analysis, although of substantial scientific interest, also have considerable commercial importance in the present context, as the properties of diamond potentially make it an excellent engineering material for the next generation of electronic and opto-electronic devices [4]. In particular, diamond displays high free-carrier mobilities, wide intrinsic bandgap, very high electrical breakdown

strength and excellent thermal, mechanical, optical and chemical properties. Already, prototype devices have been produced in various laboratories for high temperature/power applications, particle/radiation detection, and visible-blind UV detection. As natural diamond is restricted for these applications by cost and size limitations, it has become necessary to develop processes capable of producing suitable dimensions of electronic grade synthetic diamond at a reduced cost.

Chemical vapour deposition (CVD) has proved an excellent option for this application, and it is currently possible to produce thick (several mm) large area (>10 cm diameter) specimens [5] displaying excellent optical, thermal, mechanical and chemical properties. Additionally, it is possible to control the semiconducting properties of the material by the addition of dopant gases during the synthesis process [6] enabling the production of either p-type or n-type semiconducting diamond (although a useful n-type material for semiconductor device applications is still beyond present production processes). However, to date the commercial use of CVD diamond has been limited, restricted mainly to thermal management and optical applications. A potential limitation of CVD diamond for electronic device applications is that it is normally a polycrystalline material (unless a single-crystal diamond substrate is used for deposition) and will always contain at least small amounts of impurities and defects resulting in the formation of localised states, which can have a marked effect on carrier mobilities and lifetimes.

In addition to the limitation described above, diamond is not suitable for all semiconductor applications as it is an indirect bandgap material and does not lase.

Additionally, conventional semiconductors such as silicon and gallium arsenide have well developed markets and highly advanced technology that will be difficult to compete with on a commercial basis. Also, CVD diamond will be required to contend with new advances in high performance semiconductors such as SiC, which are easier and less expensive to produce.

Via the analysis of transient photoconductivity and related data, this study aims to obtain a detailed understanding of the concentration, character and energy distribution of the defect states in CVD diamond. For comparison, the properties of high-pressure high-temperature (HPHT) synthetic diamond have also been investigated using the same techniques. However, due to the current increased cost and size restrictions of device quality HPHT over CVD diamond, it is believed unsuitable for commercial production of electronic devices at this time.

References

[1] Marshall J M (1983) *Reports on Progress in Physics* **46** 1235-1282.

[2] Spear W E (1968) *Journal of Non-Crystalline Solids* **1** 197-214.

[3] Pang Y S, Chan S M, Jackman R B, Johnston C, Chalker P R (1997) *Applied Physics Letters* **70** (3) 339-341.

[4] Mainwood A (1998) *Diamond and Related Materials* **7** 504-509.

[5] Chan S M, McKeag R D, Whitfield M D, Jackman R B (1996) *Phys. Stat. Sol. (a)* **154** 445-454.

[6] Koizumi S, Teraji T, Kanda H (2000) *Diamond and Related Materials* **9** 935-940.

[7] Vandevelde T, Nesladek M, Meykens K, Quaeyhaegens C, Stals L M, Gouzman I, Hoffman A (1998) *Diamond and Related Materials* **7** 152-157.

[8] Marshall J M, Walters A S (1999) *Diamond and Related Materials* **8** 2118-2126.

2 DIAMOND - PROPERTIES, PRODUCTION & APPLICATIONS

The following chapter provides background information regarding diamond as an engineering material. Included is an overview of the history and properties of the bulk material and a description of how modern synthesis processes were developed based on unsuccessful attempts as long ago as ~1800! The final sections detail the development of polycrystalline diamond by the chemical vapour deposition process and outline the properties of this relatively new material.

2.1 History of Diamond

It is impossible to pinpoint exactly how long diamond has been regarded as a desirable material. Ancient texts tend to be fragmented and unreliable. Some of the earliest dependable documents pertaining to diamonds are reported to be some sixth century AD Indian manuscripts detailing the procedure for valuing diamonds. However, this implies that diamond trading was well established at this time and some observers [1] have suggested that the documents describe the state of knowledge from up to a thousand years earlier! In addition to the difficulties described above, the word 'diamond' may not mean the same today as in ancient times when the technology did not exist for unambiguous classification of minerals. Today, as detailed below, the word 'diamond' refers to one specific element (carbon) in one specific crystallographic structure.

2.2 Chemistry of Diamond

Diamond chemistry is relatively straightforward. Diamond is made from carbon, ideally 100% carbon. However, when a natural diamond is burnt it produces around only 99% CO_2, the remaining 1% is caused by impurities within the crystal. Although only present in minute amounts, these impurities, as we shall see, can have a radical effect on the properties of diamond.

The burning experiments described above began as early as 1694 by G Averani and C A Targioni [2]. Similar experiments were repeated by Isaac Newton (around 1800), Antoine-Laurent Lavoisier (1772) [3], Smithson Tennant (1797) [4] and others during the 18th century. As a result, by 1900 the consensus was that diamonds were predominantly made from carbon.

2.3 Structure of Diamond

By 1900, graphite was also known to be composed of carbon and it had been suggested by W Allen and W H Pepys [5] that the difference between diamond and graphite was in the *'state of aggregation of their particles'* or more commonly, the atomic structure.

How are the atoms arranged in diamond? The first indication of the atomic structure of diamond was obtained from the shape of natural diamonds, which are often tetrahedral or octahedral in shape. But it was not until 1912 when William Henry Bragg and his son William Lawrence Bragg developed X-ray diffraction that the question began to be answered. W L Bragg realised that X-ray diffraction by a crystal

could only occur due to reflection of the rays from the planes of atoms within a crystal. The rays could only be deflected at certain angles dependent on their wavelength and the distance between the atomic planes. Therefore, measurement of the angles of reflection led to a straightforward calculation of the distance between the atomic planes. From this, the Braggs were able to deduce that every atom was at the centre of a tetrahedron of four other atoms and that diamond was a vast organic molecule composed solely of carbon atoms.

However, this still did not resolve whether natural diamonds should have a tetrahedral or octahedral structure. The answer lay in the way the atoms would bond together - different in each case. The tetrahedral system would require each atom to be aligned along an axis running through the crystal to produce the top and bottom nature of the crystal. The octahedral system in comparison would have no such alignment. The advent of wave mechanics in the 1930's provided the solution when it was discovered that electron orbitals of atoms do not carry over directly into molecules in the bond. Instead atomic orbitals merge to form hybrid (sp^3) orbitals. This allows the carbon atom to make four identical bonds with four neighbouring atoms. There is no asymmetry and diamonds are therefore expected to be octahedral in structure.

However, in 1944 Chandrasekhara Venkata Raman proposed that diamonds could exist with atoms bonded together in four different ways. This theory was developed to explain the results of a survey of thousands of diamonds by R Robertson, J J Fox and A E Martin [6]. The study showed that some diamonds were transparent to

certain wavelengths of infrared radiation (8 μm) while others were opaque. Additionally, it was noted that almost all diamonds absorb ultraviolet radiation at wavelengths shorter that 300 nm but some did not. It was observed that the anomalously transparent diamonds seemed to be made up of a large number of thin parallel plates. In this way, diamonds were classified into two distinct classes - 'Type 1' (opaque) and 'Type 2' (transparent). It was deduced that Type 2 diamonds were more nearly ideal crystals and the absorption observed in the Type 1 diamonds was due to strains present in the less ideal crystal lattice. However, it is now known that the difference in absorption is due to nitrogen impurities in the crystal and that some diamonds are transparent at 300 nm and opaque at 8 μm (these contain nitrogen in the 'B' aggregate and will be discussed in later sections). Thus, it was to explain why some diamonds absorbed certain wavelengths of radiation and some didn't that Raman proposed his theory that diamonds can exist with different crystallographic structures.

Raman discovered that if he focused a beam of monochromatic light onto a light scattering material (e.g. glycerine or diamond) some of the energy from the light could be absorbed by the substance in the form of molecular vibrations resulting in an increase in wavelength (decrease in energy) of the light - known as the *Raman effect* [7].

Raman collected diamonds from India and South Africa and subjected them to a series of detailed measurements on the way they absorbed light, emitted it in fluorescence and scattered it through the Raman effect. The results of these

experiments explained the differences observed by Robertson, Fox and Martin. Raman concluded that the electronic configuration of the atoms in diamond possessed tetrahedral symmetry, which allowed four possible arrangements of the atoms, two with tetrahedral structure and two with octahedral structure.

The results from Raman's studies indicated that the Type 1 diamonds could absorb infrared radiation and show Raman scattering. In contrast the Type 2 diamonds could produce only Raman scattering and not infrared absorption. From the fact that vibration of a tetrahedral crystal is theoretically allowed to produce both infrared absorption and Raman light scattering and that an octahedral lattice cannot, it was concluded that Type 1 diamonds are tetrahedral and the rarer Type 2 diamonds are octahedral. Additionally, from his scattering experiments Raman had shown that there was no detectable difference in the vibrational frequencies of the diamond lattice, whether it was Type 1 or Type 2. This indicated the bonds between the carbon atoms were similar in both types of diamond.

These conclusions, although backed up by much experimental evidence was quickly challenged and dismissed by Kathleen Lonsdale [8], who exploited the fact that a specific x-ray deflection, known as the 222 reflection, could occur weakly in octahedral crystals but was forbidden from tetrahedral lattices. She showed there was a definite 222 reflection from Type 1 diamond, proving Raman's theories incorrect and suggesting that the natural growth shape is octahedral for all diamonds. It has now been shown that each diamond tetrahedron combines with four other tetrahedra forming a strongly bonded, three-dimensional covalent

crystalline structure. This structure can exist in two forms, one with cubic symmetry (the more common and stable) and one with hexagonal symmetry that is known as the mineral Lonsdaleite.

The cubic structure described above that is diamond is characterised by strong (711 kJ mol^{-1}) covalent bonds with short (0.154 nm) bond lengths. The diamond unit cell consists of eight atoms located at ⅛ x 8 at the corners, ½ x 6 at the faces and 4 inside the unit cell, Figure 2.3.1(a) and (b). On a macroscopic scale the diamond structure can be considered as a stacking of infinite layers of the {111} planes displaying a stacking sequence ABCABC so that every third layer is identical.

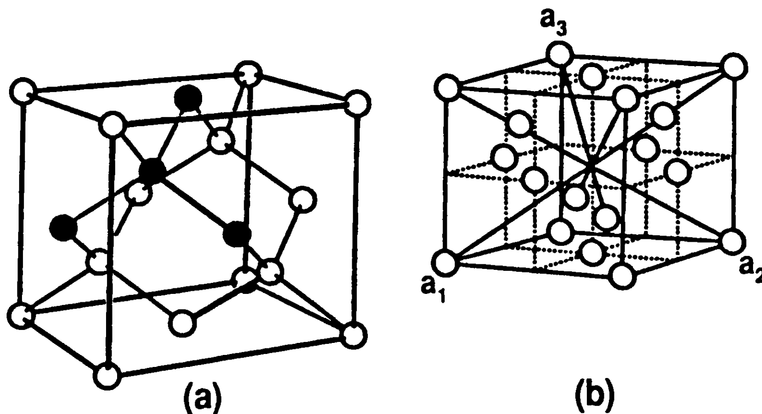

Figure 2.3.1: (a) & (b) Schematic Representation of the Diamond Unit Cell.

How is the atomic structure in diamond different to that of graphite?

Figure 2.3.2(a) below shows the atomic arrangement of graphite. The atoms are joined in a two dimensional hexagonal arrangement. The separation of neighbouring atoms (0.142 nm) is less than that in diamond (0.154 nm) resulting in very strong bonding in the cleavage plane. The planes are 0.34 nm apart which is too large to result in strong bonding between atoms, but enough interaction is achieved to

produce an ordered structure. This combination of weak inter-plane bonding and strong intra-plane bonding allows the planes to readily slip over each other while remaining intact. This property is commonly exploited in the use of graphite as a lubricant.

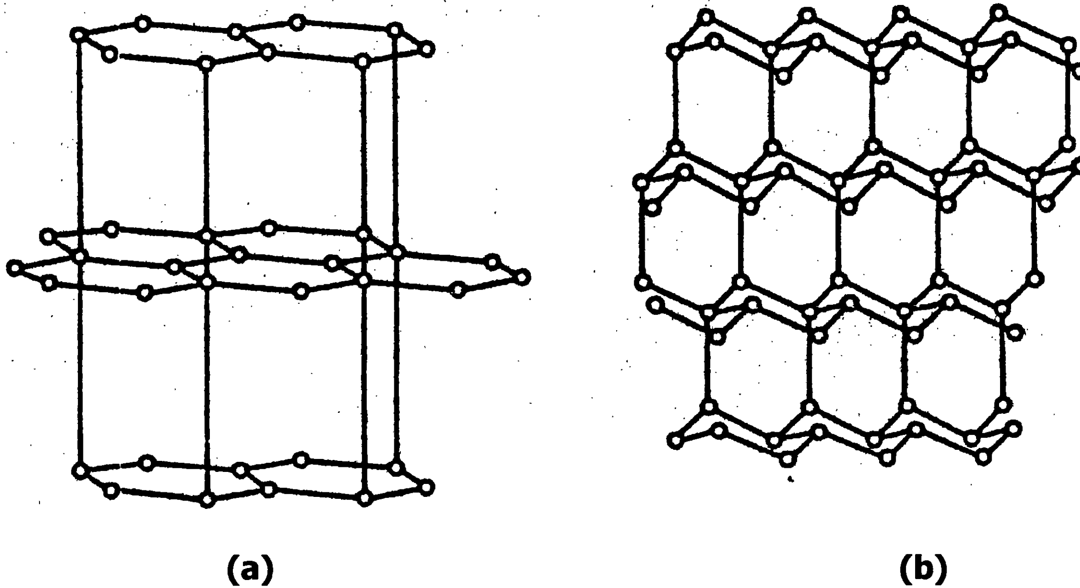

Figure 2.3.2: Atomic Arrangement of (a) Graphite and (b) Diamond.

Diamond and graphite are geometrically similar. In diamond there is also a hexagonal ring structure, however it is 'puckered' so that one atom is above the plane of the ring and one is below in the 'chair' formation, as shown in Figure 2.3.2(b). Diamond is readily converted to graphite if enough energy is supplied. The hexagonal rings become separated to 0.34nm found in graphite and this weakening of one bond from each atom causes the atoms to rearrange within the hexagonal ring, reducing the inter-atomic spacing to that of graphite. This conversion of diamond to graphite is thermodynamically favourable; the challenge to scientists was the reverse process of converting graphite to diamond and will be discussed in later sections.

2.4 Physical Properties of Diamond

Diamond is an extraordinary material and displays the following properties.

- The highest thermal conductivity of any solid at room temperature, five times that of copper.
- Optically transparent from the far infrared to the ultra-violet, making it ideal for optical window applications.
- Outstanding semiconductor properties, very high electrical breakdown strength compared to other semiconductors, high carrier mobilities and a dielectric constant that is half that of silicon.
- Hardest known material.
- Extremely resistant to neutron radiation.
- Superb strength and rigidity.
- Unusually high refractive index.
- Excellent lubricity in air, similar to that of Teflon™.
- Highest atom-number density of any material.

What effect do impurities have? As mentioned above, even a tiny amount of impurity can have a drastic effect on the properties of diamond and both synthetic and natural diamond are never completely free of impurities. Two types of impurity are commonly found in diamond.

- Lattice impurities - consisting of foreign elements incorporated into the lattice in the place of a carbon atom.
- Inclusions - separate particles located in-between the lattice sites, usually consisting of silicates of aluminium, magnesium and calcium.

The two main lattice impurities found in diamond are nitrogen and boron - carbon's neighbours in the periodic table. They both possess small atomic radii and are readily accepted into the diamond structure. Other elemental impurities have been observed but only in extremely small amounts and their effect on the properties of diamond has yet to be fully investigated. Nitrogen is usually found in diamond as pairs of atoms, although it has been observed to exist as isolated atoms and occasionally as platelets.

Diamonds are currently classified based on the nature and amount of impurities present in the structure and consists of four types (Table 2.4.1).

Table 2.4.1: Diamond Classification.

Type	Origin	Impurities
1a	98% of all natural diamonds.	~0.1% N in small aggregates - includes <10% platelets. Not paramagnetic.
1b	Rare in nature (<0.1%). Most HPHT synthetic diamond.	~0.05% N in lattice. Paramagnetic.
2a	Rare in nature.	Few ppm N. Usually clear.
2b	Extremely rare in nature. Produced by high-pressure synthesis.	Less N than 2a. Becomes semiconducting by boron doping. Blue.

Diamond is expensive and only available as small crystals (natural or high-pressure high-temperature (HPHT)) or relatively thin sheets (chemical vapour deposition (CVD)). As a result, it is often expensive and difficult to accurately measure its physical properties, resulting in a spread in the values reported in the published

literature. The properties listed below are an attempt to provide an overview of the currently accepted values for single crystal diamond, either natural or synthetic.

Thermal Properties. The carbon phase diagram below (Figure 2.4.1) displays the thermodynamic relationship between diamond and graphite and shows that diamond is not stable at room temperature and pressure. However, the diamond to graphite transition is infinitesimally small under these conditions and can only be observed as the temperature is increased. For example, at 2100 °C a 0.1 carat (0.02 g) octahedral crystal is converted to graphite in less than three minutes [9].

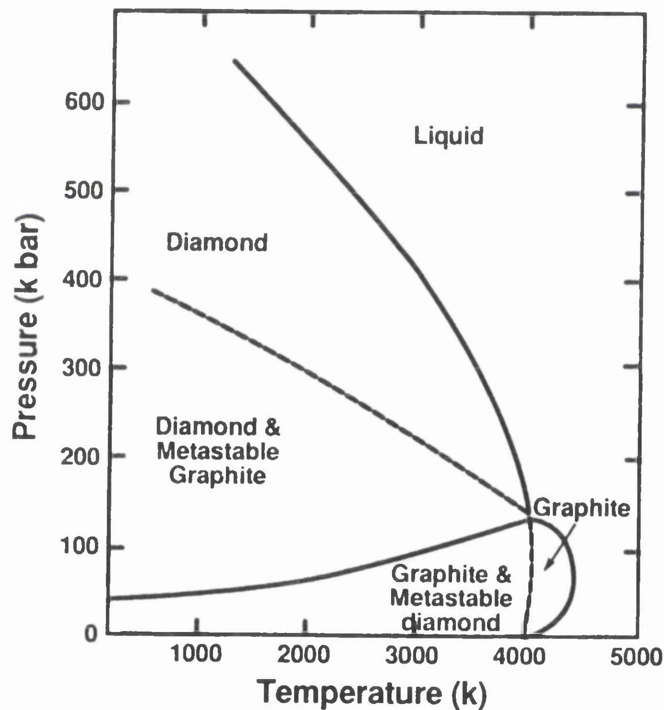

Figure 2.4.1: Carbon Phase Diagram.

'Impurity free' diamond has the highest thermal conductivity of any known solid material at room temperature. Thermal conductivity occurs in diamond in the form of lattice vibrations as opposed to electron transport in metals. Lattice vibrations occur in diamond if the carbon atoms are excited by a source of energy, in this case heat.

The carbon atoms are small, have low mass and are tightly and isotropically bonded. This means the quantum energies required to vibrate the atoms are large and at room temperature few lattice vibrations are present to impede the flow of phonons, resulting in high thermal conductivity. However, impurities, especially nitrogen, can reduce the thermal conductivity.

The coefficient of thermal expansion is low in diamond (0.8 ppm / °C compared to copper 17 ppm / °C) due to the strong bonding between the carbon atoms. Also, the specific heat is higher than for most metals, is comparable to that of graphite and increases with increasing temperature.

Optical Properties. Diamond is unexcelled in its ability to transmit light over a wide range of optical wavelengths. Again, this is a product of the strong inter-atomic bonding. For incident radiation to be absorbed, the energy of the photon must be equal to or greater than the energy required to break a bond and excite an electron across the bandgap. In diamond the bandgap is high (~5.45 eV at room temperature) so for the majority of the optical spectrum the energy of the radiation is less than the band gap and as such is transmitted or refracted by diamond. This is what gives diamond its unequalled brightness in appearance.

Theoretically, pure diamond has only two intrinsic absorption bands.

- Ultra-violet absorption due to an electron transition across the band gap at 230 nm, Figure 2.4.4.

- Infra-red absorption between 1400 - 2350 wave numbers (cm^{-1}) due to the creation of phonons and the intrinsic multi-phonon absorption, Figure 2.4.5.

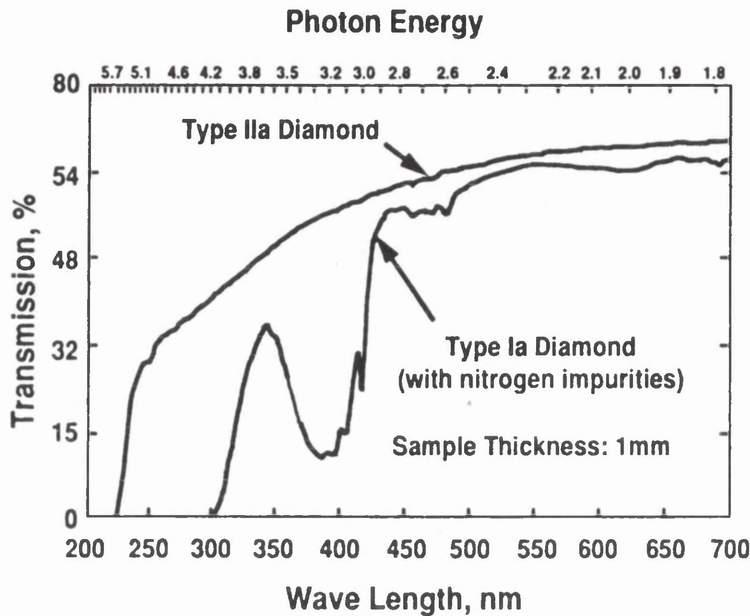

Figure 2.4.4: Transmission Spectra of Natural Type 1a and 2a Diamond.

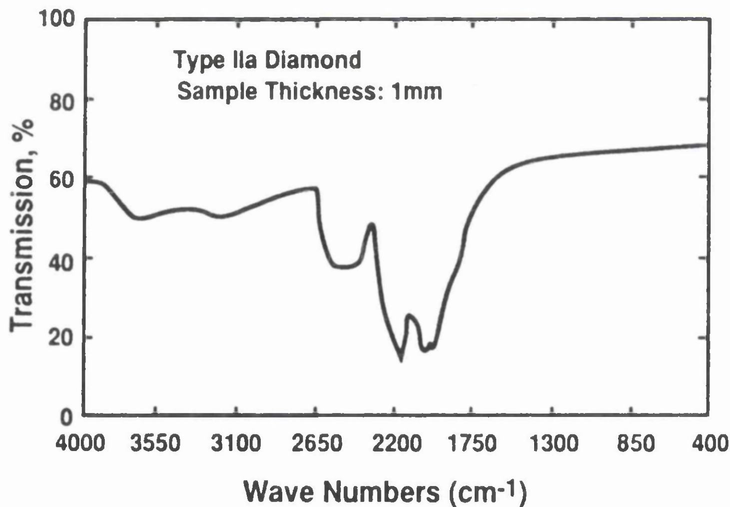

Figure 2.4.5: Infra-red Transmission by Type 2a Diamond.

As a result, diamond is the ideal transparent material. However, impurities, especially nitrogen, and lattice defects can impede the movement of photons, reducing the transmittance and increasing the absorption bands. Nevertheless, diamond is still the best optical material to date.

Photo-luminescence and cathodo-luminesence are also well-documented optical properties of diamond, originating from mid-band gap states caused by impurities and lattice defects. The index of refraction is high for diamond (~2.4) with few materials exhibiting higher indices, e.g. Si (3.5), rutile (2.9), AlC_3 (2.7) and Cu_2O (2.7). X-ray transmission is excellent in diamond due to the low atomic number of carbon.

Acoustic Properties. Sound waves are carried by low-frequency vibrations which are favoured by the structure of diamond, resulting in a high sound velocity: ~20 km/s compared to ~13 km/s for beryllium and ~10 km/s for silicon.

Electrical and Semiconductor Properties. Table 2.4.2 below summarises the electrical and semiconductor properties of diamond.

Table 2.4.2: Electrical and Semiconductor Properties of Diamond.

Property	**Value**
Resistivity	
Type 1 and most 2a	$\sim 10^{16}\ \Omega$ cm
Type 2b	$10^3 - 10^5\ \Omega$ m
Dielectric Constant (at 300 K)	5.7 ± 0.05
Dielectric Strength	10^6 V/cm
Saturated Electron Velocity	2.7×10^7 cm/s
Carrier mobility	
Electron	2200 cm^2/V s
Hole	1600 cm^2/V s

Pure single-crystal diamond has a bandgap of 5.45 eV, and this makes it one of the best solid insulators at room temperature. However, impurities, especially any sp^2 (graphitic) bonding, can render the material useless for electrical applications of this type. The semiconducting properties of diamond are excellent and potentially make it good for many device applications. Diamond is an indirect bandgap material and has the widest bandgap of any semiconducting material.

Basic semiconductor theory states that when a semiconducting material is heated, the probability of electron transfer across the bandgap from the valence band to the conduction band increases as a result of the thermal excitation. Thus, above a threshold temperature the material can no longer operate as a semiconductor. Large bandgap semiconductors can therefore be used at higher temperatures, as there is less probability of electron transfer. Diamond, for example, has an upper operating temperature of 500 °C compared to that of silicon 150 °C and GaAs 250 °C.

Diamond can be doped to produce an extrinsic semiconductor material with the addition of elements such as boron and phosphorus during the synthetic growth process of HPHT or particularly by CVD. Although, n-type phosphorus doping still remains problematic due to the discrepancy in atom size, which not only makes doping difficult, but also introduces significant strain related defects into the lattice.

Diamond exhibits excellent electron carrier mobility, exceeded only by germanium in the p-type and by gallium arsenide in the n-type. The saturated carrier velocity

(velocity at which electrons move in high electric fields) is higher than in other semiconductors and is maintained in high intensity fields, Figure 2.4.6 below.

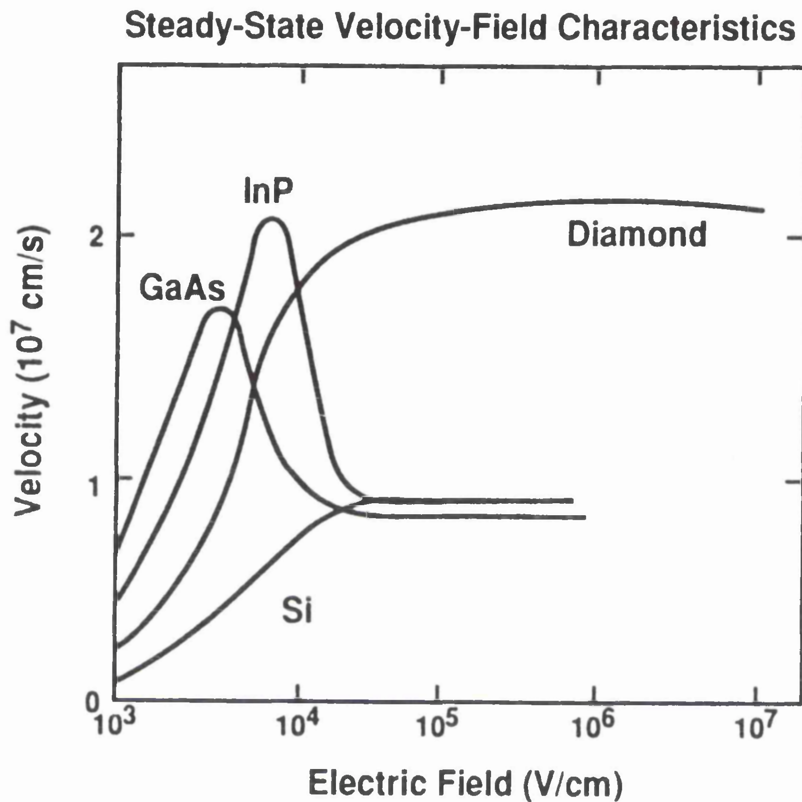

Figure 2.4.6: Electron Carrier Mobility of Diamond and Other Semiconductors.

Mechanical Properties. The mechanical properties of diamond are summarized in Table 2.4.3 below. Included for comparison is data for a high strength ceramic, alumina.

Table 2.4.3: Mechanical Properties of Diamond and Alumina at 23°C.

Property	Diamond	Alumina
Density (g/cm^3)	3.52	3.98
Young's modulus (GPa)	910 - 1250	380 - 400
Compression strength (GPa)	8.68 - 16.53	2.75
Knoop hardness (kg/mm^2)		
Overall	5700 - 10400	2000 - 2100
111 plane	7500 - 10400	
100 plane	6900 - 9600	
Poisson's ratio	0.10 - 0.16	0.22
Coefficient of friction		
In air	0.05 - 0.1	
In vacuum	~1	

Chemical Properties. Diamond is chemically inert in most environments but can be oxidised with relative ease. Oxidation in pure oxygen begins at temperatures as low as 250 °C for finely divided powders and becomes rapid at temperatures above 600 °C.

Diamond is resistant to all liquid organic and inorganic acids at room temperature. However, it can be etched by strong oxidizers such as sodium and potassium nitrates above 500 °C, by fluxes of sodium and potassium chlorate and molten hydroxides such as NaOH. At around 1000 °C it reacts readily with carbide forming materials such as Ni, Co, Fe, Al, Ti and B, and this reaction provides the basis for the high-pressure high-temperature synthesis of diamond discussed below.

2.5 Early Attempts at Diamond Synthesis

One of the first documented attempts to synthesise diamond occurred in 1828 when J N Ganal [10] claimed to have created diamonds several millimetres in diameter by dissolving phosphorus in carbon disulphide and leaving the mixture underwater for three months. However, in H Moissan's detailed study of diamond synthesis, described below, the experiment was repeated [11]. Solid particles were indeed discovered but they dissolved readily in hydrofluoric acid and as such could not have been diamond.

Later in around 1850, C Despretz employed the electric arc furnace in an attempt to produce diamond. By using one platinum and one graphite electrode he found that small micro-crystals resulted at the end of the graphite electrode. These he believed to be diamond, as the crystals reportedly scratched ruby [12]. He gave the electrodes to the Sorbonne. Here they were examined by M Berthelot [13], who found no trace of diamond. It was subsequently suggested by Moissan that the crystals might have been silicon carbide.

E Lionnet was the next to experiment with the use of electricity in the synthesis of diamond. In 1866 [14] he claimed the decomposition of carbon disulphide by the voltage generated between a gold leaf and a tin ribbon resulted in the formation of diamond. Again, this was investigated by Moissan and dismissed.

In 1893 G Rousseau claimed that the decomposition of acetylene at atmospheric pressure via an electrical current would result in diamond formation [15]. Later, in 1907 E de Boismenu electrolysed molten calcium carbide and reported diamond

formation at the anode [16]. However unlikely this may seem, the theory appears to have never been formally disputed.

However, towards the end of the 19th century a more realistic theory of diamond synthesis was suggested. In 1880 Sydney Marsden proposed that if graphite could be dissolved in a solvent it might be possible to crystallise the carbon out in the form of diamond. Marsden used silver and a silver-platinum alloy as the solvent in a graphite crucible containing pure charcoal. This was heated in a gas furnace for 8-9 hours and subsequently cooled slowly over 14 hours. The silver was removed by dissolving in nitric acid and the residue was reported to contain minute crystals. Unfortunately the crystals were too small to allow any chemical analysis but Marsden claimed they were diamonds because there were no other elements present in the reaction system [17]. This approach was repeated in 1905 by C V Burton using a lead-calcium alloy as the solvent [18]. The technique was also investigated by Moissan, as discussed below, and K Krushchev a mineralogist at St Petersburg Medical Academy.

It was also towards the end of the 19th century that diamond mining began from primary deposits in South Africa as opposed to existing sources of diamond such as river deposits resulting from the erosion of a 'diamond pipe'. It became clear that natural diamonds were formed deep within the earth, which from the evidence of volcanic eruptions was known to be at high temperature and pressure. Armed with this new knowledge, the scientist J B Hannay attempted diamond synthesis using the carbon-solvent method. Hannay had already discovered from previous investigations that pressurising a solvent increases the amount of material it can contain, as does

increasing its temperature. Thus, Hannay deduced that diamond synthesis was merely finding out how to contain the reactants for a long enough time at high enough temperature and pressure for the reaction to occur. Hannay acquired hydraulic iron tubing 20 in long, 1" thick and ½" bore. Filled with a trial mixture the tubes were sealed with threaded caps and heated in a gas furnace. The screw threads leaked, so Hannay placed iron balls in the tubes and compressed the ends so that when heated the pressure would cause the balls to push against the necks of the tube and form a seal. This worked until the iron softened and the balls shot out *'like musket balls'* [19]. Next, the tubes were welded up at either end, which was reasonably successful although the tubes still posed a threat at the end of the experiment when they had to be cut open and frequently exploded during this process. Hannay found in some of the tubes that survived some hard black material which when ground in a mortar exposed transparent pieces that appeared to be crystalline carbon exactly the same as diamond. Out of around 80 attempts only three were reported to have been successful and in these the carbon source had been obtained from the decomposition of paraffin spirit by metallic lithium in the presence of *'bone-oil distillate'* which is the nitrogenous distillate obtained in the manufacture of bone char. This is fascinating, as nitrogen is one of the major impurities in diamond and diamonds with the greatest amount of nitrogen impurities have the best overall crystal structure. It is now believed that nitrogen stabilises diamond growth, but at the time Hannay would have had no way of knowing about nitrogen impurities and their effect on diamond growth. However, from the understanding of modern synthesis methods, it is clear that Hannay could not have achieved high enough pressures or temperatures to produce diamond.

Around 1900, Henri Moissan [11] reported a successful and relatively safe way to synthesise diamond. Unfortunately, no examples survive today for analysis. Moissan started by analysing natural diamonds to gain insight into the growth conditions. Burning in oxygen revealed the formation of tiny flakes of graphite at the surface prior to ignition. He investigated how diamond reacted with a wide range of chemicals and analysed the ash from the burning in oxygen experiments and found that iron was a common impurity in most instances. He also obtained two small diamonds from a mainly iron meteorite from Diablo Canyon, Arizona. Initially, he tried to synthesise diamond by dissolving carbon in a solvent and hoping it would crystallise out as diamond. He repeated Marsden's work using silver and eighteen other metals. All proved unsuccessful and he concluded that at ordinary pressures the carbon would be liberated from the solvent only as graphite. To create the high pressure he thought required for diamond synthesis, Moissan dissolved carbon in molten iron and rapidly cooled the solution. This produced the effect of the outside freezing first to produce a solid case, which when the inside began to solidify would create increased pressure. Employing this method, Moissan reported having produced crystals less than a tenth of a millimetre across, that scratched ruby, were approximately the correct density and burned in oxygen to produce CO_2 and no ash. However, he could not obtain enough to confirm chemically that they were diamond and later investigators failed to produce diamonds by this method. Michael Seal in 1963 [20] obtained crystals similar to Moissan's by this method, but using x-ray diffraction showed the crystals to be silicon carbide and alumina.

Other attempts to synthesise diamond were made by Crookes (1905) [21] [22] [23], Parsons (1907) [24] [25] and Hershey (1920's) [26] and although none of the above investigators can be confirmed as being successful, their work provided the basis of the theory of high-pressure high-temperature synthesis in use today.

2.6 High-Pressure High-Temperature (HPHT) Diamond Synthesis

As stated above, diamond is produced in nature at high pressure and temperature. The HPHT synthesis procedure attempts to duplicate this process.

In 1961, P S de Carli and J C Jamieson converted pure graphite directly to diamond by subjecting it to explosive shocks which created pressures ~300,000 atm for ~ 10^{-6} s [27]. In the following year F P Bundy at the General Electric Research Laboratories heated graphite to ~3300 K at 130,000 atm in a customised steel belt press [28]. A short pulse (~ 0.2 ms) of electricity from a capacitor generated the heat (~ 6 J), which was enough to heat the graphite sufficiently, but not enough to damage the press. As displayed in Figure 2.6.1 below, the graphite was in electrical contact with the pistons of the press, which allowed the electrical pulse to be passed through it whilst under pressure. By measuring the voltage and current, an estimate of the temperature could be calculated from the specific heat and mass. Bundy's experiment produced a conglomerate of finely divided crystals, which were confirmed as diamond by X-ray diffraction. Both of the above processes are solid-state reactions where graphite is directly transformed to diamond, i.e. no melting occurs. The graphite to diamond transformation follows the relationship (for T > 1200 K),

$$P^{eq/atm} = 7000 + 27T \qquad \text{Eq. (2.6.1)}$$

with P in atm and T in K, as determined by Bundy [29] from extensive thermodynamic data which include the heat of formation of graphite to diamond, the heat capacity of graphite as a function of temperature and the atomic volume and coefficient of thermal expansion of diamond.

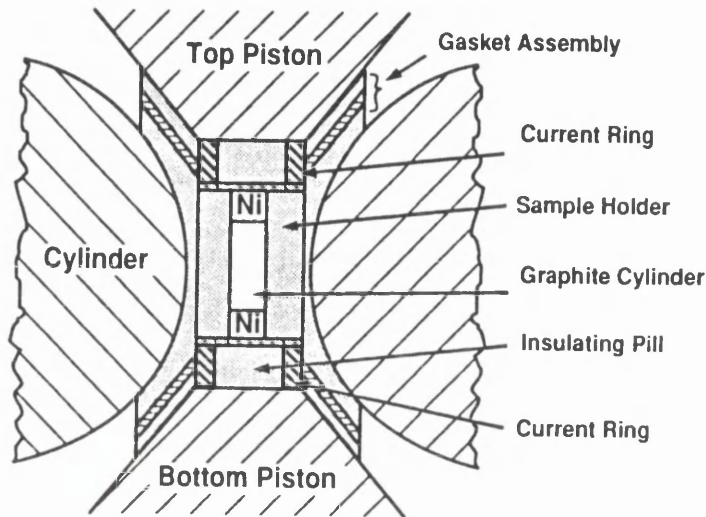

Figure 2.6.1: Belt-press and Pressure Cell Arrangement for Bundy's Diamond Synthesis.

However, there is also a kinetic barrier to diamond synthesis: the rate of transformation is inversely proportional to pressure. This is clearly in contradiction to the thermodynamic conditions necessary for diamond growth and it has been determined experimentally that very high pressures and temperatures are necessary (>130 kbar and 3300 K) for the direct graphite to diamond transformation to proceed at an observable rate, which is expensive and difficult to achieve. Additionally, crystal size is limited using the above procedures, and current commercial processes employ a metal solvent-catalyst.

The use of a metal solvent-catalyst provides a reaction path with lower activation energy, which enables a faster transformation at lower pressure (~55,000 atm) and temperature (~1600 K) than required for the direct transformation. The solvent-catalysts are transition metals such as iron, cobalt, chromium, nickel, platinum and palladium. These metals display a high affinity for carbon, and so are able to break the bonds between carbon atoms and provide a medium for the transfer of the carbon to the diamond growth surface.

Typically, a metal-graphite-metal sandwich configuration will be used for the growth cell. This is placed in the press where the pistons will act as electrical terminals. As the temperature increases the metal will melt, the carbon will dissolve in the metal and at high enough pressure diamond will be stable and will crystallise out of the solvent in this form. In this process, the high temperature is required to melt the metal solvent-catalyst and the high pressure to get into the diamond side of the graphite-diamond equilibrium curve (Figure 2.6.2 below). Excessive temperature and pressure is not needed to drive the reaction at speed, as in the direct conversion performed by Bundy. If conditions are too far into the diamond region of the equilibrium diagram, diamond nucleation will be fast and only small crystals will result. Therefore, production of crystals of a specified size requires careful control of the growth conditions within small limits. This can be difficult as conditions within the cell are constantly changing, e.g. the density of diamond is 50% higher than that of graphite. Thus, the cell volume must decrease to keep the pressure constant.

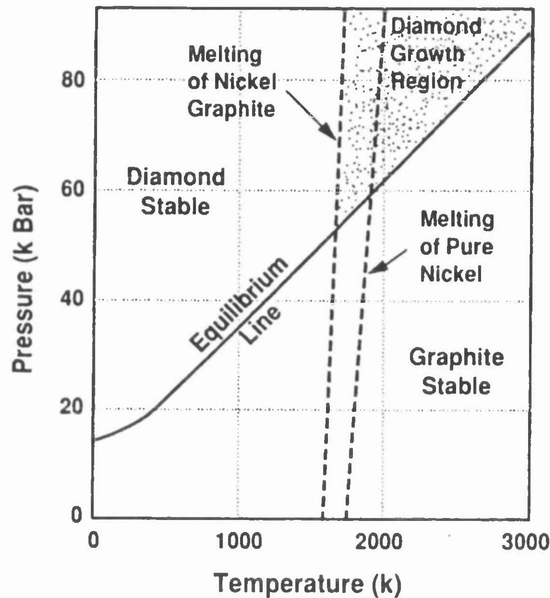

Figure 2.6.2: Graphite-Diamond Equilibrium Curve.

2.7 Chemical Vapour Deposition (CVD) Diamond

The chemical vapour deposition of diamond refers to the low-pressure vapour-phase synthesis, under relatively benign conditions, of polycrystalline diamond sheets. It is predicted that this form of synthesis will lead to reduced cost and therefore the full exploitation of diamond as an engineering material. Current applications include optical windows, thermal management and wear/chemical resistant coatings. Additionally, it has been suggested that diamond is a material suitable for the production of high power electronic devices [30], particle detectors [31], field effect transistors [32] and UV photo-detectors [33]. As stated above, CVD diamond has a polycrystalline structure, as opposed to most natural and HPHT diamond which is single-crystal in structure. Sheets of CVD diamond are routinely produced to thicknesses of 1 mm and greater.

Deposition. The basic reaction in the formation of CVD diamond involves the decomposition of a hydrocarbon such as methane.

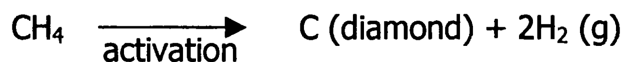

$$CH_4 \xrightarrow{\text{activation}} C\ (\text{diamond}) + 2H_2\ (g)$$

However, in reality the mechanism is far more complex, involving the interaction of many species and factors, and to date is not fully understood. Nevertheless, two conditions for growth have been identified and are generally accepted.

1. Activation of the carbon species.
2. Action of atomic hydrogen.

The hydrocarbon used as the carbon source decomposes into two stable primary species, a methyl radical (CH_3) and acetylene (C_2H_2). The methyl radical is considered to be the dominant species and is the key to diamond growth in the most common forms of CVD diamond synthesis (hot filament and microwave plasma CVD) [34] [35]. The deposition mechanism has been proposed as a two-step process [36].

1. The diamond surface is activated by the removal of surface bonded hydrogen by atomic hydrogen.

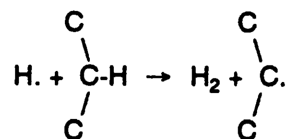

2. The activated surface carbon radical reacts with the carbon-hydrogen species in the gas phase, becoming the site for carbon addition.

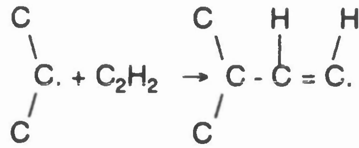

Atomic hydrogen has an essential role in the surface and plasma chemistry of diamond deposition. It is responsible for the stabilization of the sp^3 dangling bonds on the diamond surface plane (Figure 2.7.1). Without this, the bonds would not be maintained and would collapse into the graphite structure.

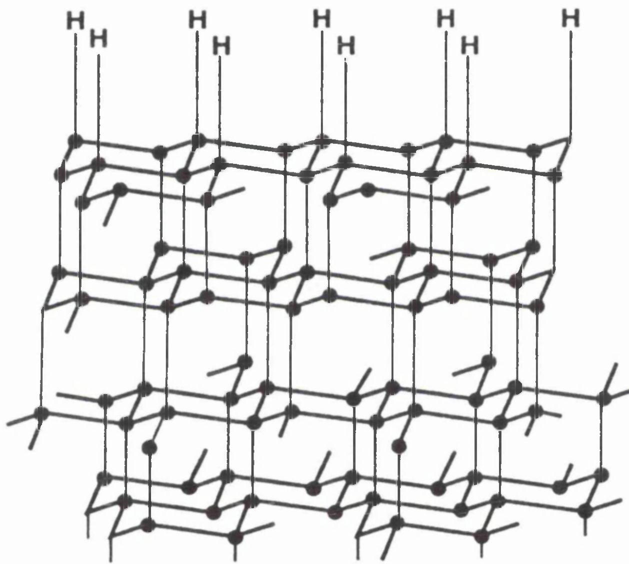

Figure 2.7.1: Stabilization of sp^3 Dangling Bonds by Hydrogen.

Additionally, atomic hydrogen is extremely reactive and selectively etches graphitic deposits twenty times faster than diamond (and even faster in the presence of oxygen). As diamond and graphite are always deposited simultaneously, this effect is crucial for preferentially removing the graphite and leaving most of the diamond intact. Currently, both graphite removal and sp^3 bond stabilization are believed to be essential for CVD diamond growth [37].

It has also been demonstrated that the addition of oxygen or oxygen-containing compounds (e.g. H_2O, CO, methanol, ethanol and acetone) can substantially enhance CVD diamond growth. O_2 added to methane and hydrogen results in the suppression of graphite formation (by reduction of the acetylene concentration) and increased diamond growth rate [38]. The addition of H_2O to H_2 increases the formation of atomic hydrogen, resulting in an increase in the deposition rate of CVD diamond.

Processes. As mentioned above, for diamond deposition to take place the carbon must be activated, otherwise as graphite is the stable form of carbon at the pressures used for CVD only this would be produced. Activation can be achieved by two methods, high temperature and plasma, both of which require large amounts of energy. There are four main CVD processes currently using the above methods for the production of diamond films, high-frequency (glow) plasma, plasma-arc, thermal CVD and combustion synthesis.

Most CVD processes require the formation of a plasma. By increasing the temperature of a gas some of the atoms are ionised (lose electrons), resulting in the formation of a plasma of positively charged ions, electrons (negative charge) and atoms that have not been ionised. There are two types of plasma used in CVD diamond synthesis, glow-discharge (non-isothermal) and arc-plasma (isothermal).

A glow-discharge plasma is generated in a gas by high-frequency electric fields (e.g. microwave frequency 2.45 GHz, radio frequency 13.45 MHz) at relatively low

pressure. The electric field ionises the gases, resulting in the formation of electrons (small mass) and ions (large mass in comparison to electrons). The electrons, due to their small mass, are quickly accelerated to high energies (~5000 K). In contrast, the heavier ions cannot react so quickly to the changing field direction, therefore their temperatures and that of the plasma stay low - hence, non-isothermal. The high-energy electrons collide with the gas molecules resulting in dissociation, the formation of reactive chemical species and the initiation of chemical reactions.

Typically, microwave plasmas are used for CVD diamond deposition. These have electron densities of the order of 10^{20} electrons/m^3 and sufficient energy to dissociate hydrogen. Figure 2.7.2 displays schematically a microwave plasma CVD (MPCVD) reactor and Table 2.7.1 displays the typical deposition parameters for such a system.

Table 2.7.1: Typical MPCVD Deposition Conditions.

Parameter	**Value**
Incident Power	600 W
Substrate Temperature	800 - 1000 °C
Gas Mixture H2/CH4	50/1 - 200/1
Pressure	10 - 5000 Pa
Total Gas Flow	20 - 200 scm^3/min

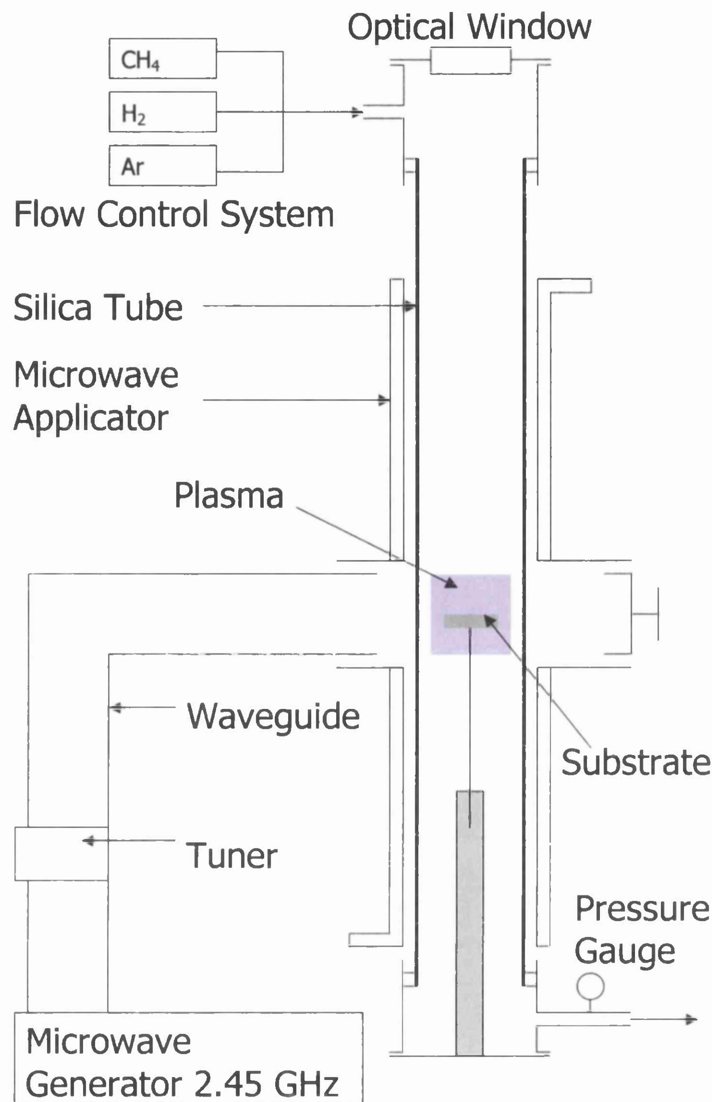

Figure 2.7.2: Schematic of a MPCVD Reactor.

The substrate (typically silicon) is positioned at the lower end of the plasma. Gases are fed in at the top of the reactor, flow around the chamber and react at the substrate surface. Gaseous by-products are removed via the exhaust system. Substrate temperatures in the region 800 - 1000 °C are required for diamond growth and can be achieved through interaction with the plasma and microwave power but are difficult to control accurately. As a result, radiant or resistance heaters are more commonly employed for this purpose.

The morphology and properties of the deposited CVD diamond coating vary as a function of substrate temperature, gas ratio and intensity of plasma. The deposition rate is relatively slow (~ 1 - 3 μm/hr) due to the low concentration of atomic hydrogen at the substrate surface (~ 5%). The microwave plasma is very stable and is easily maintained over several days. However, it can be easily disturbed by the introduction of oxygenated compounds.

Microwave plasma CVD can also be achieved using electron cyclotron resonance (ECR) and a combination of electric and magnetic fields. The electron cyclotron resonance occurs when the frequency of the alternating electric field matches the natural frequency of the electrons orbiting the lines of force of the magnetic field. This occurs at a microwave frequency of 2.45 GHz with magnetic fields of 875 Gauss. This type of system minimises substrate damage due to the high-intensity ion bombardment common in other forms of high-frequency deposition system, and operates at a relatively low temperature enabling the use of heat sensitive substrates. However, the system is more difficult to control than conventional forms of MPCVD and also requires more expensive equipment.

Radio-frequency (RF) plasma CVD systems have been used to produce diamond, but tend to produce the related and technologically important material diamond-like carbon (DLC) rather than pure diamond. DLC is a meta-stable carbonaceous amorphous material commonly produced via RF/DC PECVD, but films can also be grown by sputtering and ion beam deposition, from a variety of carbon bearing solid and gaseous source materials. Substrate temperatures are significantly lower (T <

325 °C) than those required for the production of diamond. The term diamond-like is used because the material is characterised by extreme hardness and significant optical gap. Although DLC is categorised as an amorphous material (i.e. no long-range order) containing sp^3, sp^2 and sp^1 hybridised carbon, some microcrystallinity sometimes occurs from medium-range ordering.

Other forms of deposition systems for producing CVD diamond include plasma-arc (DC plasma systems), thermal CVD (hot-filament) and combustion synthesis (oxy-acetylene torch) but are less commonly employed and are outside the scope of the present study.

Nucleation and Growth. CVD diamond is normally a polycrystalline material displaying grain sizes from a few nm to tens of µm. Its polycrystalline nature is due to the formation of multiple nuclei on the substrate surface. These, coalesce to form a continuous and polycrystalline film. Whilst some of the nuclei grow, some are crowded out. This often results in an increase in average crystal size with increasing film thickness. Figure 2.7.3 shows a SEM image of a typical CVD diamond film.

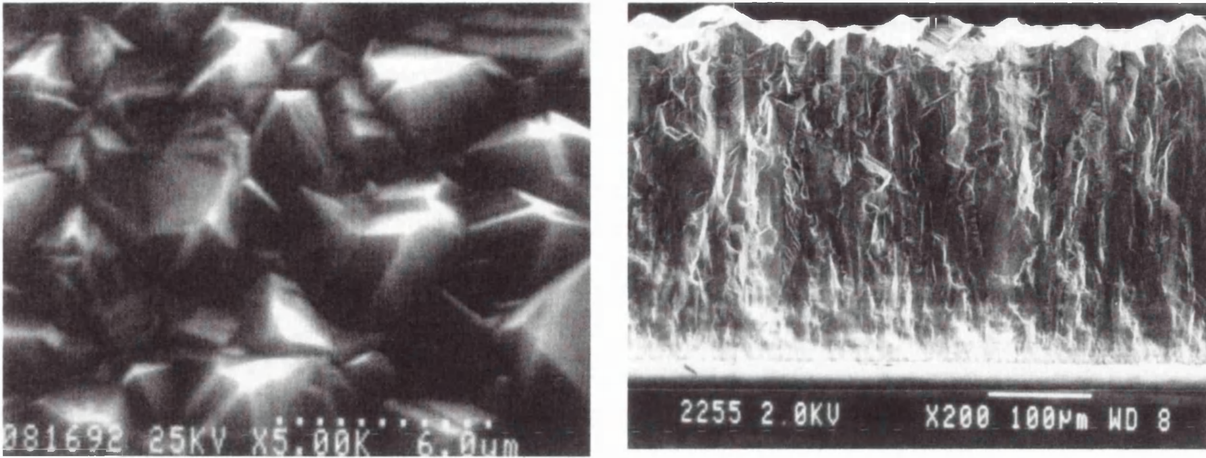

(a) **(b)**

Figure 2.7.3: CVD Diamond Film SEM Image: (a) Growth Surface and (b) Cross-section.

The properties of the substrate and its pre-treatment are important in determining the rate of nucleation, but not the subsequent growth rate once nucleation has occurred. Silicon is the most common substrate currently in use, but refractory metals (W, Ta, Mo etc.), carbides and other metals (Cu, Ni, Au) and alloys are also used. The nucleation rate and adhesion are reportedly related to the readiness of the substrate to form intermediate carbides, and surface pre-treatments (etching and scratching with diamond powder/polish) have been reported to improve both nucleation and adhesion.

As discussed above, the properties of diamond are governed by impurities and lattice defects. However, they are also affected by crystal boundaries (particularly high-angle boundaries). These are common in polycrystalline materials such as CVD diamond, which display various crystallite orientations and grain sizes.

The capability to deposit single-crystal diamond (or even a material with a high level of crystallinity) would be significant in the development of CVD diamond for electronic, semiconductor, optical and other applications. It has been suggested that epitaxial growth of single crystal diamond by CVD could be achieved by using a substrate with crystal lattice parameters close to those of diamond and displaying similar bonding characteristics. To date, single-crystal diamond is the only suitable material found for this application, and is obviously limited by its small size and high cost. If other materials could be developed for epitaxial CVD diamond growth, this would allow production of semiconducting wafers. There have been indications that nickel and some of its alloys display the necessary properties for epitaxial growth of diamond films. In particular, the lattice constants of diamond (3.52 Å) and nickel (3.56 Å) are well matched.

The as-grown films currently produced display a relatively rough surface topography, as shown in Figure 2.7.3 above. Thus, a polishing step is required for applications that require a smooth surface (e.g. optical windows). Traditionally, polishing to a radius of less than 5 nm without chipping or pulling was difficult, but ion-beam techniques have been developed which soften the surface [39]. The surface can then be mechanically polished with diamond paste.

Properties. CVD diamond is a relatively new material and as such is still expensive. This, combined with the fact that it is only available in small quantities (as coatings or thin sheets), makes accurate measurement of its properties difficult. Also, the effects of impurities, defects and the differences in production processes result in the

large spread in values reported in the literature. Table 2.7.2 attempts to summarize the properties of CVD diamond and compares them to those of single-crystal diamond.

Table 2.7.2: Properties of CVD Diamond*.

Property	CVD Diamond	Single-Crystal Diamond
Density (g/cm^3)	3.51	3.515
Thermal conductivity at 25 °C (W/m K)	2100	2200
Th. exp. coef. x 10^{-6}/°C at 25 - 200 °C	2.0	1.5 - 4.8
Bandgap (eV)	5.45	5.45
Index of refraction at 10 μm	2.34 - 2.42	2.4
Electrical resistivity (Ω cm)	10^{12} - 10^{16}	10^{16}
Dielectric constant (45 MHz - 20 GHz)	5.6	5.7
Dielectric strength (V/cm)	10^6	10^6
Saturated electron velocity (x 10^7 cm/s)	2.7	2.7
Carrier mobilities (cm^2/V s)		
Electron	1350 - 1500	2200
Hole	480	1600
Vickers hardness (kg/mm^2)	5000 - 10000	5700 - 10400

* The values of the properties listed above are representative only for a typical CVD diamond material and may vary considerably as a function of deposition parameters.

Applications. Potentially, there are more applications available to CVD diamond than natural/HPHT diamond due to the increased size and (potential) decreased cost offered via the CVD route. Currently, commercial usage is largely limited to optical coatings/windows, wear/chemical resistant coatings and thermal management applications. However, due to its unique properties CVD diamond has recently begun to be exploited for electronic devices such as high-power transistors, high-power field effect transistors, high-power microwave and UV sensors.

References

[1] Lenzen G (1970) *The History Of Diamond Production And The Diamond Trade* transl. F Bradley (London Barrie and Jenkins).

[2] Averani G, Targioni C A (1711) *G. Litterati Ital.* **8** 221.

[3] Lavoisier A-L (1772) *Memoire Academie des Sciences* pp 564, 591.

[4] Tennant S (1797) *Phil. Trans. R. Soc.* **87** 97, 123.

[5] Allen W, Pepys W H (1807) *Phil. Trans. R. Soc.* **97** 267.

[6] Robertson R, Fox J J, Martin A E (1934) *Phil. Trans. R. Soc.* **A232** 463.

[7] Raman C V (1928) *Nature* **121** 501.

[8] Lonsdale K (1945) *Nature* **155** 144.

[9] Spear K E (1989) *J. Am. Ceram. Soc.* **72(2)** 171-191.

[10] Ganal J N (1828) *J. Chim. Méd* **4** 582.

[11] Moissan H (1904) *The Electric Arc Furnace transl. A T de Monilipied* (London: Edward Arnold).

[12] Despretz C many papers in *C. R. Acad. Sci. Paris* from **25** 81 (1847) to **37** (1853).

[13] Berthelot M (1893) *C. R. Acad. Sci. Paris* **116** 226.

[14] Lionnet E (1866) *C. R. Acad. Sci. Paris* **63** 213.

[15] Rousseau G (1893) *C. R. Acad Sci. Paris* **117** 164.

[16] de Boismenu E (1907) *French Patent No. 4566.*

[17] Marsden R S (1880) *Proc. R. Soc. Edinburgh* **11** 20.

[18] Burton C V (1905) *Nature* **72** 397.

[19] Hannay J B (1880) *Proc. R. Soc.* **30** 450.

[20] Seal M (1963) *Proc. Int. Congr. On Diamond in Industry Paris 1962* (London: Industrial Contributors) p313.

[21] Crookes W (1861) *Chem. News* **3** 303.

[22] Crookes W (1887) *Phil. Trans. R. Soc* **A178** 451.

[23] Crookes W (1909) *Diamonds* (London: Harper & Brothers).

[24] Parsons C A (1888) *Proc. R. Soc.* **A76** 512.

[25] Parsons C A (1920) *Phil. Trans. R. Soc.* **220** 67.

[26] Hershey J W (1940) *The Book of Diamonds* (New York: Hearthside).

[27] de Carli P S, Jamieson J C (1961) *Science* **133** 1821.

[28] Bundy F P (1962) *Science* **137** 1057.

[29] Bundy F P, Strong H M, Wentorf R H Jr (1973) *Chemistry and Physics of Carbon Vol. 10* (New York: Marcel Dekker Inc).

[30] Looi H J, Pang Y S, Foord J S, Jackman R B (1998) *Solid-State Electronics* **42**(12) 2215-2223.

[31] Bergonzo P, Foulon F, Marshall R D, Jany C, Brambrilla A, McKeag R D, Jackman R B (1998) *IEEE Transactions on Nuclear Science* **45** 370-373

[32] Looi H J, Pang Y S, Wang Y, Whitfield M D, Jackman R B (1998) *IEEE Electron Device Letters* **19** 112-114.

[33] McKeag R D, Jackman R B (1998) *Diamond and Related Materials* **7** 512-518

[34] Butler J E, Woodin R L (1994) *Thin Film Diamond* (eds. Lettington A, Steeds J W: Chapman & Hall, London) 15-30.

[35] Bachmann P K (1994) *Thin Film Diamond* (eds. Lettington A, Steeds J W: Chapman & Hall, London) 31-53.

[36] Angus J C, Argoitia A, Gat R, Li Z, Sunkara M, Wang L, Wang Y (1994) *Thin Film Diamond* (eds. Lettington A, Steeds J W: Chapman & Hall, London) 1-14.

[37] Spear K E, Frenklash M (1994) *Synthetic Diamond: Emerging CVD Science and Technology* (eds. Spear K E, Dismukes J P: John Wiley & Sons, Inc., New York).

[38] Piekarczyk W (1998) *Diamond and Related Materials* **7** 47-51.

[39] Malshe A P, Park B S, Brown W D, Naseem H A (1999) *Diamond and Related Materials* **8** 1198-1213.

3 ELECTRONIC TRANSPORT IN SEMICONDUCTORS

The sections below introduce the concept of energy-band theory for semi-conductors and how this idea is used to explain the conduction processes in ordered materials. It is then described how this theory is extended to disordered materials and the concept of mobility edges.

3.1 Introduction to Band Theory

Classical conduction theory for a metal assumes that many free electrons are available within the body of the material to take part in the conduction process, and that they behave as classical particles. However, for covalently bonded materials (e.g. semiconductors) the outermost valence electrons are not so loosely bound and are located much nearer to the parent atom's cores, therefore they cannot be considered to be associated with the entire collection of atoms as in a metal. Thus, the free electron model fails for such materials, as the potential experienced by valence electrons can no longer be considered constant throughout the lattice. In practice, it varies rapidly, particularly near to ion cores.

The quantum-mechanical band model described below overcomes this difficulty by assuming that the conduction electrons, as well as being subject to the restriction of the Pauli exclusion principle [1], are not entirely free but move in the perfectly periodic potential of a crystal. In this situation, the energy of electrons can be situated only in allowed bands separated by a forbidden energy gap. Within an allowed band, electrons behave in much the same way as free electrons, and can

interact with externally applied fields to produce conduction effects. However, the interaction parameters must be modified to take account of the presence of the lattice.

It is well understood that the electrons in an isolated atom are only allowed to possess discrete values of energy and the exclusion principle stipulates that each energy level, defined by a set of three quantum numbers, can only be occupied by at most two electrons, provided they have opposite spins.

When atoms are packed closely together in a solid, such that the electronic orbitals of neighbouring atoms tend to overlap, the allowed electron energy levels are modified from those of the individual constituent atoms. Thus, electrons that originally had the same energy in the isolated atoms have their energies slightly modified so that the exclusion principle is not violated.

Consider for example the Si atom. It contains 14 electrons distributed in various atomic energy levels as illustrated in Figure 3.1.1 below.

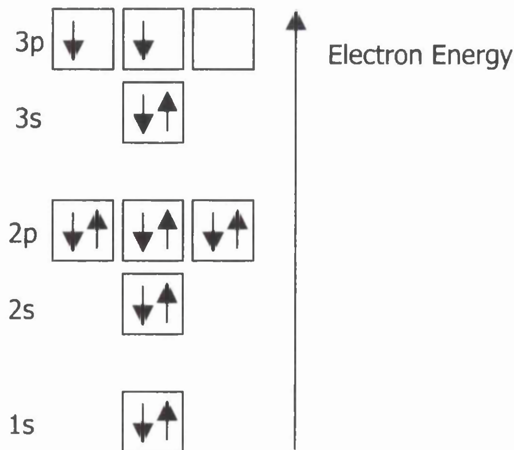

Figure 3.1.1: The Electronic Structure of Silicon.

The inner shells are full and therefore are not able to take part in the bonding process. Additionally, they are also located near to the nucleus and as a result are largely unaffected when Si atoms come together to bond. Consequently, these inner shells can be discounted for the present discussion.

The 3s and 3p sub-shells however, are located further from the nucleus and as the Si atoms approach, the electrons in these sub-shells interact strongly. This leads to the formation of new energy bands.

Since the two 3p orbitals are only half full (and the 3s orbital full) it would be reasonable to expect that a Si atom would bond with two neighbouring Si atoms. However, the 3s and 3p orbitals are located reasonably close, and when four Si atoms approach each other the interaction results in the four orbitals (one s and three p) mixing together to form 4 new hybrid orbitals. They are orientated in tetrahedral directions to maximise the distance between them. This process is known as sp^3 hybridisation and the sp^3 hybrid orbitals each contain one electron and are thus half-full. Therefore, each Si atom can bond with four other Si atoms (or hydrogen atoms etc). The same is true for the carbon atom (important for this study) and it is the sp^3 hybridisation that is responsible for the formation of diamond.

There are two ways in which the sp^3 hybrid orbitals can overlap with those of neighbouring Si atoms to form two molecular orbitals. These are namely 'in phase' (both positive or both negative) and 'out of phase' (one positive and the other one negative) to produce a bonding or an anti-bonding molecular orbit ψ_B or ψ_A

respectively with corresponding energies E_B and E_A. So, each Si – Si bond consists of two paired electrons in a molecular bonding orbital ψ_B.

In the solid there are N (say ~ 5 x 10^{22} cm^{-3}) Si atoms and almost as many ψ_B bonds. Interactions between the ψ_B orbitals (Si – Si bonds) result in splitting of the energy level E_B into N levels. This results in the formation of a completely full (with electrons) energy band known as the valence band.

In a similar way, the interactions between N ψ_A orbitals results in the splitting of the energy level E_A into N levels, thus forming a completely empty (void of electrons) energy band known as the conduction band. The two bands are separated by a definite energy gap E_g (also known as the band-gap). In a perfect crystal there are no states in this region, therefore an electron cannot obtain an energy value within this range.

Electronic states in the allowed bands extend throughout the whole solid, as they are a result of N ψ_B (or ψ_A) orbitals interfering and overlapping one another. As before, N ψ_B orbitals can overlap in N different ways to produce N distinct wavefunctions ψ_{VB} that extend throughout the whole solid. As a result, an individual electron cannot be related to a particular bond or site because the wavefunctions, ψ_{VB}, corresponding to the valence band energies are not concentrated at a single location. Therefore, the electrical properties of semiconductors are based on the fact that there are certain bands of allowed energies for the electrons, and these bands are separated by forbidden energy gaps.

3.2 Conduction in Crystalline Semiconductors

It has been described above how the electrical properties of a solid are characterised by its band structure. In a semiconductor there are two important bands involved in electrical conduction, the valence band and the conduction band separated by a forbidden energy gap, E_g (Figure 3.2.1).

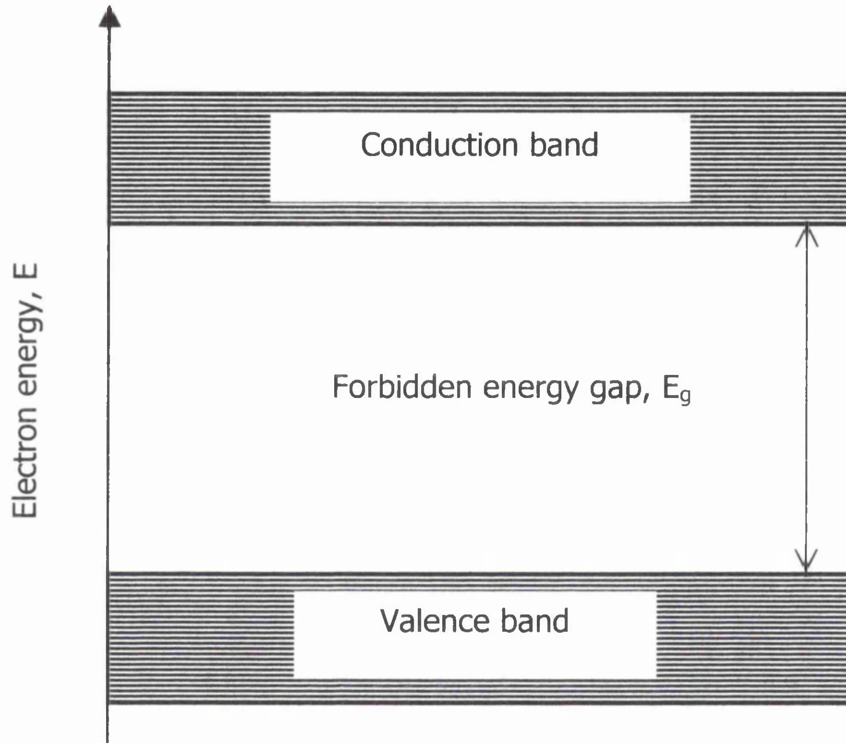

Figure 3.2.1: Band Structure of a Semiconductor.

At 0 K, the valence band is completely full and the conduction band completely empty and the semi-conductor effectively behaves as an insulator. At higher temperatures there is a possibility of electrons being transferred across the energy gap to the conduction band, resulting in vacant levels in the valence band. This concept can also be considered in terms of bonding in the semiconductor lattice. For conduction to occur, sufficient energy ($\geq E_g$) must be supplied to break a bond. This can be achieved by raising the temperature of the crystal until enough energy is

transferred from lattice vibrations to valence electrons to allow them to break free. A freed electron can then move through the crystal, under an applied field, until it experiences another broken bond and recombines or reaches the extinction electrode at the surface of the semiconductor. Also, when a bond is broken and an electron released, a net positive charge is created. This positive charge, or hole, can also move through the crystal and take part in the conduction process.

3.3 Direct and Indirect Band Gap Semiconductors

In some circumstances, particularly when discussing optical absorption, the simplified band model described above becomes inadequate, as it does not contain sufficient information to enable carrier transport effects to be fully explained. Under these conditions it is necessary to consider the energy-momentum (E-p) diagram, which characterises semiconductors into two distinct types, direct (e.g. GaAs) and indirect (e.g. Si, Ge, C) band gap semiconductors (Figure 3.3.1).

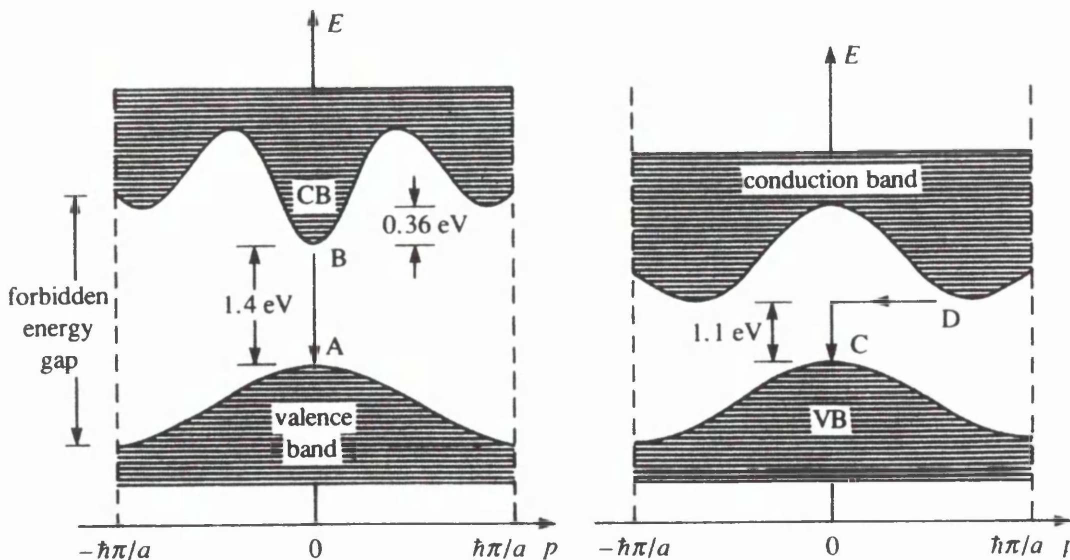

Figure 3.3.1: Examples of Band Diagrams for (a) Direct and (b) Indirect Energy Gap Semiconductors.

In direct band gap semiconductors the maximum in the valence band corresponds to a minimum in the conduction band at p = 0 (A – B in Figure 3.3.1 (a) above). Thus, electrons can be elevated from the valence band to the conduction band with the minimum energy E_g and no momentum change is necessary. However, in indirect band gap materials the valence band maximum occurs at p = 0 but the conduction band minimum is located elsewhere on the momentum axis. Thus, electrons transferred across the energy gap must undergo a momentum change via interaction with lattice phonon vibrations, which is much less likely than the direct process (C – D in Figure 3.3.1 (b) above).

3.4 Recombination and Trapping

Recombination occurs in a semiconductor when an electron is removed from the conduction band to recombine with a hole in the valence band. However, the likelihood of this is very low in the case of indirect band gap materials as momentum must be conserved, which is improbable in the case of a colliding hole and electron. It is more probable that a conduction band electron will return to the valence band only after several intermediate transitions. For example, it may fall into some localised state in the energy gap and after some random time interval be transferred to some empty state in the valence band, i.e. it recombines with a hole from the valence band at the localised level or recombination centre (Figure 3.4.1a). However, it is possible a cascade of phonons may be emitted if no intermediate state is available.

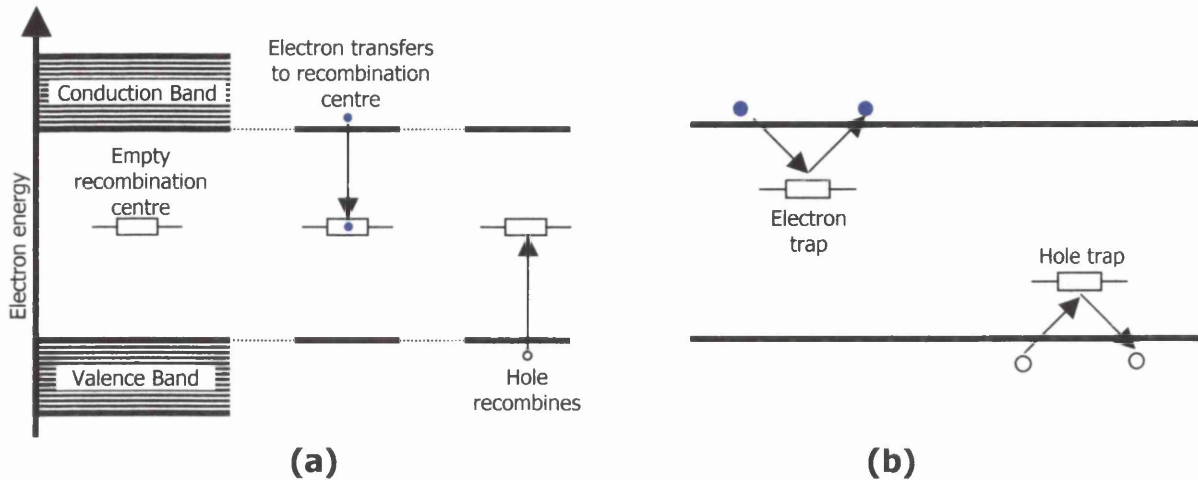

Figure 3.4.1: Illustration of (a) Recombination and (b) Trapping.

Alternatively, the carrier may be trapped at the localised level (Figure 3.4.1b) for a period of time and then released back into its original energy band. With respect to electronic device performance, the impact may be negligible if release is fast, as the electrical signal will not be significantly altered. However, slow traps with release times greater than several seconds are not uncommon and can completely modify electrical information being processed by a device.

Recombination and trapping centres occur at isolated levels in the forbidden energy gap and are the result of some imperfection of the crystal lattice such as dislocations, vacancies and additional atoms.

3.5 Band Structure of Non-Crystalline Semiconductors

It was believed for a long time, during and after the introduction of band theory for crystalline solids, that non-crystalline materials could not behave as semiconductors. This was due to the concept that the bands of allowed electronic energy states

separated by forbidden ranges of energy were due to the interaction of an electronic waveform with a periodic lattice, which fairly reasonably, was thought not possible in materials displaying no long-range order.

However, no real solid is completely amorphous (totally disordered) some short-range order always exists, explaining the fact that non-crystalline semiconductors can possess many of the physical properties of the crystalline form. In many elemental non-crystalline semiconductors, the short-range atomic configuration around a particular site is often fairly well defined and frequently very similar to that of the crystalline material. However, slight variations in bond length and angle may destroy the long-range order (Figure 3.5.1) resulting in the creation of dangling bonds where the bonding requirements of a particular atom cannot be satisfied.

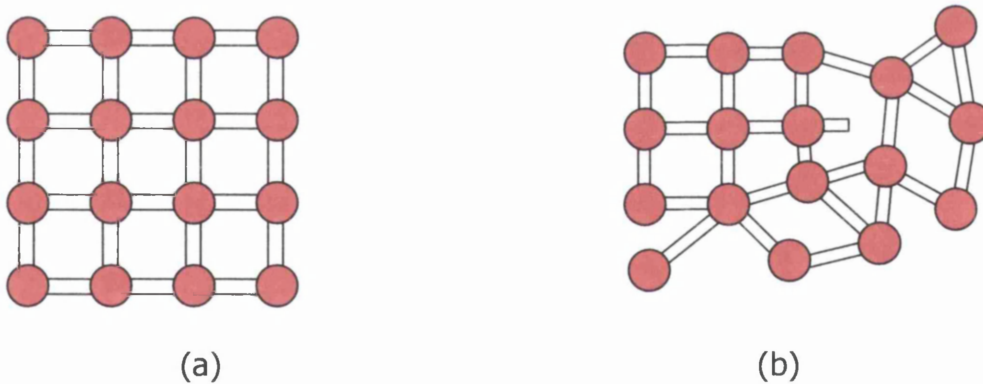

Figure 3.5.1: Illustration of (a) Crystalline Solid and (b) Non-Crystalline Solid.

In highly ordered crystalline materials, defect concentrations tend to be low and each defect site can be considered as being in isolation in an otherwise perfect lattice, resulting in well defined energies for these states. However, the higher defect densities experienced in non-crystalline semiconductors causes random variations in

the environment of individual sites. Thus, the energies of these states will also be subject to random variations. This causes two effects, a blurring of the energy distribution of localised states and variations of local potential which influence the behaviour of free electrons, resulting in localisation of electronic states at the extremities of the energy band.

Figure 3.5.2 below demonstrates that under conditions where high levels of disorder exist, localisation extends well into the energy band, whilst additional localised states become distributed broadly across the energy gap. This theory can be extended, so that for a notionally completely disordered solid extended electronic states completely disappear, as was originally envisaged for all non-crystalline materials.

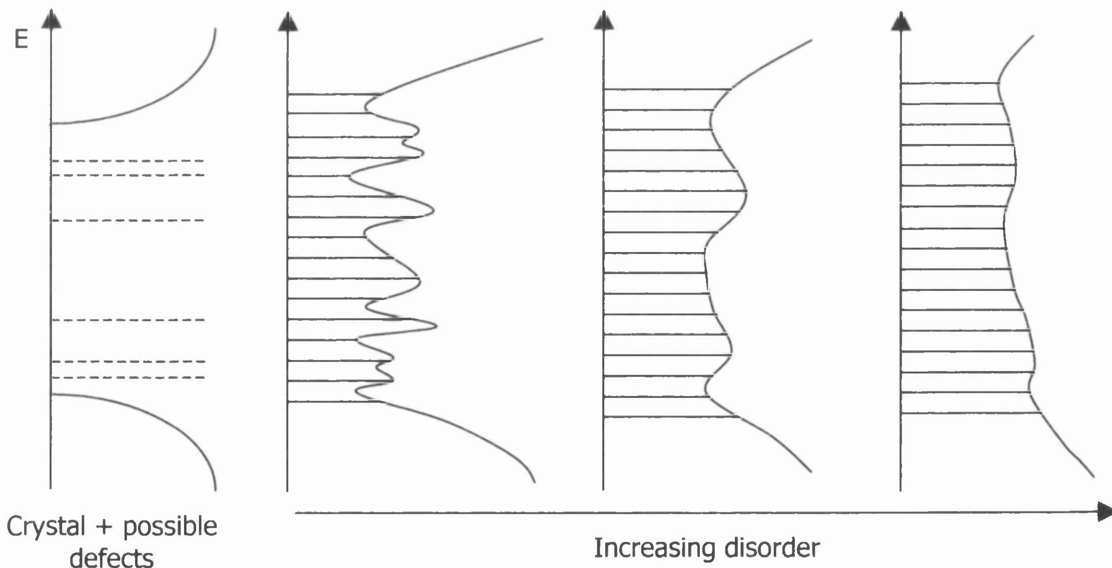

Figure 3.5.2: Effect of Increasing Disorder Upon Band Structure of a Semiconductor.

Several models have been proposed for the systems described above (Figure 3.5.3), Cohen [2] and Mott & Davis [3] suggested idealised models whilst Marshall & Owen [4] developed a different concept arguing that experimental evidence from chalcogenide semiconductors indicated the presence of varying concentrations of localised states at reasonably well defined energies. A similar conclusion was later reached by Spear and co-workers [5] for the technologically important amorphous silicon (a-Si).

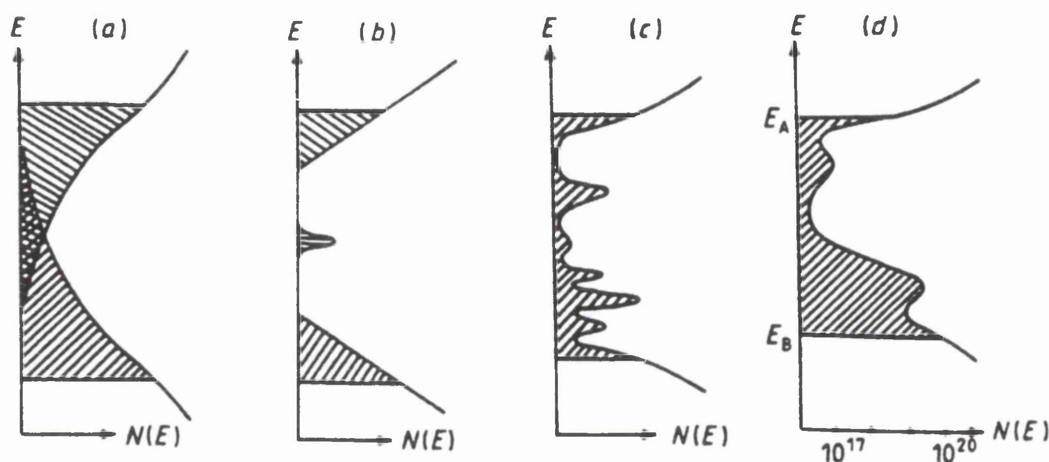

Figure 3.5.3: Models of Non-Crystalline Semiconductor Band Structure: (a) Cohen-Fritzche-Ovshinsky, (b) Mott-Davis, (c) Marshall-Owen and (d) Spear et al.

3.6 Conduction in Non-Crystalline Semiconductors

If a moderate degree of disorder exists, resulting in the type of band structure described by the Marshall-Owen model, there are several different conduction processes by which a charge carrier may move between locations in a non-crystalline semiconductor.

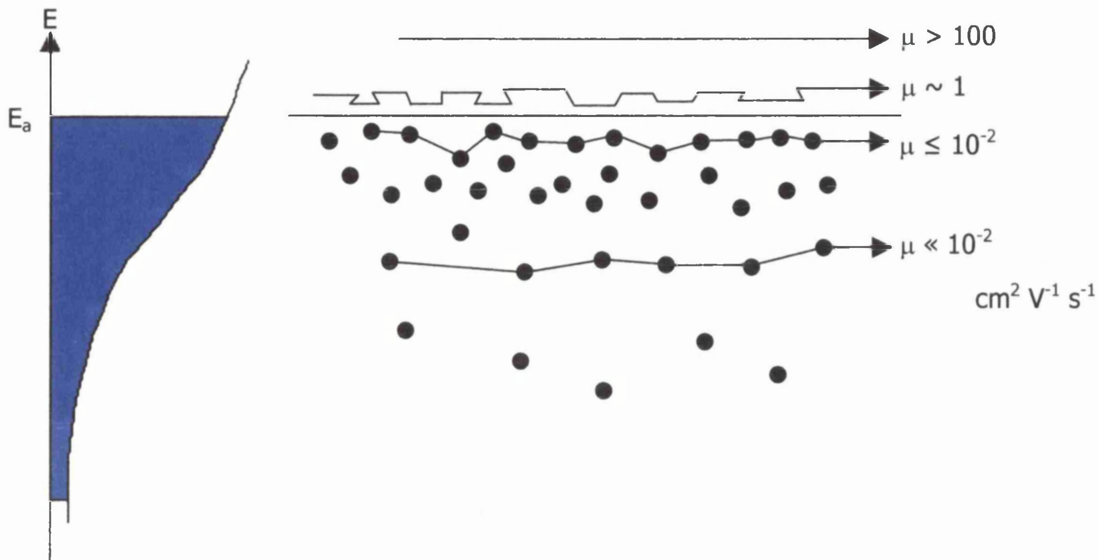

Figure 3.6.1: Variation of Charge Carrier Mobility with Energy.

Considering the information displayed in Figure 3.6.1 above, carriers with energies in excess of E_a (where E_a is the minimum energy for an extended state throughout the material) are free to move within extended electronic states as in the case for crystalline semiconductors. From the conventional band theory, the minimum mobility, μ_0, for electrons in such states has been calculated to be ~ 100 $cm^2V^{-1}s^{-1}$. For mobilities less than this, the calculated mean free path between scattering events becomes less than the De Broglie wavelength of the electron and for mobilities smaller than 10 $cm^2V^{-1}s^{-1}$ the mean free path becomes less than the inter-atomic spacing. However, Cohen [6] calculated a lower limit for extended state conduction (μ_0 ~ 1 $cm^2V^{-1}s^{-1}$) by discarding established band transport theory and considered instead electron motion in the presence of appreciable scattering (similar to the Brownian motion of dust particles in a gas).

It has been argued that, except in the case of high doping levels or sufficiently low temperatures, electronic conduction in crystalline semiconductors involves motion in extended states. However, because of the high density of defect centres present in non-crystalline semiconductors the possibility exists of transport by direct 'tunnelling' between localised states and the magnitude of the mobility for such 'hopping' transport between iso-energetic sites has been estimated to be of the order of [7],

$$\mu_h \approx \left(\frac{e \nu_{ph} \overline{R}^2}{6kT} \right) \exp\left(\frac{-2\overline{R}}{R_0} \right) \exp\left(\frac{-W}{kT} \right) \qquad \text{Eq. (3.6.1)}$$

where, ν_{ph} is the 'attempt to hop' frequency (~ 10^{12} - 10^{13} Hz, i.e. a value appropriate to the top of the phonon frequency), $\overline{R}$ is the mean separation between neighbouring sites, R_0 is the localisation radius of the centres (in practice equal to the effective Bohr radius for localised carriers) and W is any activation energy associated with the tunnelling process. Thus, even in the case of unactivated hopping in the presence of very high densities of localised states μ_h is not expected to exceed ~ 10^{-2} $cm^2V^{-1}s^{-1}$. Considering a more realistic situation where $\frac{\overline{R}}{R_0}$ is well in excess of unity, much smaller values of mobility would be expected. Thus, when considering the case of electronic transport at a specific energy, the carrier mobility is seen to decrease rapidly as the dividing energy between extended and localised states is approached. This dividing energy is commonly termed the 'mobility edge'.

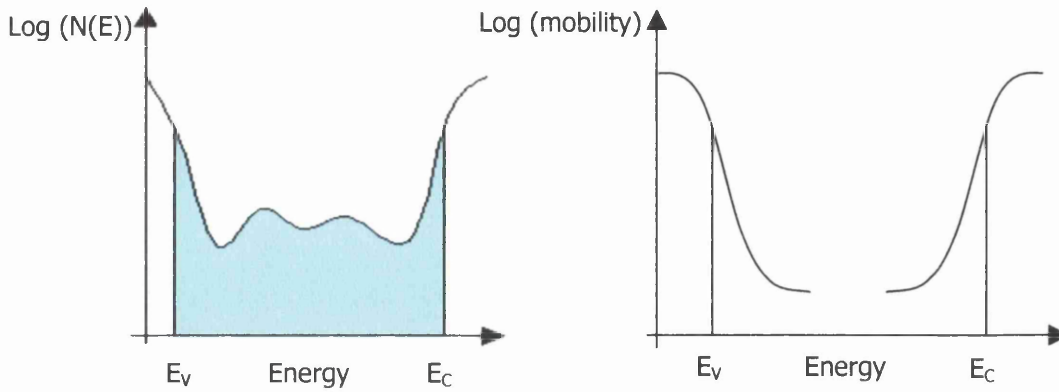

Figure 3.6.2: Energy Bands of a Disordered Semiconductor.

Considering the case illustrated in Figure 3.6.2 above, there exists no forbidden energy gap as allowed electronic states exist at all energies. However, the presence of the mobility edges for the conduction and valence bands causes the electrical conductivity (at appropriately high temperatures) to be dominated by carriers excited into states close to these energies. As a result, the mobility edges become equivalent in most respects to the band edges observed in crystalline semiconductors.

However, in materials possessing significant densities of localised states, it cannot be assumed that carrier transport over macroscopic distances will be iso-energetic. In these circumstances, conduction is more likely to occur via 'trap limited band transport' [8], where carrier transport takes place via extended states but is repeatedly interrupted by trapping in localised states and subsequent re-emission into the extended states after a period of immobilisation. This reduces the macroscopic 'drift mobility', μ_d, from the free carrier value by a factor taking into account the time spent trapped.

$$\mu_d = \mu_0\left(\tau_f\left(\tau_f + \tau_t\right)^{-1}\right) = \mu_0\left(n_f\left(n_f + n_t\right)^{-1}\right) \quad \text{Eq. (3.6.2)}$$

Where, τ_f is the mean free carrier trapping time, τ_t is the mean free carrier release time, n_f is the steady-state density of free carriers and n_t is the steady-state density of trapped carriers (steady state because behaviour under transient conditions can differ appreciably).

Additionally, the hopping transport described above may also be limited in a similar fashion to trap limited band transport, by interaction with deeper lying states. This 'trap limited hopping' [9] [10] is characterised by a mobility derived from Eq. (3.6.2) above by replacing μ_0 with an appropriate hopping mobility from Eq. (3.6.1) related to carrier motion between the shallower localised states and with n_f and n_t being replaced by the concentrations of 'shallow' and 'deep' centres.

It should be noted that interpretation of experimental drift mobility data may be considerably complicated by the possibility that electron-lattice interactions may produce polarons [11] [7] and localised states may interact with each other producing correlation effects [12] [13] leading to charge exchange phenomenon and new types of 'valence alternation' defects.

References

[1] Pauli W (trans. 1980) *General Principles of Quantum Mechanics* (Springer-Verlag, Berlin) 116 – 129.

[2] Cohen M H, Fritzsche H, Ovshinsky S R (1969) *Phys. Rev. Lett.* **22** 1065-1068.

[3] Mott N F, Davis E A (1971) *Electronic Processes in Non-Crystalline Materials* (Oxford: Clarendon) 1st edn.

[4] Marshall J M, Owen A E (1975) *Phil. Mag.* **35** 1341-1356.

[5] Madan A, Le Comber P G, Spear W E (1976) *J. Non-Cryst. Solids* **20** 239-57.

[6] Cohen M H (1970) *J. Non-Cryst. Solids* **4** 391-409.

[7] Mott N F, Davis E A (1979) *Electronic Processes in Non-Crystalline Materials* (Oxford: Clarendon) 2nd edn.

[8] Rose A (1951) *RCA Rev.* **12** 362-414.

[9] Sreet G B, Gill W D (1966) *Phys. Stat. Solidi* **18** 601-607.

[10] Gibbons D J, Spear W E (1966) *J. Phys. Chem. Solids* **27** 1917-1925.

[11] Emin D (1973) *Electronic and Structural Properties of Amorphous Semiconductors* eds. Le Comber P G, Mort J (New York: Academic) 261-328.

[12] Mott N F, Davis E A, Street R A (1975) *Phil. Mag.* **32** 961-991.

[13] Kastner M, Adler D, Fritzsche H (1976) *Phys. Rev. Lett.* **37** 1504-1507.

4 CHARACTERISATION AND ANALYSIS TECHNIQUES

The following section describes how the band structure and electronic transport properties of a material can be explored by the analysis of transient photoconductivity data.

4.1 Transient Photoconductivity in Crystalline Semiconductors

The properties of crystalline semiconductors have been readily extracted via common characterisation techniques such as the 'Hall Effect' [1] and the 'Haynes-Schockley Experiment' [2]. However, the Hall effect produces anomalous results for non-crystalline semiconductors and the Haynes-Schockley technique is not suitable for low mobility materials typical of non-crystalline semiconductors. However, a modified version of the Haynes-Schockley experiment was developed [3] to study crystalline specimens of lower conductivity and mobility that could not be reliably examined by the procedure in its original form (Figure 4.1.1). This revised version of the experiment has also proved valuable in the study of non-crystalline semiconductors.

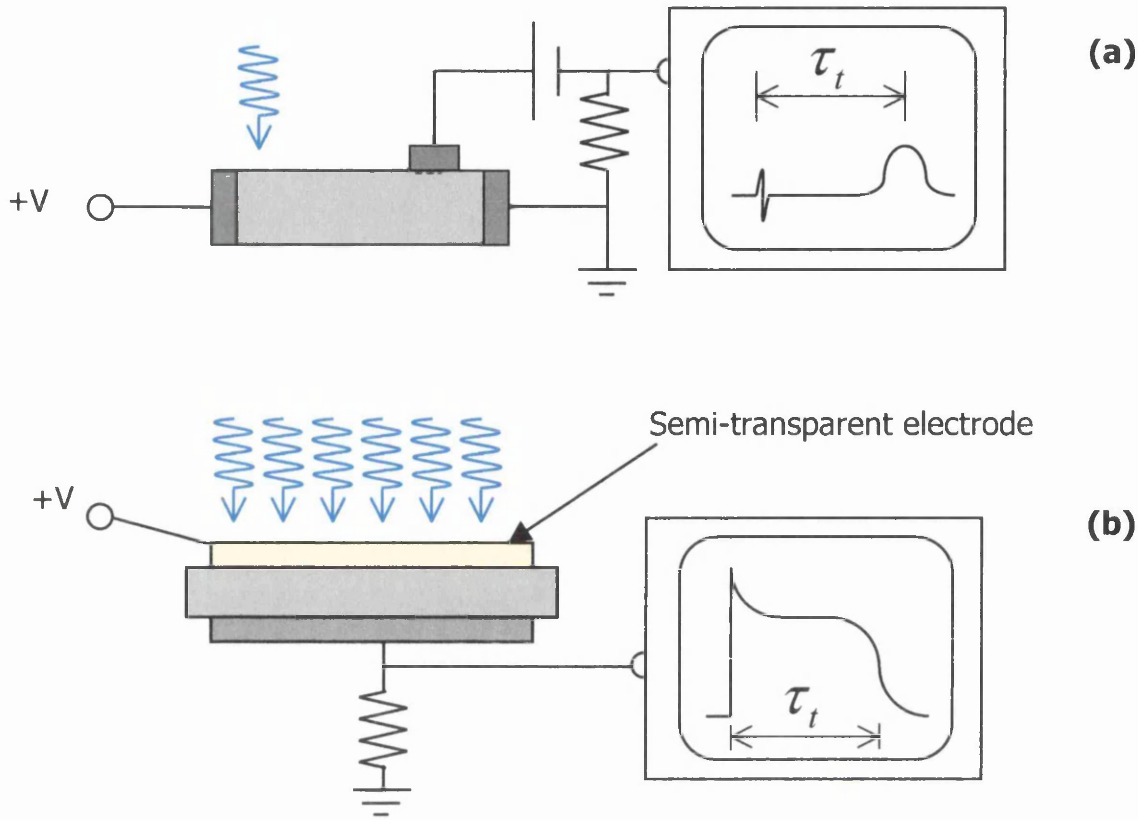

Figure 4.1.1: (a) Haynes-Schockley Experiment and (b) Time-of-Flight (Spear).

In the sandwich configuration illustrated in Figure 4.1.1 (b) above, a short pulse of strongly absorbed photons generates high concentrations of free carriers close to the illuminated surface of the specimen. Then, as long as the material is of sufficiently high resistivity to avoid dielectric relaxation effects over the period of measurement, carriers of one sign (depending on the polarity of the applied field, F) will be drawn across the specimen. Ideally, the electrodes employed will be of a blocking nature, resulting in the excess current generated falling relatively abruptly when carriers reach the lower extinction electrode. In theory, the average transit time, τ_t, can be determined and thus the charge carrier drift mobility, μ_d, can be calculated, taking into account any time spent in shallow traps, via the expression,

$$\mu_d = \frac{l}{F.\tau_t} \quad \text{Eq. (4.1.1)}$$

where, l is the thickness of the specimen. This *'time-of-flight'* (TOF) configuration allows electrons or holes to be studied independently of one another by simply selecting the appropriate polarity of applied field. Additionally, if while using the TOF configuration significant recombination occurs during transit, the proportion of carriers completing their transit will vary depending upon applied field (or inverse transit time). This allows determination of the lifetime (or recombination time), τ_r, of the carrier species under examination via a procedure developed by Hecht [4]. In this procedure, the definite integral of the transient current (a measure of the total charge displacement within the specimen), Q, is plotted versus applied field. Ignoring for the moment disorder induced distortions (discussed below) the relationship should take the form,

$$Q = Q_0.\varepsilon\left(1 - \exp\left(-\varepsilon^{-1}\right)\right) \quad \text{Eq. (4.1.2)}$$

where, $\varepsilon = \frac{\tau_r}{\tau_t} = \frac{F}{F_0}$. At sufficiently high fields, all carriers will complete their transits and thus the integrated current will saturate out, Q_0. At an appropriate lower field, $F = F_0$, Q tends to 0.63Q_0, and the carrier transit time will equal the recombination time (lifetime), τ_r. Hence, if τ_t is measured as a function of F via TOF procedures, τ_r can also be determined.

Nevertheless, care must be taken, as distortion of the pulse shape may occur if the photo-generated charge injected into the specimen is large enough to modify the electric field in the sample. This will result in a space-charge limited transient

behaviour. To avoid this, the injected charge must be restricted to less than the capacitance-voltage product for the specimen.

Mobility and lifetime data can therefore in theory be easily extracted via the TOF procedure. However, the procedure requires (relatively) thick specimens to provide a large enough timescale for analysis. Also, complications may arise due to the interaction of carriers with localised states. However, if the electrodes are not of a blocking nature or the illumination is not strongly absorbed by the specimen (as is the case for the present study) it is inappropriate to interpret the results as TOF data. Nevertheless, important information can still be extracted by interpreting the measurements as transient photocurrent data using the techniques described below.

If it is necessary to use thinner specimens than those required for the sandwich configuration described above, a coplanar electrode configuration could be employed. With selection of an appropriate electrode gap, more meaningful measurements can be obtained using this configuration in relation to some device applications, such as thin film transistors, where the conduction path is parallel to the specimen surface. However, transit time measurements are difficult to perform, requiring a narrow beam of illumination to be focussed close to one of the blocking electrodes. Due to these complications in experimental set-up, it is more usual to perform measurements using injecting electrodes and illumination spanning the inter-electrode gap. This allows study of the interaction of excess carriers with localised states over extended timescales. The obvious drawback of this technique is

that it does not distinguish between the relative contributions of the various species of charge carriers.

4.2 Transient Photoconductivity in Non-Crystalline Semiconductors

Localised states in the mobility gap can affect the time evolution of the transient photocurrent. If a pulse of strongly absorbed illumination is incident on a specimen configured in the TOF arrangement described above, excess charge carriers created will normally populate the extended states outside the mobility edges. Subsequently, they will become trapped in localised defect levels and the time until release back into the extended states will vary with trap depth from the mobility edges, with the shallower states releasing first. However, further trapping and release will occur, resulting in an energy distribution of excess carriers evolving with time. This process is commonly termed 'thermalisation' [5].

If it is assumed that losses due to recombination and extraction at electrodes can be ignored, that defect concentrations are too low for inter-site tunnelling to make a meaningful contribution, and that injected carrier concentrations are low enough to only fill a small proportion of trapping centres, then the time evolution of the photocurrent is dependent upon the nature, energy distribution and other properties of the trapping centres. Hence, it is possible to use the transient photo-response to analyse the defect states using several techniques (discussed below) that have been developed by various groups over the past two decades.

If thermalisation of carriers occurs, using the TOF configuration a progressive reduction of the pre-transit current will occur. Additionally, some carriers during transit may randomly become relatively deeply trapped within the mobility gap. These may then be released at times significantly longer than the average carrier transit time. These effects can combine, significantly distorting the transit pulses (Figure 4.2.1).

In cases with large amounts of this type of dispersion, arrival of the charge carriers at the extinction electrode may be obscured (Figure 4.2.1(b)). Under these circumstances the data can be re-plotted on log-log axes (Figure 4.2.1(d)), highlighting the 'transit time' separating the pre-transit (prior to significant extraction) and post-transit (current governed by release of deeply trapped carriers) regimes. This transit time represents the arrival of the leading edge of the charge packet at the extinction electrode, not an average value for the charge carriers. Also, due to the varying degrees of thermalisation, this value of transit time will be dependent on the applied field. Therefore, a mobility cannot be explicitly calculated. Hence, the drift mobility will decrease with increasing transit time (inverse field) and the drifting charge packet will spread out more than would be expected from conventional diffusion theory. This phenomenon is known as *anomalously dispersive transport* [6] [7]. Thermalisation during transit can also lead to distortion of Hecht plots used for the determination of charge carrier lifetimes.

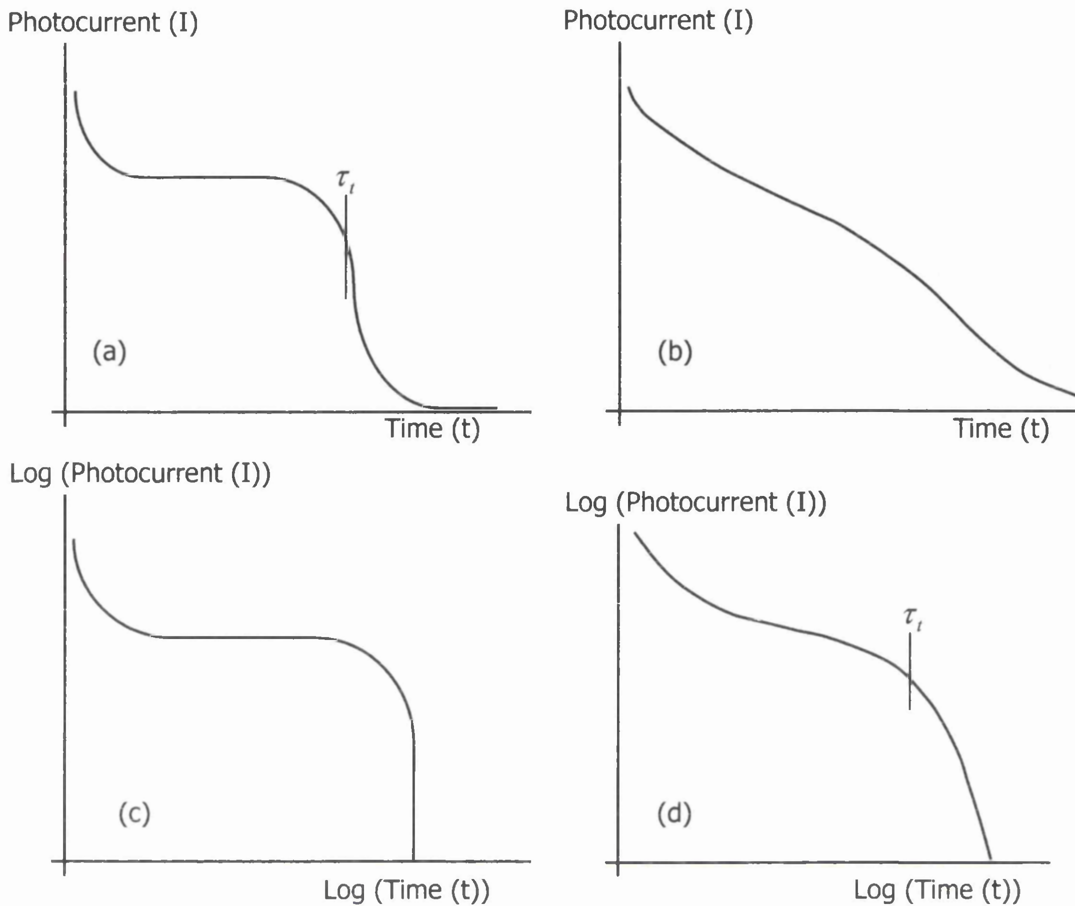

Figure 4.2.1: Typical Transit Pulses and the Effect of Dispersion:

(a) Conventionally Dispersive, (b) Anomalously Dispersive,

(c) & (d) Log-Log Plot of (a) & (b) Respectively.

4.3 Interpretation Techniques

Over the past twenty years or so, many procedures have been developed for the analysis of pulsed transient photoconductivity measurements on disordered semiconductors, with respect to the nature and energy distributions of localised states. In this section the methods most applicable to the data gathered during this study are reviewed.

NOTE: In the following text, all energy values are measured downward from the conduction band mobility edge, E_c, and assumes the carriers under consideration are electrons.

'Thermalisation energy' interpretation of pre-transit currents

The *'pre-transit'* technique [8], as it is commonly known, requires a continuous, relatively broad and featureless (e.g. exponential) energy distribution of the localised states. It is also assumed that no losses occur due to recombination or completion of transit. Then, at time t after generation of N_0 excess charge carriers by illumination of the specimen, the majority of these carriers will reside in states within $k.T$ of a *thermalisation energy*, E_{th}. States at this depth will have a release time constant equal to the time elapsed since generation of the excess charge carriers,

$$E_{th} = k.T.\ln(\nu.t) \qquad \text{Eq. (4.3.1)}$$

where, ν is the *attempt-to-escape frequency* for the localised states, T is the temperature and k is Boltzmann's constant. States shallower than E_{th} have had enough time to reach quasi-thermal equilibrium with each other. Occupancy of these states will therefore decrease rapidly with decreasing depth. In contrast, states deeper than E_{th} will not have had time to reach equilibrium and occupancy will vary with concentration and is assumed (for a suitably decaying localised state distribution) to fall rapidly with increasing depth. This results in a peaking of trapped charge carrier density near to E_{th}. This leads to the relation

$$N(E) \approx \left(\frac{N_{eff}.N_0}{\nu}\right)(n_t.t)^{-1}, \qquad \text{Eq. (4.3.2)}$$

Where, N_{eff} is the effective density of band states, N_0 is the total number of excess photocarriers and n_t is the free number of excess photocarriers.

Since n_t is directly proportional to the transient photocurrent an expression for the concentration of localised states at E_{th} has subsequently been developed [9],

$$N(E_{th}) = \frac{C}{I(t).t}, \qquad \text{Eq. (4.3.3)}$$

where the constant $C = \frac{N_0.N(E_c).e.\mu_0.F}{\nu}$. Here, N_0 is the total number of states in the material, $N(E_c)$ the *effective density* of conduction band states, e the charge on an electron, μ_0 the free electron mobility and F the applied field.

This method provides a relatively simple procedure for determining $N(E_{th})$. However, if sufficient structure exists in the distribution of localised states it has been shown [10] that Equation 4.3.3 can give a complete inversion of the actual $N(E)$. This can also occur if there is significant recombination or trapping into very deep states [11] (with release times in excess of the experimental timescale).

'Thermalisation energy' interpretation of post-transit currents

The *post-transit* regime is said to commence when approximately half of the drifting charge carriers have completed their transit across the specimen to a blocking electrode. Any photocurrent observed after this will be mainly due to emission of carriers from traps deeper than E_{th} at the transit time. It is statistically probable that these carriers will complete their transit without further deeper trapping. The post-

transit current is therefore governed by the rate of emission of charge carriers from the states deeper than E_{th}. The energy distribution is given by [10],

$$N(E_{th}) = C' I(t).t \qquad \text{Eq. (4.3.4)}$$

where, $C' = \frac{2.N(E_c)}{e.N_0.\nu.\tau_{free}}$, and τ_{free} is the free carrier transit time. This procedure results in an inversion of that obtained using the pre-transit technique. However, as stated above, in circumstances where there is significant recombination or very deep trapping it has been shown [11] that it is appropriate to employ the post-transit technique even when carriers do not complete their transit. It is also appropriate to employ the post-transit analysis where the energy distribution of localised states and the corresponding transient photo-response are significantly structured. Under these conditions the elapsed time may involve contributions from traps at different energies or multiple trapping at a particular level.

Fourier transformation of transient photocurrents

In this analysis procedure, developed by Main and co-workers [12], computed localised state distributions have been demonstrated [11] [13] to be insensitive to the effects of carrier losses by recombination or completion of transit.

In this procedure, transient photo-decay data are first transformed from a time to a complex frequency domain set, $I(\omega_n)$, via numerical Fourier integration. A further manipulation of $I(\omega_n)$ yields a discrete representation of $N(E_n)$, where,

$$E_n = kT.\ln\left(\frac{\nu}{\omega_n}\right). \qquad \text{Eq. (4.3.5)}$$

This expression is formally equivalent to Equation (4.3.1) of the pre-transit technique. However, the assumptions concerning the nature of the thermalisation process are unnecessary. The free carrier mobility and concentration of excess carriers are required variables, but will only influence the magnitude of the computed localised state concentrations and not their variation with trap depth.

References

[1] Allison J *Electronic Engineering Semiconductors and Devices* (McGraw-Hill, London, 1990) p137.

[2] Haynes J R, Schockley W (1949) *Physics Review* **75** 1917-1925.

[3] Spear W E (1968) *Journal of Non-Crystalline Solids* **1** 197-214.

[4] Hecht K (1932) *Z. Phys.* **77** 235.

[5] Marshall J M, Main C (1983) *Philosophy Magazine B* **47** 471-480.

[6] Marshall J M (1983) *Reports on Progress in Physics* **46** 1235-1282.

[7] Michiel H, Marshall J M, Adriaenssens G J (1983) *Philosophy Magazine B* **48** 187-202.

[8] Arkhipov V I, Iovu M S, Rudenko A I, Shutov S D (1996) *Phys. Stat. Sol. (a)* **54** 67.

[9] Marshall J M, Barclay R P in *Physics and Chemistry of Disordered Solids* (Eds. Adler D, Fritzche H, Ovshinsky S R, Plenum, New York 1985) p567.

[10] Seynhaeve G F, Barclay R P, Adriaenssens G J, Marshall J M (1989) *Physics Review B* **39** 10139.

[11] Marshall J M in *Thin Film Materials and Devices – Advances in Science and Technology – Proc. 10th International School on Condensed Matter Physics* (Eds. J M Marshall, N Kirov, A Vavarek, J M Maud, World Scientific, Singapore, 1999) p175.

[12] Main C, Webb D P, Reynolds S in *Electronic, Optoelectronic and Magnetic Thin Films – Proc. 8th International School on Condensed Matter Physics* (Eds. J M Marshall, N Kirov, A Vavrek, Research Studies Press, Taunton, 1995).

[13] Marshall J M (2000) *Philosophy Magazine B* **80** 9 1705 – 1726.

5 EXPERIMENTAL PROCEDURES

The following section describes the samples, apparatus and techniques used for the measurement of transient photo-decay data.

5.1 Specimen Preparation

Thin-film polycrystalline diamond samples, grown via microwave plasma chemical vapour deposition, were supplied by De Beers Industrial Diamond Division (UK) Limited. Samples were supplied as 10 mm x 10 mm or 5 mm x 5 mm pieces and varied in thickness (~ 100 – 500 μm), grain size (30 – 60 μm) and surface finish (polished or as-grown). Details of specific specimens can be found in Table 5.1.1 below. Additionally, De Beers supplied samples of single-crystal high-pressure high-temperature synthetic diamond for comparison to the polycrystalline material.

All specimens were equipped with thermally evaporated gold-on-titanium electrodes configured in the 'sandwich' arrangement. It should be noted that because the electrodes used were not of a blocking nature it is appropriate to interpret the measurements as transient photoconductivity data and not as time-of-flight. In addition, it would be impossible to interpret the data as time-of-flight in this instance as the illumination employed was sub-band gap, resulting in carrier generation throughout the bulk of the material and not just at the illuminated surface. Electrical connections were made to these electrodes using silver wire and silver electro-dag. The samples were then mounted into the variable temperature cryostat described below.

Table 5.1.1: Physical Properties of Samples Investigated.

Sample ID	Size (mm)	Thickness (μm)	Surface finish
JMM2	5 x 5	~ 170	Side 1 – as-grown Side 2 – polished
JMM4	5 x 5	~ 500	Both polished
JMM5	10 x 10	~ 100	Side 1 – as-grown Side 2 – polished
JMM6	10 x 10	~ 160	Side 1 – as-grown Side 2 – polished
Single Crystal SC1	3 x 3	~ 400	Both polished

5.2 Transient Photoconductivity (TPC) Measurements

The apparatus employed for the measurement and analysis of transient photo-decay data is illustrated in Figure 5.2.1 below and includes: -

- Laser source - Laser Science Inc. VSL337 pumped nitrogen dye laser (λ = 337 nm, pulse length = 3 ns).
- Transient recorder - Gould DSO4074 400 Ms/sec 100 MHz digital storage oscilloscope.
- Bias voltage source - Keithley 230 programmable high-voltage source/measure unit.
- Cryostat – Oxford Instruments DN1704 liquid nitrogen variable temperature cryostat & ancillary ITC4 intelligent temperature controller.
- IBM compatible PC, equipped with an IEEE488.2 interface card – allowing control of the test equipment and collection of results by the custom data acquisition and analysis software developed in-house.

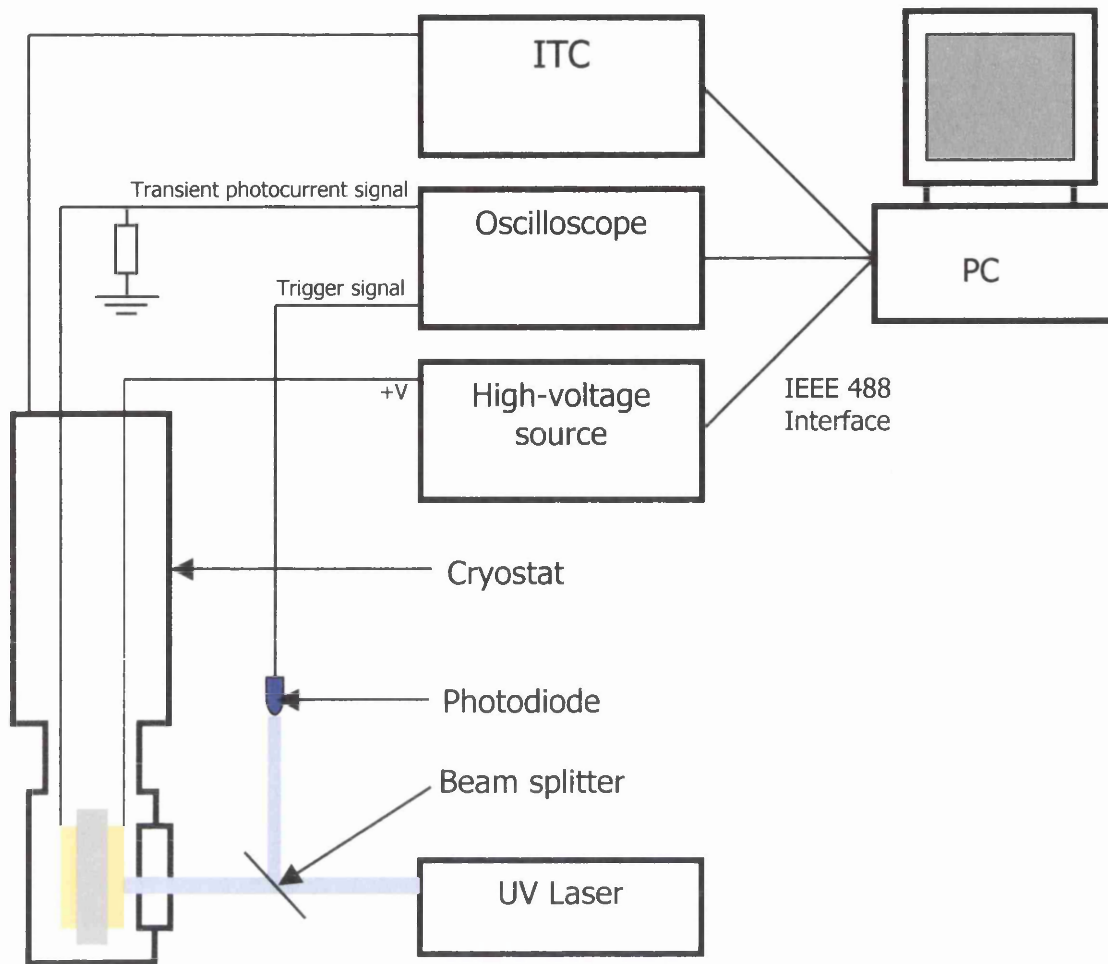

Figure 5.2.1: Experimental Apparatus Set-up.

Utilizing the TOF sandwich configuration described in the previous chapter, illumination was delivered to the specimen as a short pulse (3 ns) from the nitrogen laser (337 nm). This wavelength is sub-bandgap for diamond and therefore relatively weakly absorbed, with optical absorption coefficients reported [1] to be in the range 1 – 10 cm^{-1} for the best quality materials. Additionally, at this wavelength constant photocurrent measurement studies [2] have indicated that only around 10% of the absorbed photons contribute to the consequent photocurrent. Nevertheless, in the relatively thick (≥ 100 μm) samples available to this study, adequate concentrations of photo-stimulated carriers were generated to produce photocurrents measurable

over an extended time range (10^{-8} s to > 1 s) at room temperature, without the need for amplification. The bias voltage applied to the front (illuminated) electrode was pulsed only during the illumination-measurement cycle, to minimise the effects of dielectric relaxation and space-charge accumulation. Additionally, the time between measurements was sufficient to allow dissipation of any residual polarisation or injected charge, so that no detectable differences between individual photocurrent measurements could be detected. The photocurrent signals were recorded using the digitising storage oscilloscope detailed above. To enable measurements at different time ranges, the measurement resistor was progressively increased (with increasing time) from 50 Ω to 10^6 Ω, with any data for which the resistance value was sufficient to cause integration of the transient pulse being discarded. Measurements were made over a range of timescales and data combined to produce a composite image of the photo-decay. Results of the above measurements are located in the following chapter.

5.3 Residual Field Measurements

It was observed at an early stage in the present investigation that prolonged application of a D.C. bias voltage to the specimen caused considerable space-charge injection, (also observed by other investigators [3]) resulting in the creation of an internal field which was of a measurable magnitude long after the bias voltage was removed. To explore this phenomenon, a voltage (250 V) was applied to the specimen for a selected period (5 s) and then removed. After a subsequent delay (upto 15 hours), the specimen was exposed to a pulse from the laser. This created a transient current resulting from the photo-carrier movement in the residual field.

Integration of this provided a measure of the total charge displacement, and thus of the magnitude of the space-charge related field. Between individual measurements, the specimen was discharged of any residual space charge by exposure to repeated pulses from the laser in the absence of any applied field. Results of this investigation are located in the following chapter.

References

[1] Sussman R S, Brandon J R, Coe S E, Pickles C S J, Sweeney C G, Wasenczuk A, Wort C J H, Dodge C N (1998) *Industrial Diamond Review* **58** 69.

[2] Rohrer E, Graeff C F O, Nebel C E, Stutzmann M, Guttler H, Zachai R (1997) *Materials Science and Engineering B* **46** 115.

[3] Nebel C E, Stutzmann M, Lacher F, Koidl P, Zachai R (1998) *Diamond and Related Materials* **7** 556-559.

6 RESULTS

The following section contains the results of transient photoconductivity and residual space-charge measurements. These are displayed in graphical form and followed by a brief description of the observed behaviour.

6.1 Transient Photoconductivity Results

Figure 6.1.1 below displays the transient photo-decay data for the polycrystalline thin-film diamond sample JMM2. Measurements were performed at 295K using gold-on-titanium semi-transparent electrodes. Illumination took place at the growth surface and the applied bias voltage was 150 V.

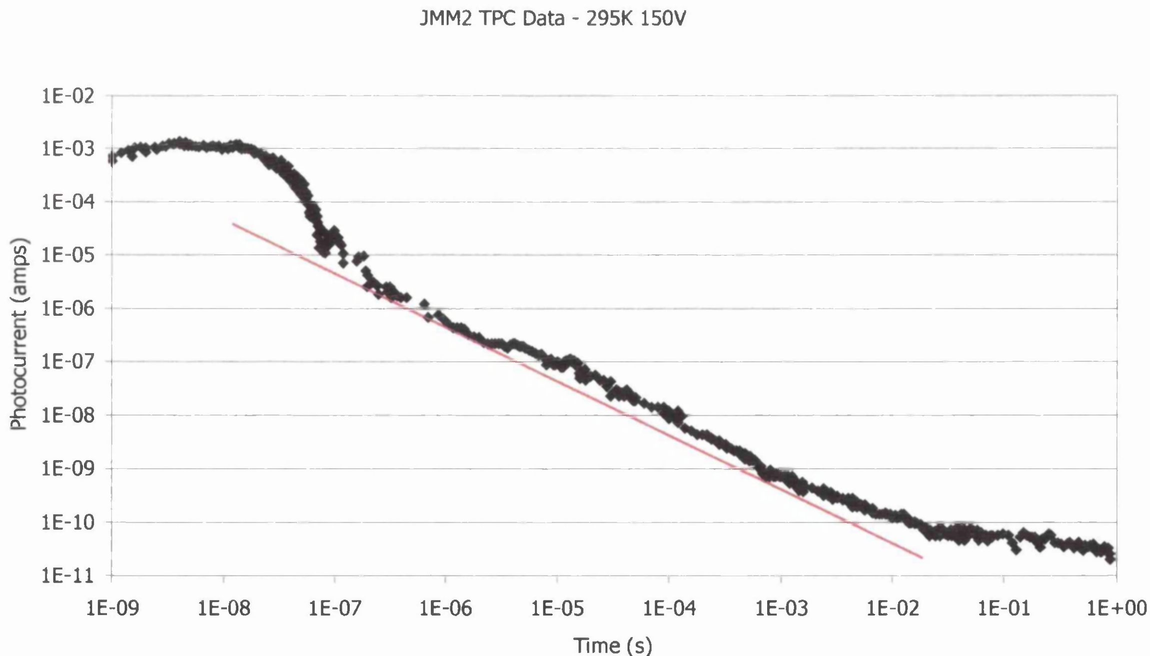

Figure 6.1.1: TPC Results for JMM2 at 295 K, 150 V (red line shown to highlight bump feature).

It is clearly visible in the chart displayed above that there is a moderate degree of noise on the signal. This can result in local distortions and apparent anomalous behaviour where the transient photocurrent is seen to increase with time, which in reality is not possible.

The data displayed above are typical of the photocurrent decay for a material of this type and have been observed by other authors making similar measurements [1] [2]. The decay is characterised by a flattish response at short times, followed by a sharp decline up to ~ 1×10^{-7} s, where a change in regime is apparent. There is then an almost linear decay up to ~ 5×10^{-2} s, where the signal begins to flatten. However, the red line inserted on the chart highlights the presence of a feature located between 1×10^{-6} s and 1×10^{-3} s.

The custom control and data acquisition software allowed the option of calculating the integrated area under the transient pulse. This resulted in a value of the total displacement of charge, Q, taking place within the specimen. From this, it could be determined whether significant carriers are lost due to completion of their transit across the specimen. Using the Hecht procedure, described in Chapter 4, the result was a linear increase in Q with electric field. Therefore, even at very high fields very few carriers appeared to be completing their transits.

Results of experiments performed at different temperatures and on different specimens are displayed below. They are seen to be broadly similar to those presented above, with variations in detail resulting from differences in the physical

properties of individual specimens and the way in which the time-evolution of the photocurrent varies with temperature. It is important to note that although the differences in the transient photocurrent data may appear very small, they can have a significant influence upon the form of the calculated density-of-states, $N(E)$.

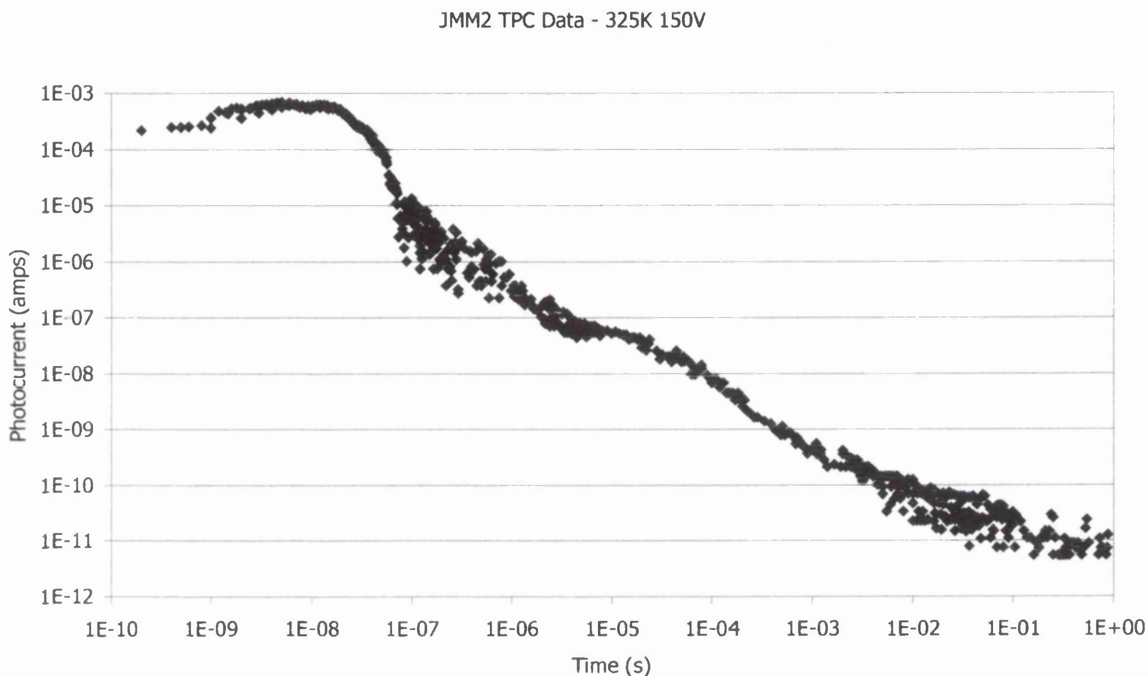

Figure 6.1.2: TPC Results for JMM2 at 325 K, 150 V.

The results displayed in Figure 6.1.2 above illustrate the time-evolution of the photocurrent in specimen JMM2 at temperature 325 K and applied voltage 150 V. Initially, the results appear broadly the same as those collected at 295 K. However, it is clear on closer examination that the photocurrent decays more quickly at the higher temperature, dropping below 1×10^{-11} A after 1 second. Whereas, although the data requires some extrapolation, at 295 K this level would not be reached until approximately 10 seconds. This behaviour is consistent with the thermalisation concept described in chapter 4.

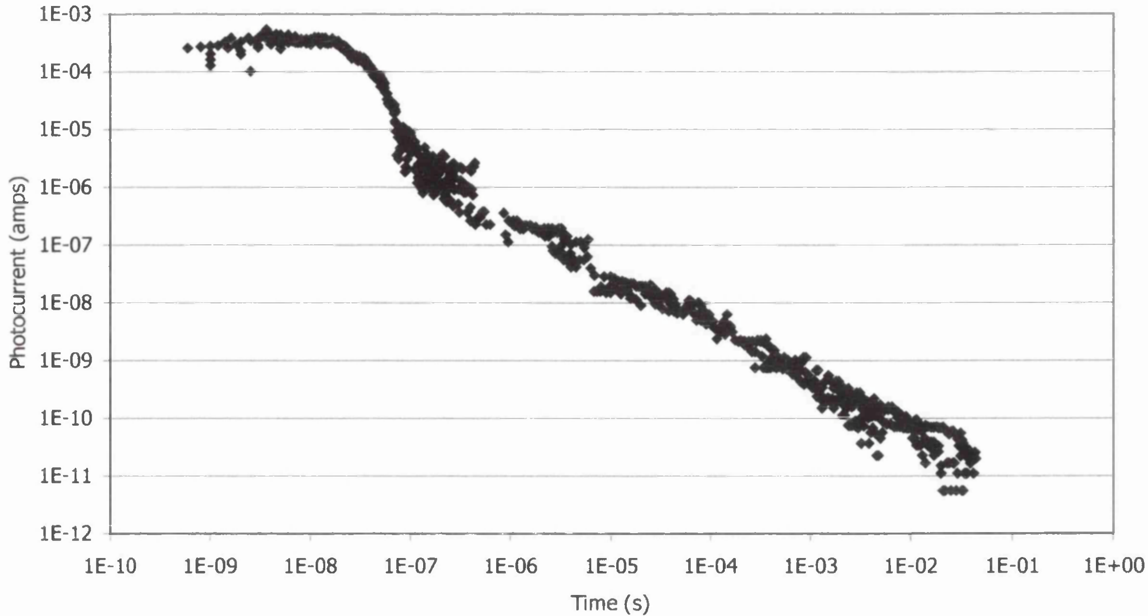

Figure 6.1.3: JMM2 TPC Results at 340 K, 150 V.

Although the general trend is preserved in Figure 6.1.3, it is again apparent that the photocurrent decays more rapidly with increased temperature. Above it is shown that the photocurrent has fallen to a level of 1×10^{-11} A after 0.1 s.

At this point it is important to mention that when the photocurrent falls below 1×10^{-11} A, the degree of noise experienced on the signal renders further measurement below this level unviable with the current experimental set-up. It is possible that different / additional experimental equipment may allow measurement of very small photocurrents, and this is discussed in later sections.

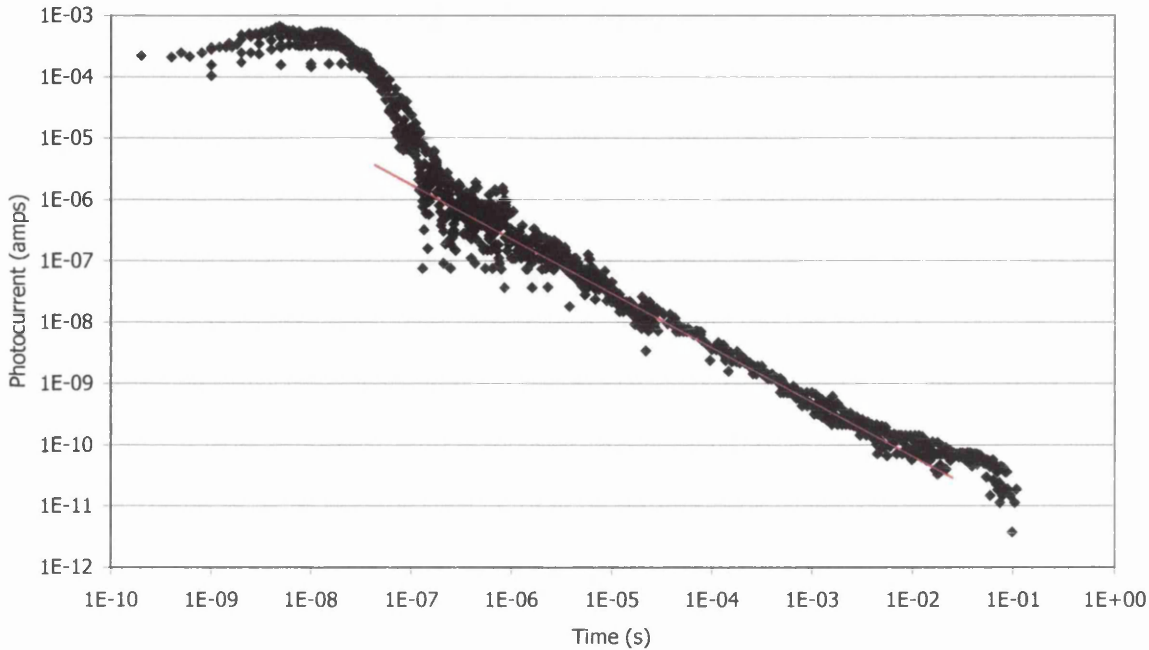

Figure 6.1.4: JMM2 TPC Results at 350 K, 150 V.

The data in Figure 6.1.4 appear inconsistent with the previous charts, as the photocurrent does not appear to decay more quickly at the increased temperature. If compared closely with the data for 340K, the decay appears approximately equivalent. Based on the data for lower temperatures displayed previously, a decrease in the decay time would be expected. However, it is possible that deeply trapped carriers are now being released at shorter times due to thermal re-emission, resulting in an extension of the photocurrent decay. Additionally, the feature previously located between 1×10^{-6} and 1×10^{-3} s has been significantly smoothed out.

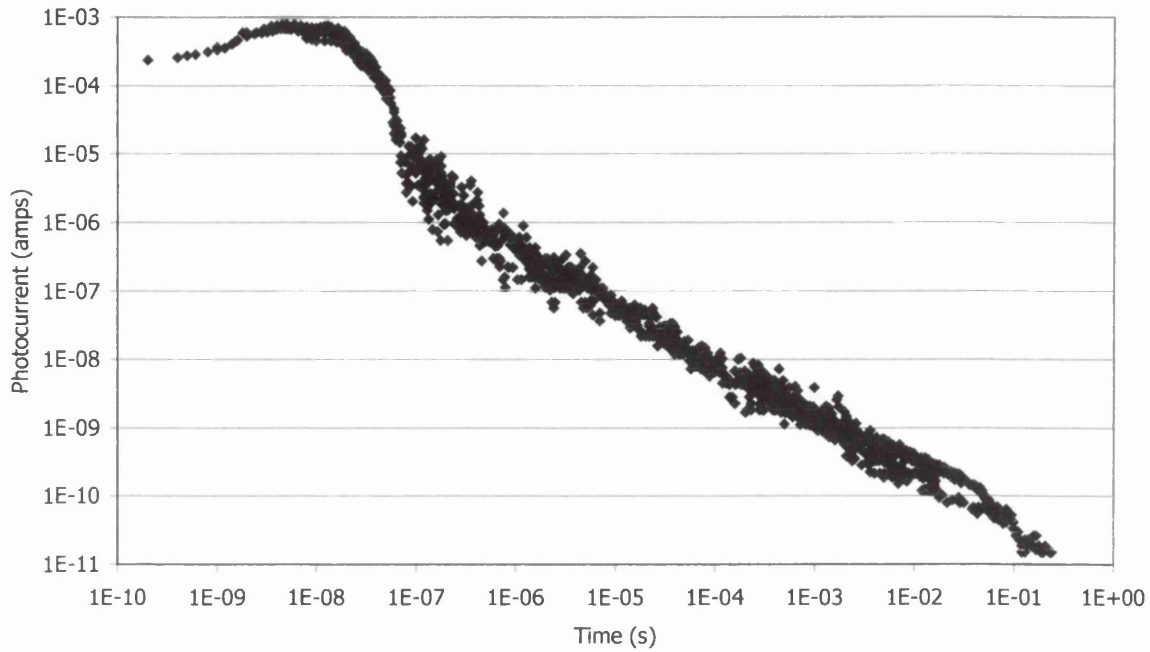

Figure 6.1.5: JMM2 TPC Results at 390 K, 150 V.

Again, in Figure 6.1.5 an increase in the net decay time of the photocurrent is evident, accompanied by further smoothing of the lump feature.

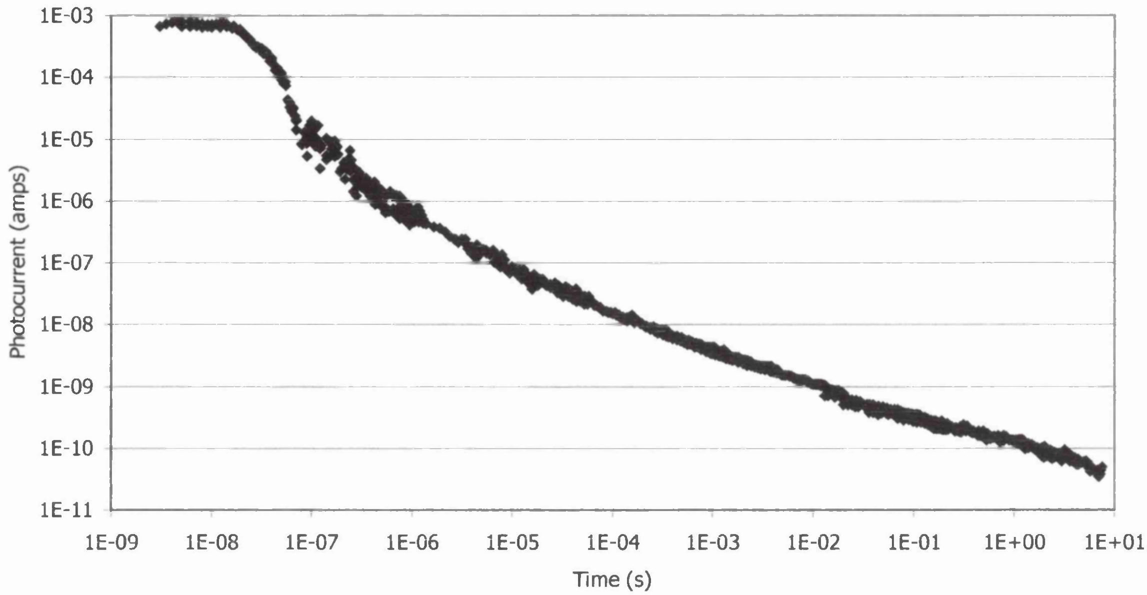

Figure 6.1.6: JMM2 TPC Results at 450 K, 150 V.

Figure 6.1.6 shows that at this high temperature, the photocurrent is observed to persist at measurable levels for significantly longer times (~ 10 s). Additionally, if the data is extrapolated, the 1 x 10^{-11} A level will not be reached until approximately 100 s has passed since the initial photo-excitation of the specimen. Again, this is attributed to the release of deeply trapped carriers that would, at lower temperatures, remain trapped outside the experimentally accessible time-range.

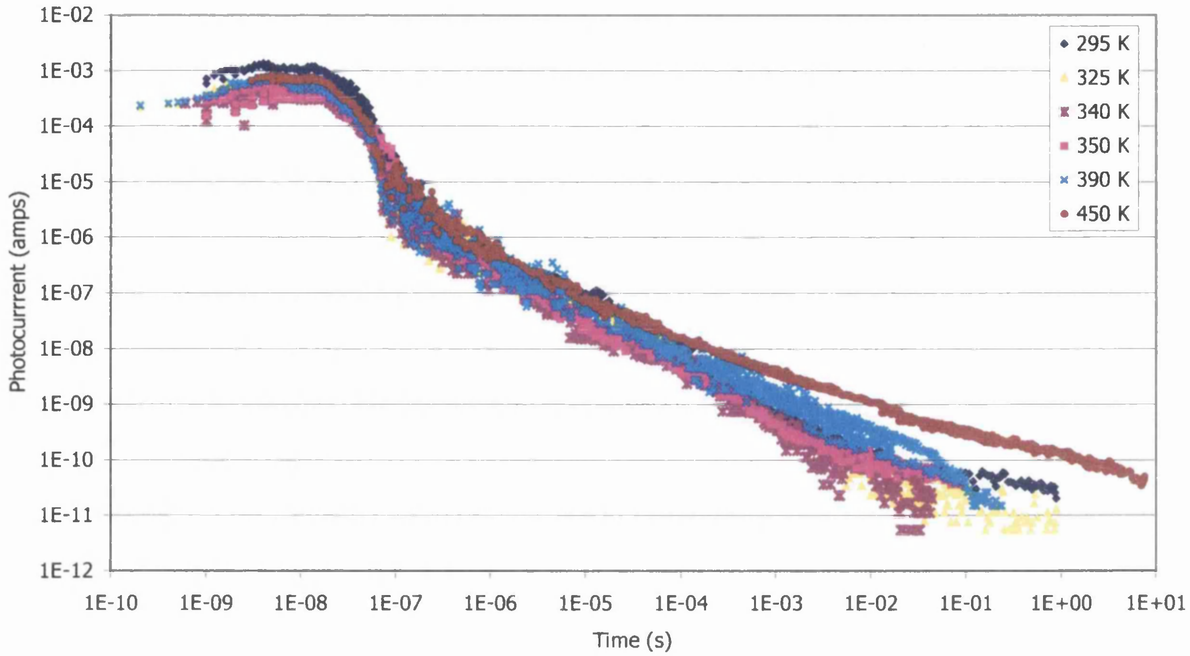

Figure 6.1.7: Compiled TPC Results for JMM2.

Figure 6.1.7 above attempts to illustrate more clearly the gradual change in detail of the transient photocurrent decay for polycrystalline diamond specimen JMM2, as the experimental operating temperature is progressively increased.

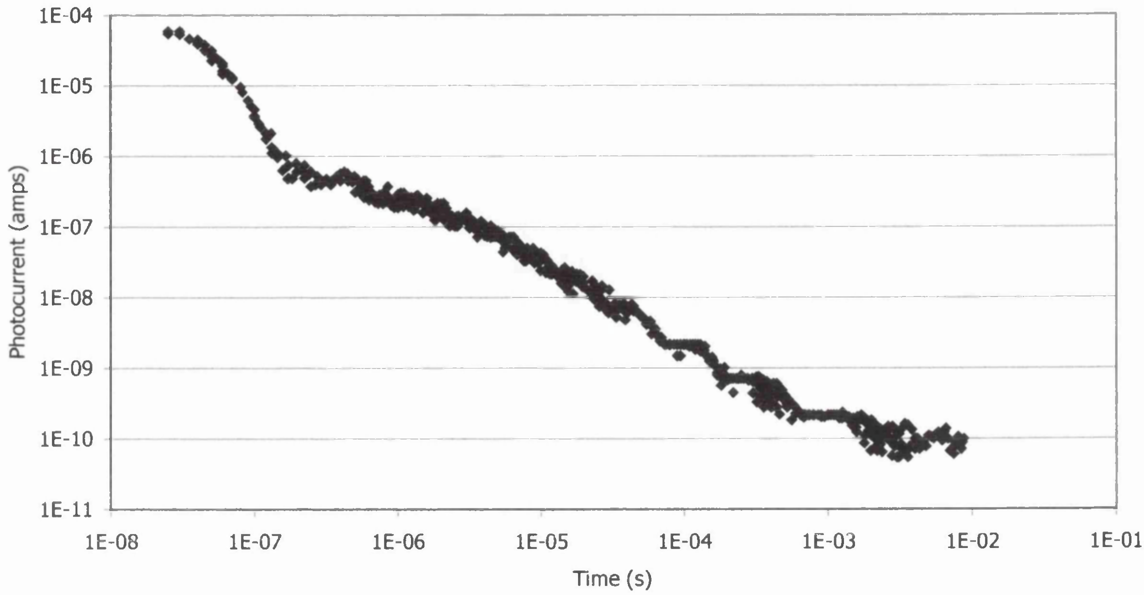

Figure 6.1.8: JMM4 TPC Results Side 1 at 300 K, 200 V.

During the growth of JMM4, the conditions in the CVD reactor were significantly altered with respect to the concentration of one of the gaseous species in the chamber. For commercial reasons the details of this cannot be revealed. However, it was hypothesised that this would result in significant differences in the photo-response of the two surfaces. With respect to this, Figures 6.1.8 and 6.1.9 illustrate the transient photoconductivity data for Side 1 and Side 2 respectively.

Unfortunately, both surfaces of the specimen were supplied polished on this occasion, so it was impossible to determine visually between the growth and nucleation surfaces. However, the TPC data for Side 1 is consistent with that observed for the growth surface of other specimens, whereas the data for Side 2 differs significantly from that observed previously in this study and by other authors.

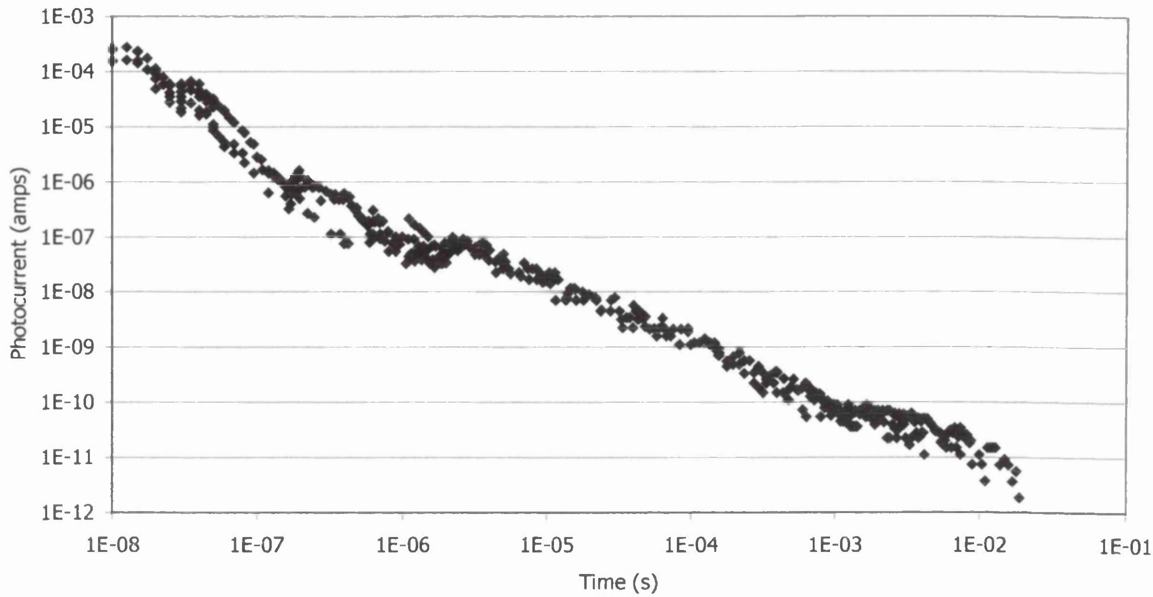

Figure 6.1.9: JMM4 TPC Results for Side 2 at 300 K, 200 V.

In Figure 6.1.9 above, there appears to be a smearing of the two regimes that are usually marked by a more pronounced change in gradient at a time close to 1 x 10^{-7} than is observed on this occasion. This is also attributable to the reasons outlined above. It is likely that this is some function of the increased proportion of grain boundary related defects associated with the nucleation surface.

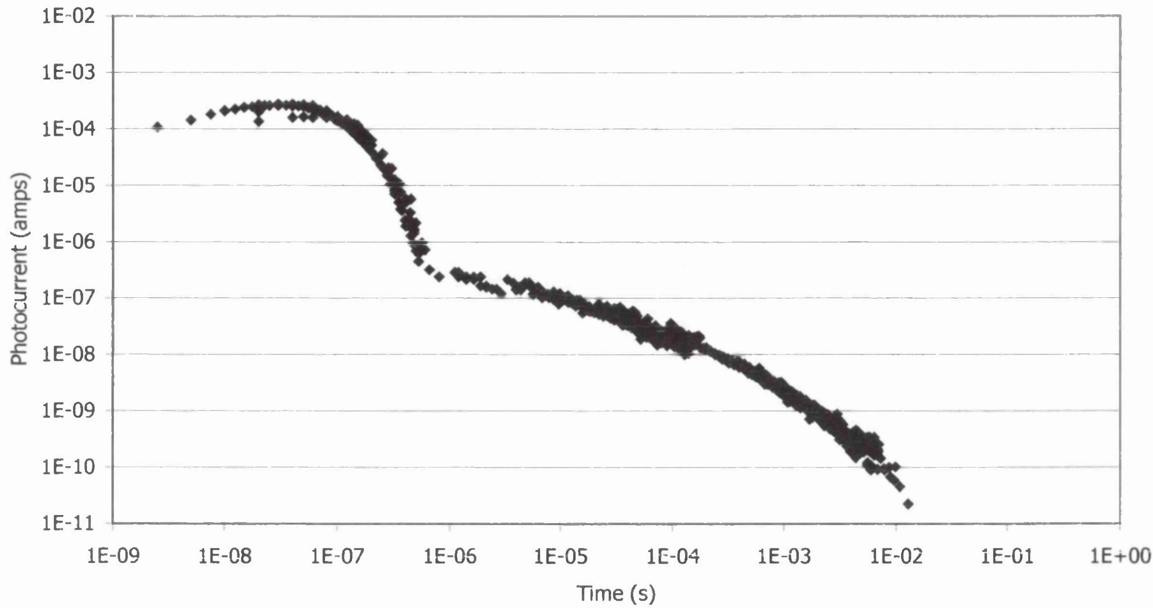

Figure 6.1.10: TPC Results for JMM5 at 300 K, 150 V.

Specimens JMM5 and JMM6 are known to be identical in most respects, except that there is at least an order of magnitude difference in nitrogen concentration between the two specimens. Again, due to commercial sensitivity, actual growth conditions and specimen compositions are restricted.

Initially, it is clear that although the classic decay shape observed earlier is preserved, the previously seen feature (centred at ~ 1×10^{-4} s) is considerably more pronounced. Additionally, whereas in previous specimens there has been an indication of the decay flattening out at long times (> 0.1 s), the data for JMM5 display a complete opposite of this behaviour. This has been observed by other authors in polycrystalline diamond displaying a high degree of orientation with respect to the grain structure of the material [1]. This material, termed highly orientated diamond (HOD), is a result of low nitrogen growth conditions.

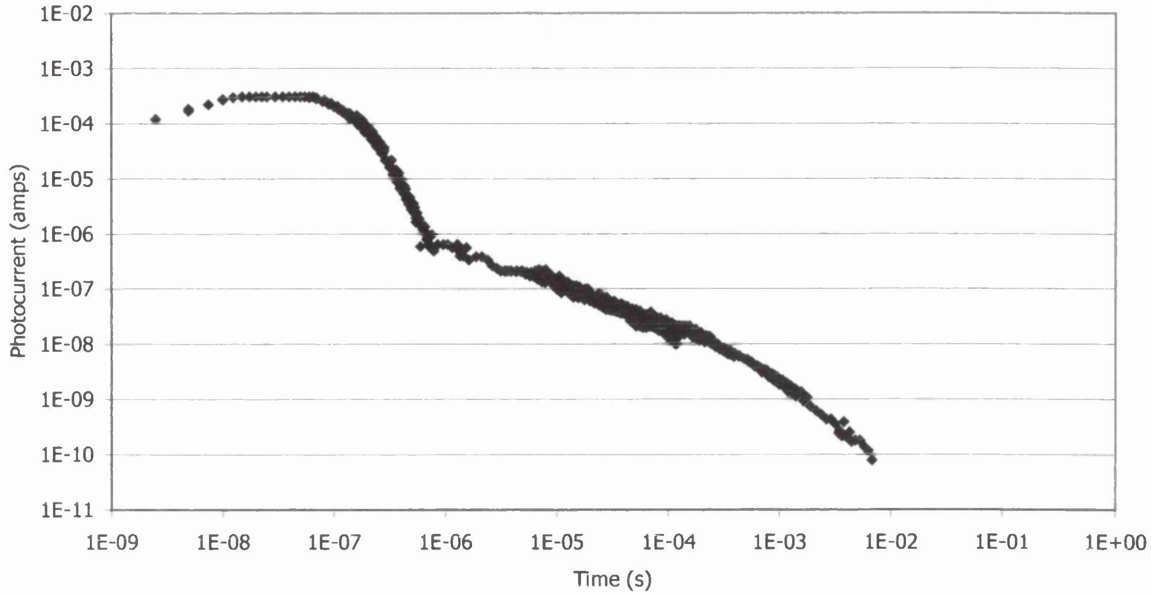

Figure 6.1.11: TPC Results for JMM5 at 320 K, 150 V.

Figure 6.1.11 above illustrates the transient photocurrent data for specimen JMM5 at 320 K. The photo-decay is not noticeably different to the data gathered at 300 K.

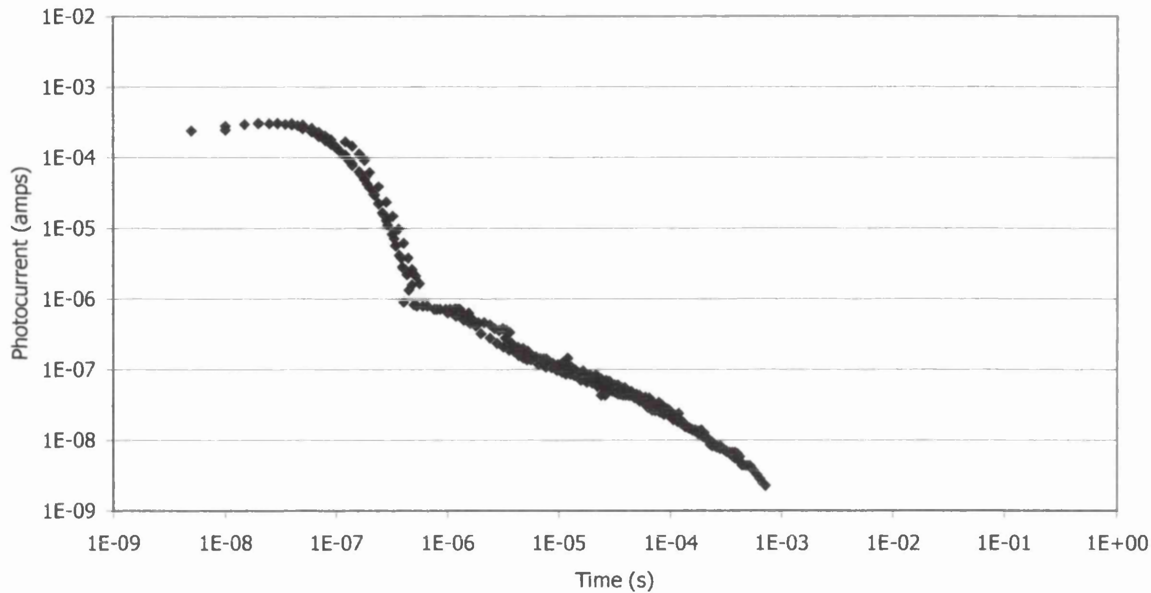

Figure 6.1.12: TPC Results for JMM5 at 350 K, 150 V.

Again, the data for JMM5 at 350 K illustrated in Figure 6.1.12 above, is not significantly different from that collected at 300 K and 320 K as Figure 6.1.13 below demonstrates. However, the signal quality degraded to such an extent at times > 1 x 10^{-3} s that measurement below ~ 1 x 10^{-9} A became unviable.

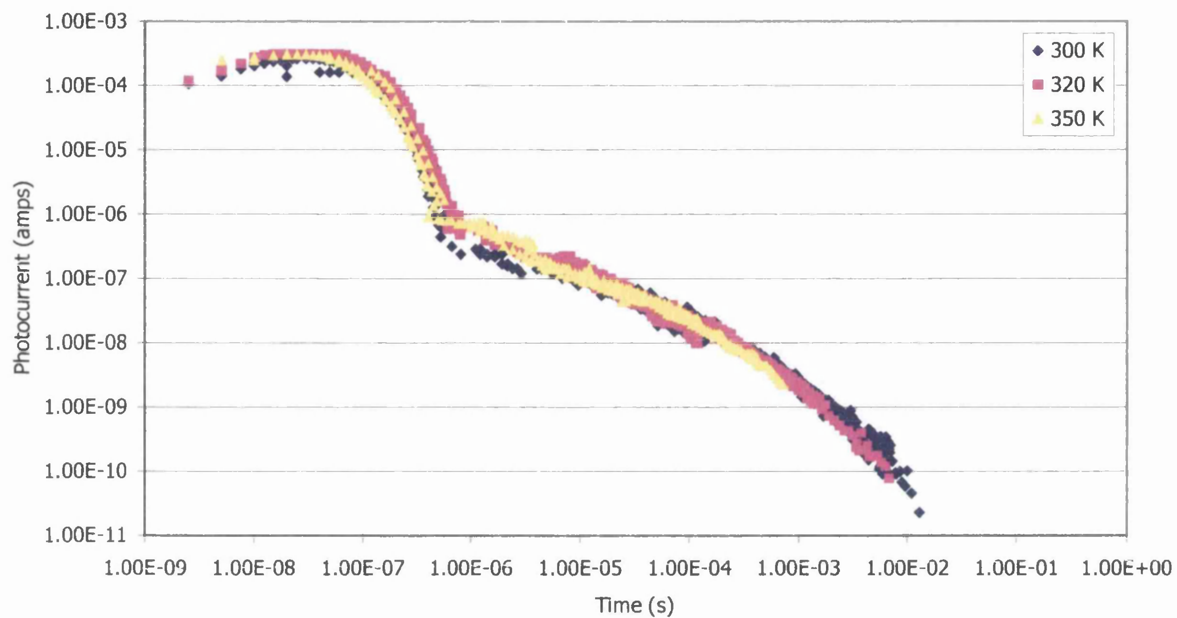

Figure 6.1.13: Compiled TPC Results for JMM5.

Figure 6.1.13 above highlights that there appears to be no significant change in the time-evolution of the photocurrent decay with increasing temperature for polycrystalline diamond specimen JMM5.

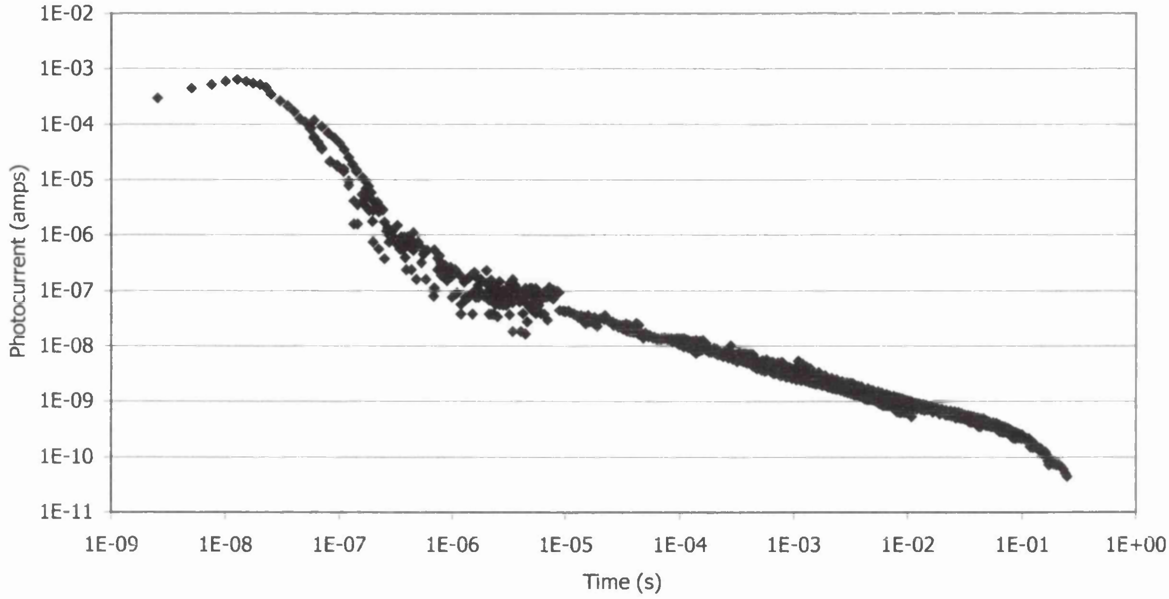

Figure 6.1.14: TPC Result for JMM6 at 300K, 150V.

Again, the TPC data illustrated in Figure 6.1.14 are fairly typical for a material of this type. However, the feature observed in earlier specimens, and most noticeably in the previous specimen JMM5, does not appear to be present on this occasion.

This behaviour is consistent with that observed by other authors in polycrystalline diamond (PD), displaying a low degree of orientation with respect to the grain structure of the material [1].

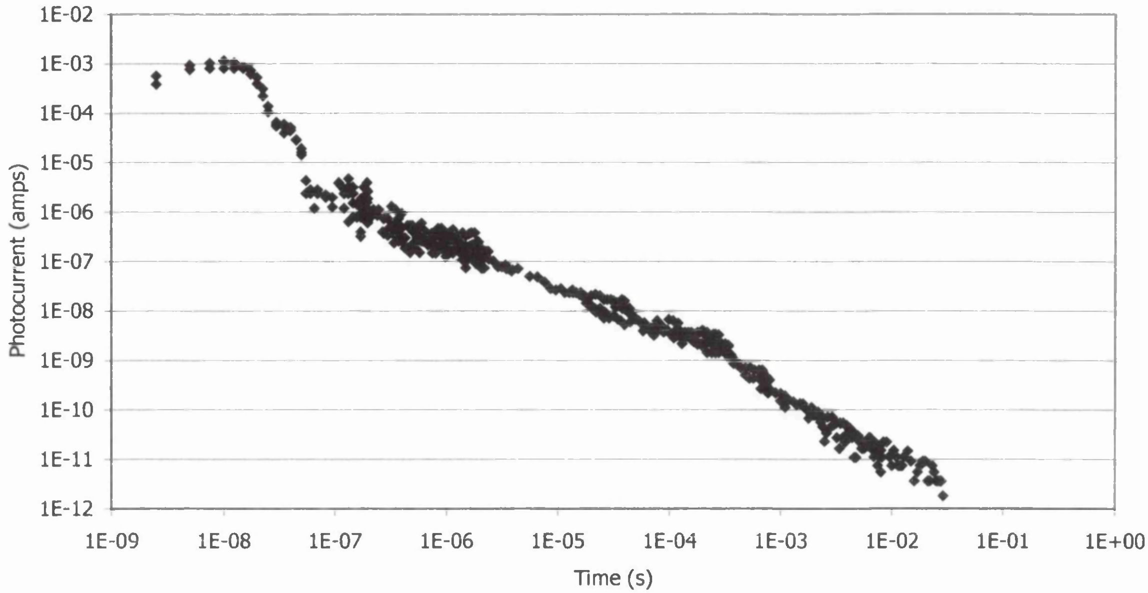

Figure 6.1.15: TPC Results for HPHT Diamond at 300K, 150V.

The transient photoconductivity results for HPHT single-crystal diamond (Figure 6.1.15) are very much the same as those recorded for polycrystalline CVD diamond in many respects with regard to the shape of photocurrent decay. In particular, the common features are preserved - the sharp fall-off until ~ 1×10^{-7} s followed by a marked change in gradient and steady decay until the minimum resolution of the experimental set-up is reached. There also appears to be some evidence of the previously observed localised state feature located at ~ 10^{-4} s.

6.2 Residual Space-Charge Field Results

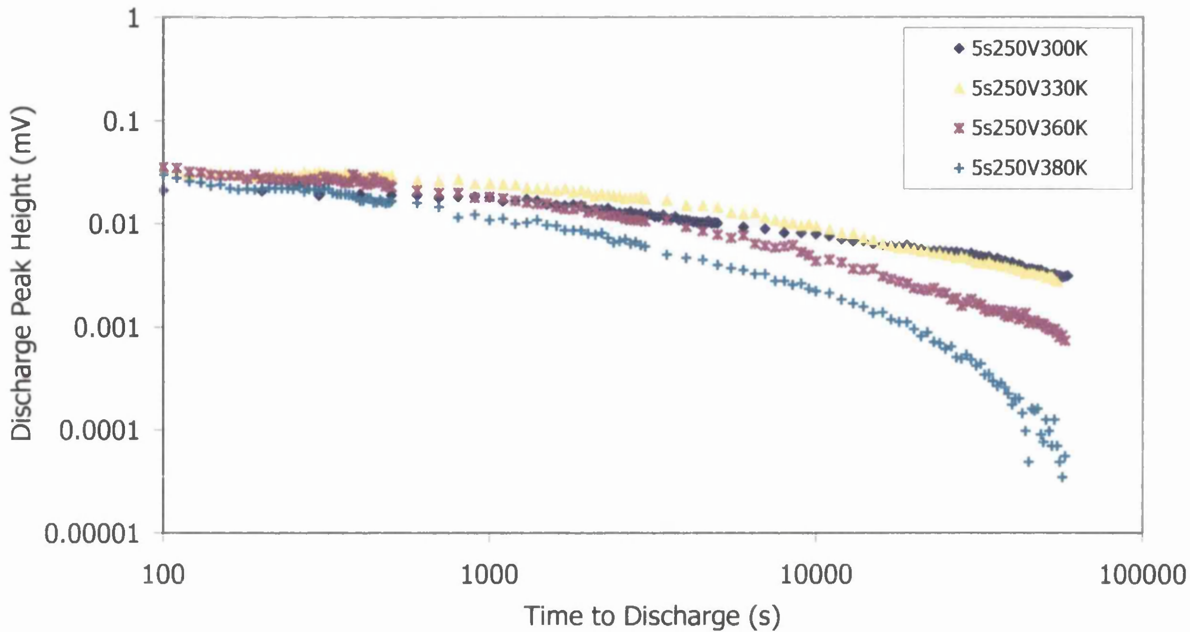

Figure 6.2.1: Time-Evolution of the Residual Field Decay.

Initially, it is again evident from the data presented in Figure 6.2.1, that the residual field persists over a considerable time-range (> 15 hours), inferring that significant numbers of charge carriers are being deeply trapped without thermally activated re-emission during the experimentally accessible time-frame. Clearly, the space-charge decays more quickly with increasing temperature, but does not otherwise appear dependent on temperature with respect to the time-evolution of the response (i.e. the behaviours at short times are very similar).

References

[1] Nebel C E, Stutzmann M, Lacher F, Koidl P, Zachai R (1998) *Diamond and Related Materials* **7** 556-559.

[2] Salvatori S, Rossi M C, Galluzzi F, Riedel D, Castex M C (1999) *Diamond and Related Materials* **8** 871-876.

7 DISCUSSION

In the following section, the experimental results and subsequent analysis are discussed and interpreted with respect to the electronic properties of CVD and HPHT synthetic diamond.

7.1 Transient Photo-Response

Initially, it is clear from the TPC results that the photocurrent persists over a significant timescale. This indicates that the dominant charge carriers are interacting with considerable concentrations of localised states distributed over a broad range of energy. Therefore, it can be concluded that it is appropriate to apply the analytical procedures described in previous sections.

Integrated photocurrent calculations have determined that few if any charge carriers are lost by completion of their transit during the experimentally accessible time-scale. This infers that it would be appropriate to consider the data to be in the pre-transit regime. However, as explained in Chapter 5, it is appropriate to employ the post-transit analysis procedure if significant levels of recombination or deep trapping occur, or if a sufficiently structured density-of-states, $N(E)$, is present. Figure 7.1.1 below, displays the post-transit analysis for the TPC data shown in Figure 6.1.1 for polycrystalline CVD diamond specimen JMM2. Here, and throughout the current study, the value of ν used for defining the energy axis was 10^{12} Hz. It is theoretically possible to evaluate the value of ν by comparing results obtained at different temperatures [1]. However, 10^{12} Hz is currently consistent with the value employed

by other authors [2] and an incorrect estimate of ν will simply displace the $N(E)$ data linearly along the energy axis (provided ν does not vary with the depth of centres). Additionally, any displacement is unlikely to be large, as an error of an order of magnitude in ν will result in a displacement of only 0.05 eV. Also, as the parameters necessary for determining the constant C' in Equation 4.3.3 have either been assumed or not determined here, the $N(E)$ axis is in relative units.

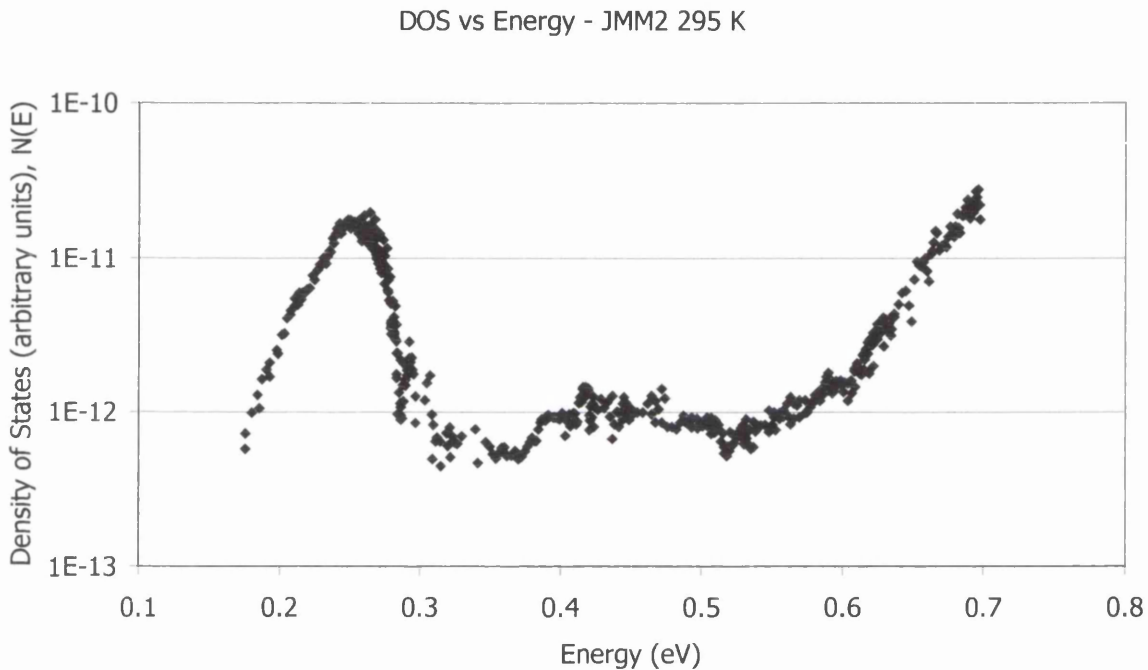

Figure 7.1.1: Post-Transit Analysis for JMM2 at 295 K, 150V.

As explained previously, the transform technique is almost completely insensitive to the presence of recombination or to whether the data refer to the pre- or post-transit regimes. The result of applying this procedure to the TPC data in Figure 6.1.1 is displayed in Figure 7.1.2 below. Both the transform and the post-transit analysis procedures result in a computed density of localised states with similar features in similar positions along the energy axis. In contrast, application of the pre-transit

analysis procedure would produce a complete inversion of the post-transit calculation for the reasons described in previous sections. This would be highly inconsistent with the transform results and is to be expected for the structured energy distribution present. Thus, this procedure can be discounted.

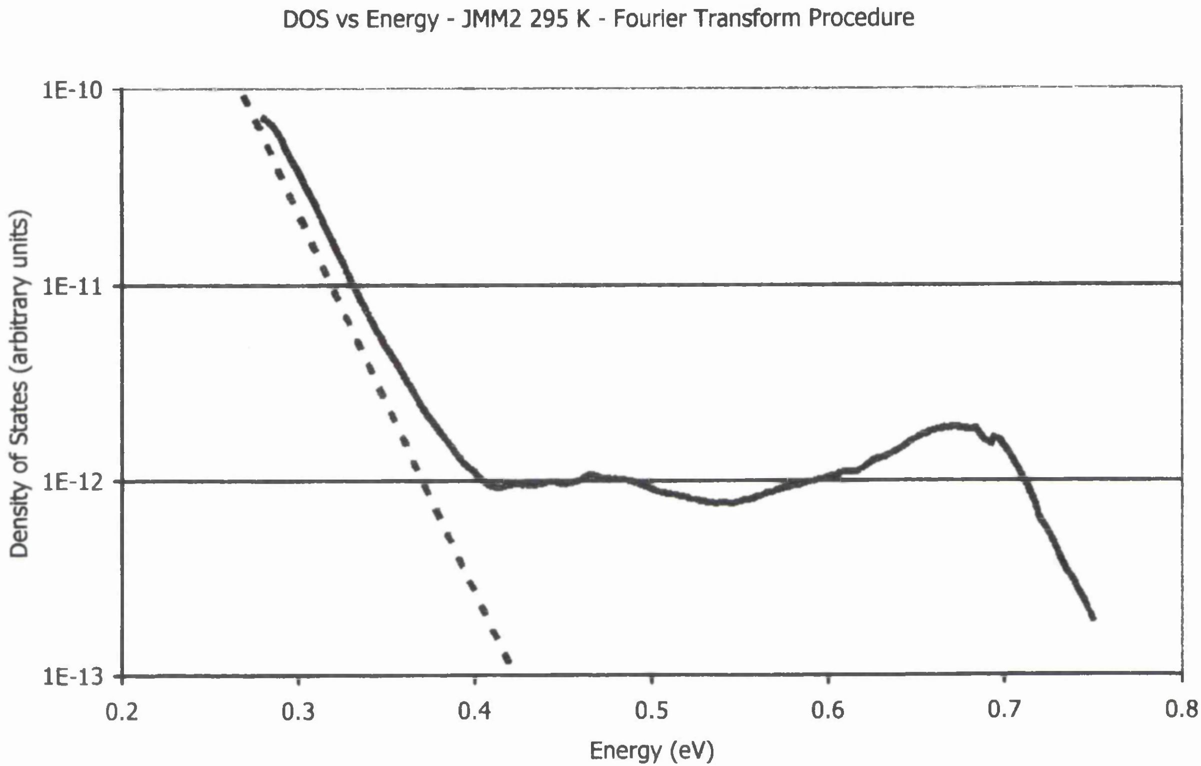

Figure 7.1.2: Fourier Transform Analysis for JMM2 at 295 K, 150V.

The post-transit analysis exhibits a falling $N(E)$ below energies of around 0.25 eV. This is an artefact of the procedure, as it has been demonstrated to become invalid at sufficiently short times [1] [3]. Similarly, the transform technique results in a decreasing $N(E)$ for energies greater than around 0.7 eV. This is also an artefact of this particular procedure associated with the effects of the truncation of the $I(t)$ data at a non-zero value at the upper end of the time range.

Taking into account the differences described above, the results generated by the post-transit analysis and the transform procedure provide relatively good agreement. Thus, attention can be focused on the differences in detail of the two techniques and whether either is a true representation of the actual energy distribution of localised states.

The largest degree of distortion occurs in both procedures due to 'kT broadening' effects. The transform technique, in particular, cannot reproduce energy variations rising or falling more quickly than $\exp\left(\pm\frac{E}{kT}\right)$. Therefore sharp features become blurred out. This effect has been demonstrated by recent computer modelling studies [4] and is illustrated by the dotted line in Figure 7.1.2 which represents an $\exp\left(\frac{-E}{kT}\right)$.

The computer modelling studies mentioned above have indicated that although the post-transit technique also generates a kT broadening effect for energies rising more sharply than $\exp\left(\pm\frac{E}{kT}\right)$ with trap depth, this may not be the case for $N(E)$ decreasing rapidly with depth. This explains the sharper fall in the computed $N(E)$ between 0.25 – 0.3 eV and consequently the more clearly defined 'trough' in $N(E)$ close to 0.35 eV observed in the post-transit analysis 7.1.1. On this basis, the post-transit analysis procedure is deemed to be more sensitive, and therefore provides a more accurate representation of the density of localised states for the data gathered in this study. However, the pioneers of the transform technique have reported [5]

recent advances in the procedure that appear to reduce the broadening effects described above. Such developments may prove advantageous to continued work on this study.

A model density of states consistent with the observed experimental data has been developed, consisting of a steep exponential band-tail at the band edge plus three Gaussian features (Eq. (7.1.1)).

$$N(E) = \exp\left(\frac{-E}{0.008}\right) + \left(\frac{A_1}{W_1\sqrt{\pi/2}}\right)\exp\left[\left(\frac{(E-C_1)}{W_1}\right)^2\right] + \left(\frac{A2}{W_2\sqrt{\pi/2}}\right)\exp\left[\left(\frac{(E-C_2)}{W_2}\right)^2\right] + \left(\frac{A_3}{W_3\sqrt{\pi/2}}\right)\exp\left[\left(\frac{(E-C_3)}{W_3}\right)^2\right]$$

Eq. (7.1.1)

Here, C_{1-3} represent the central energies of the Gaussian features, W_{1-3} the distributions in energy of the states, and A_{1-3} the amplitudes of the features. Specific values for the model are displayed in Table 7.1.1 below and the modelled data is illustrated in Figure 7.1.3.

Table 7.1.1: Model Parameters.

Parameter	Amplitude A	Centre C	Width W
1	7.61×10^{-13}	0.25	0.035
2	2.18×10^{-13}	0.45	0.16
3	9.00×10^{-13}	0.725	0.09

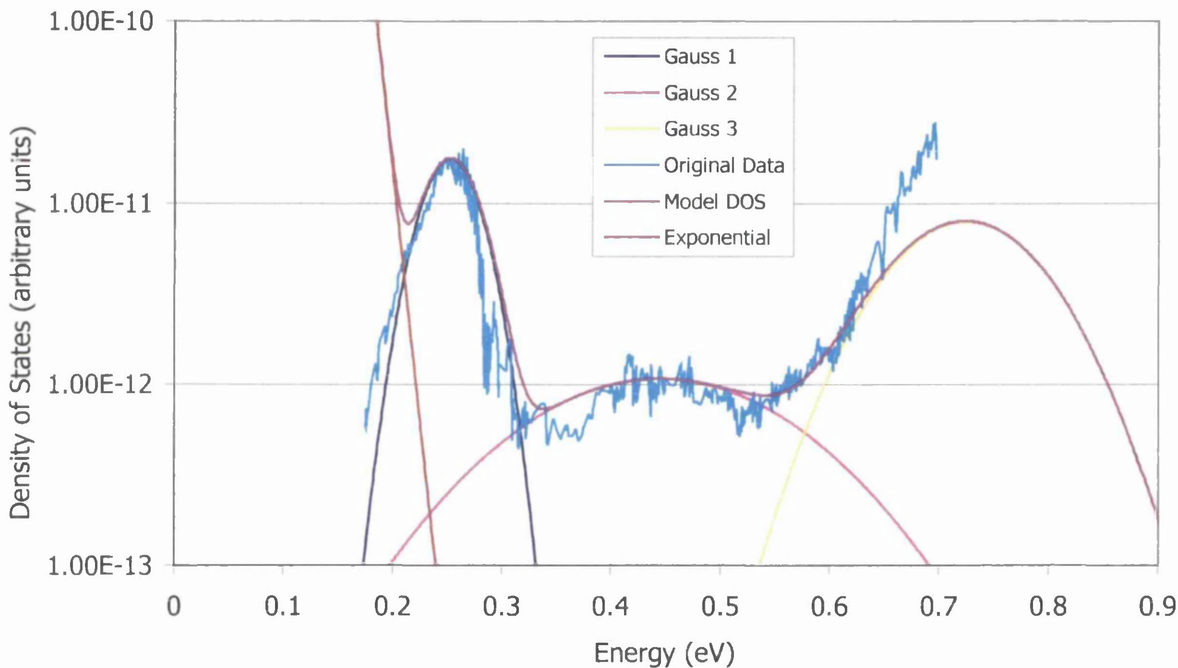

Figure 7.1.3: Energy Distribution of Localised States Developed to Model Transient Photo-Response Data in Figure 6.1.1.

The shallow exponential band-tail was included to provide continuity of the $N(E)$ to the band edge, as would normally be expected for disordered semi-conducting materials. In practice, the energy distribution in the shallow range 0 – 0.2 eV could be varied significantly without affecting the time-form of the photocurrent over the experimentally accessible time range. However, this function was selected to represent these states, as the presence of such a relatively well-defined set of

electron traps at a depth close to 0.2 eV has been inferred from other studies of transient photoconductivity using enhanced time resolutions (< 1 ns) [6]. These authors concluded that these centres were energetically distinct from the slightly deeper centres located at approximately 0.25 eV deemed to be located at grain boundaries.

The $N(E)$ beyond 0.7 eV is also somewhat speculative, as it too is outside the experimentally accessible energy range. The detail of the states is not overly significant to this investigation, but it should be noted that carrier losses into these deep states will occur during the experimentally probed timescale. It is therefore necessary to have a term representing a sufficient concentration of such centres, to produce $I(t)$ data similar to that measured experimentally. It should also be noted that few carriers falling into such states would be released within the experimental timescale.

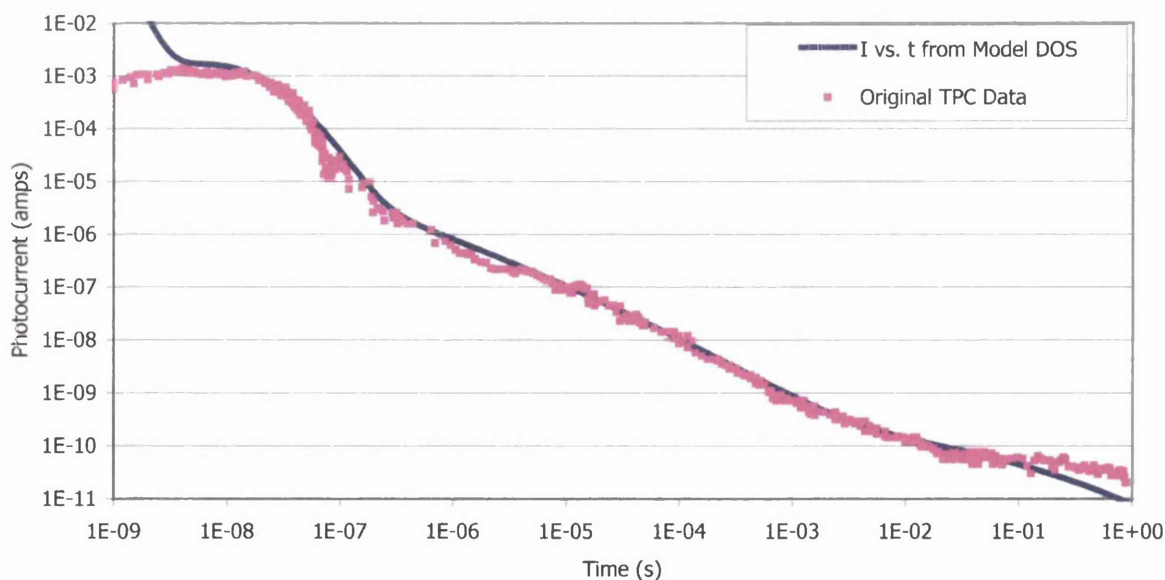

Figure 7.1.4: Original TPC Data Compared to Modelled Data.

Figure 7.1.4 clearly demonstrates that the model closely imitates the measured transient photo-decay over the majority of the experimentally accessible time-range.

The following graphs illustrate the density-of-states calculated via the post-transit analysis procedure for the TPC data displayed in the previous chapter.

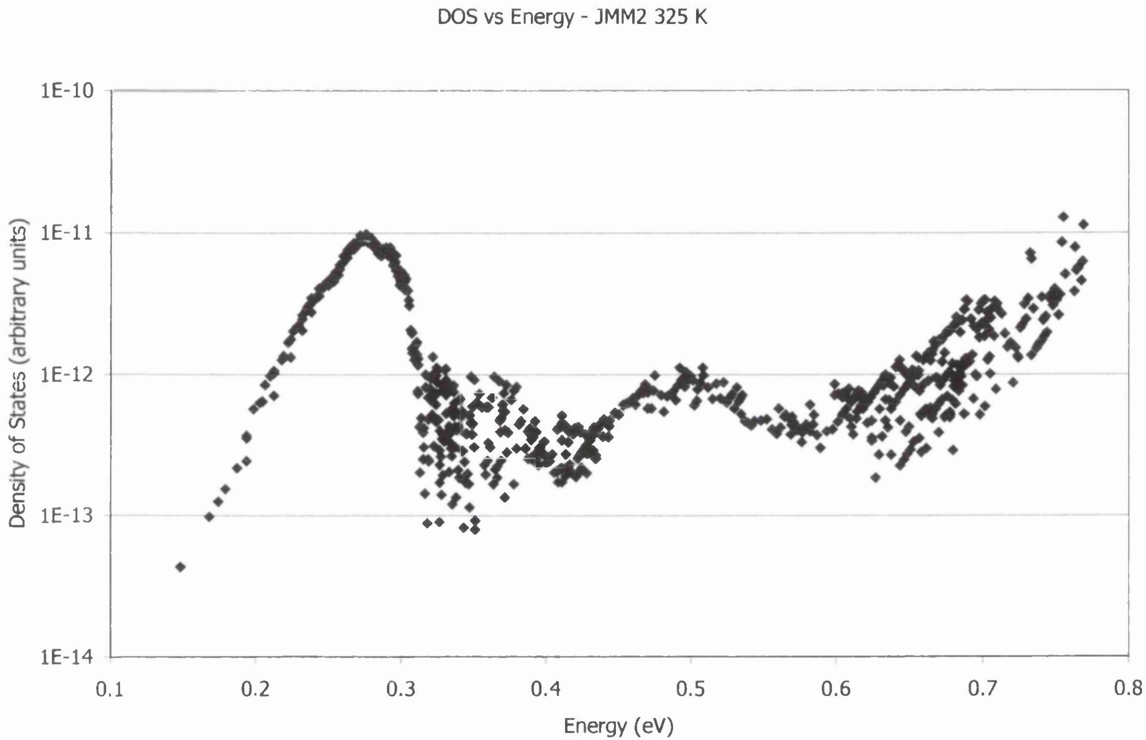

Figure 7.1.5: Calculated DOS for CVD Diamond Specimen JMM2 at 325 K.

From Figure 7.1.5, it is evident that the general form of the DOS is preserved and the three states previously identified are again present. Note however, the slight movement to deeper energies of the entire DOS. This effect is possibly a result of an incorrect estimate in the value of the constant, ν, and becomes more prominent as the measurement temperature is increased.

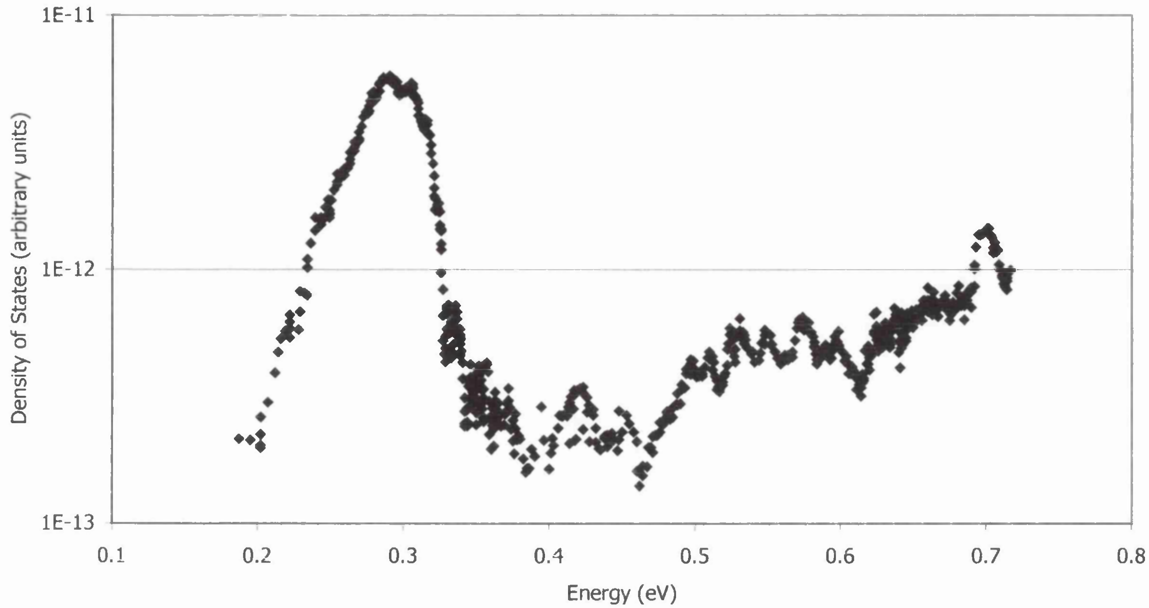

Figure 7.1.6: Calculated DOS for CVD Diamond Specimen JMM2 at 340 K.

The information in Figure 7.1.6 indicates that as the temperature is increased, the deepest centre identified appears to become more dominant at the expense of the central feature. This is likely to be the result of significant numbers of deeply trapped carriers being released at shorter times due to thermal stimulation. This behaviour becomes increasingly evident as the temperature is increased (Figures 7.1.7 – 7.1.9) until the central feature is no longer distinguishable from the deepest one.

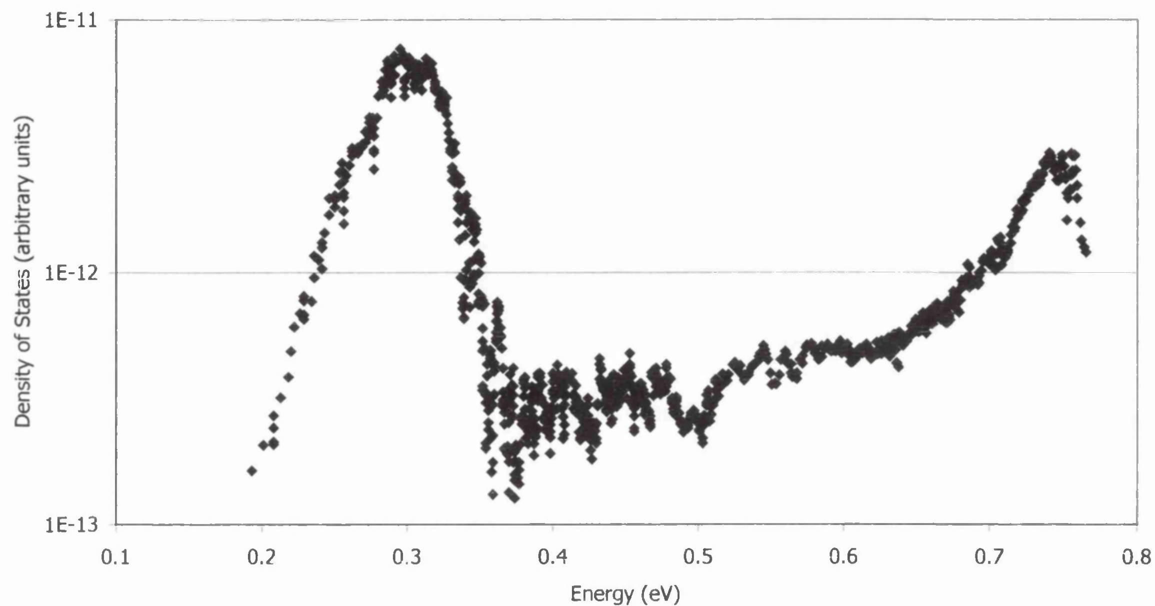

Figure 7.1.7: Calculated DOS for CVD Diamond Specimen JMM2 at 350 K.

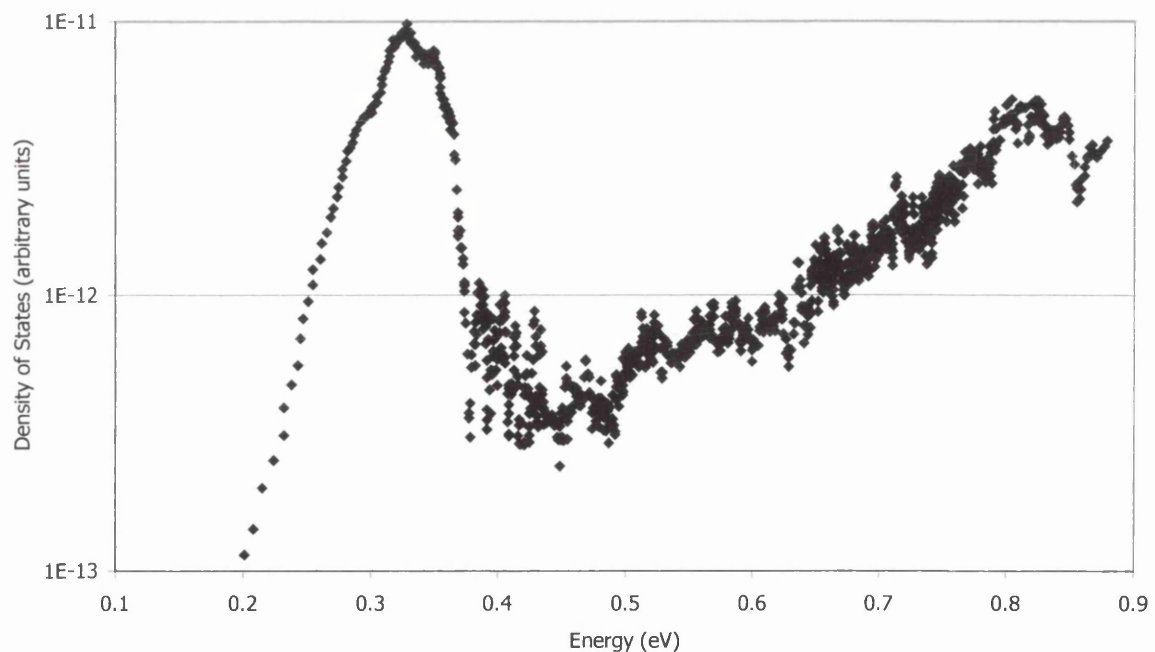

Figure 7.1.8: Calculated DOS for CVD Diamond Specimen JMM2 at 390 K.

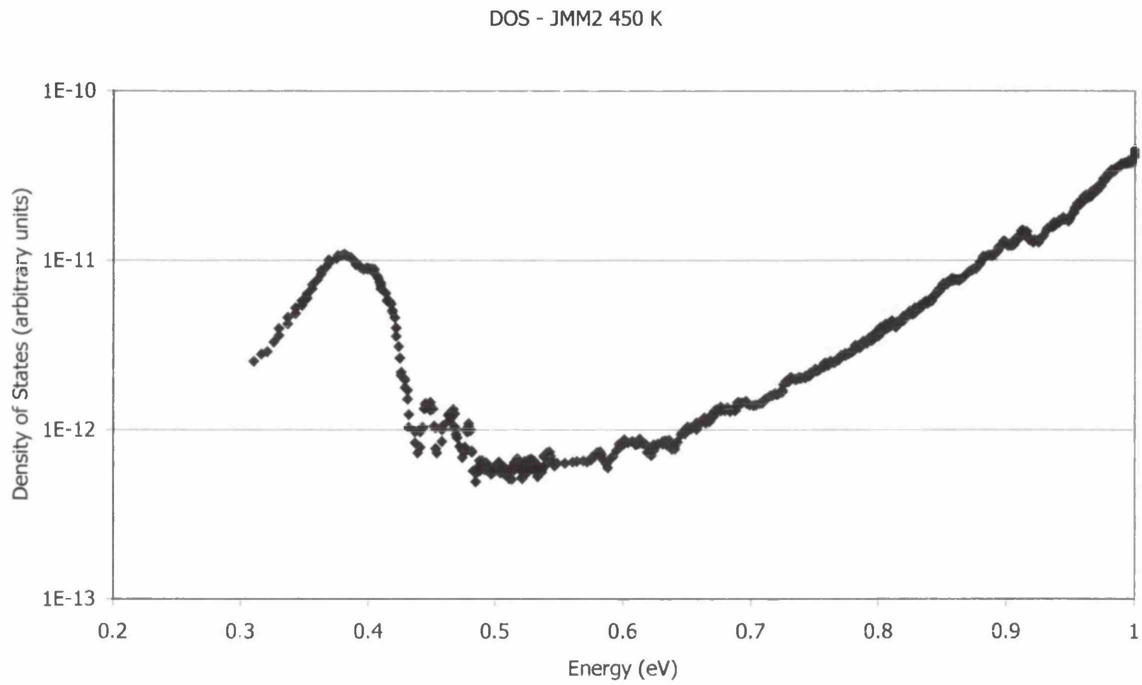

Figure 7.1.9: Calculated DOS for CVD Diamond Specimen JMM2 at 450 K.

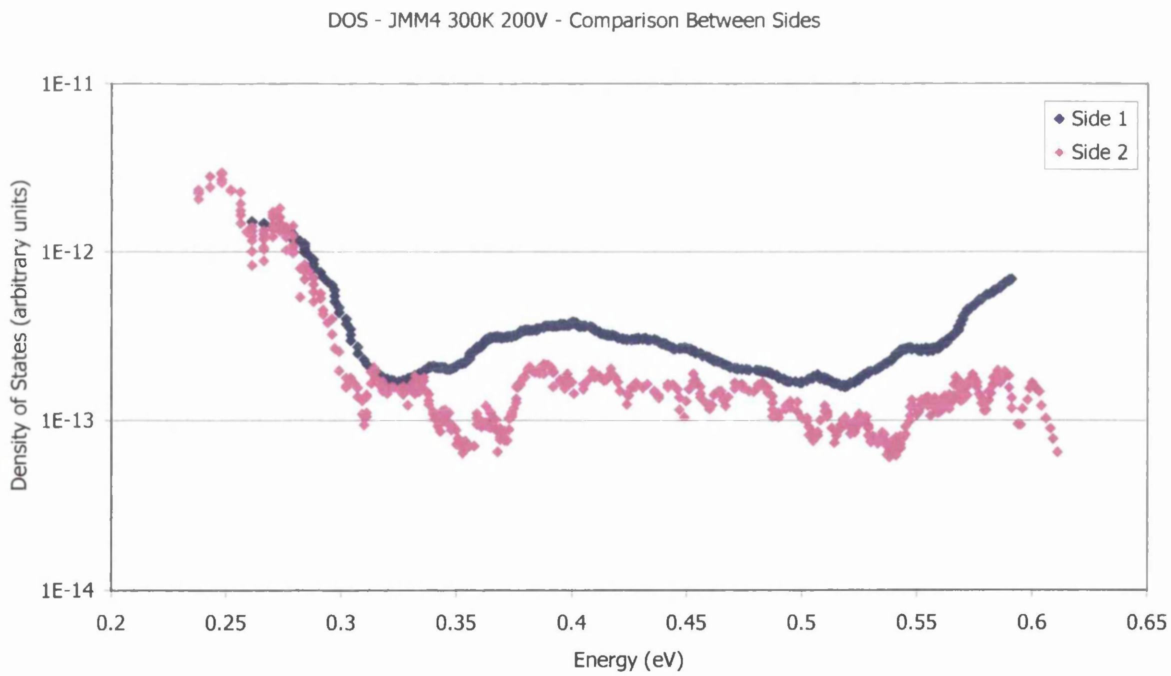

Figure 7.1.10: Calculated DOS for JMM4 Sides 1 & 2 at 300 K, 150 V.

Figure 7.1.10 displays the calculated density-of-states for polycrystalline CVD diamond specimen JMM4 for both the nucleation and growth surfaces. The increased noise observed on the data for the nucleation surface is likely to be the result of the increased grain boundary to grain size ratio, and thus the increased quantity of associated non-diamond (graphitic) defects.

It is clear that the three previously identified features are again apparent, to varying degrees, for drift away from both the growth and nucleation surfaces.

Although the conditions were significantly altered during growth, the data would seem to indicate that this did not have a marked impact on the transient photo-decay of the sample. However, this is not surprising taking into account the weakly absorbed illumination employed during this study (carriers would be generated throughout the material, and not just at the illuminated surface).

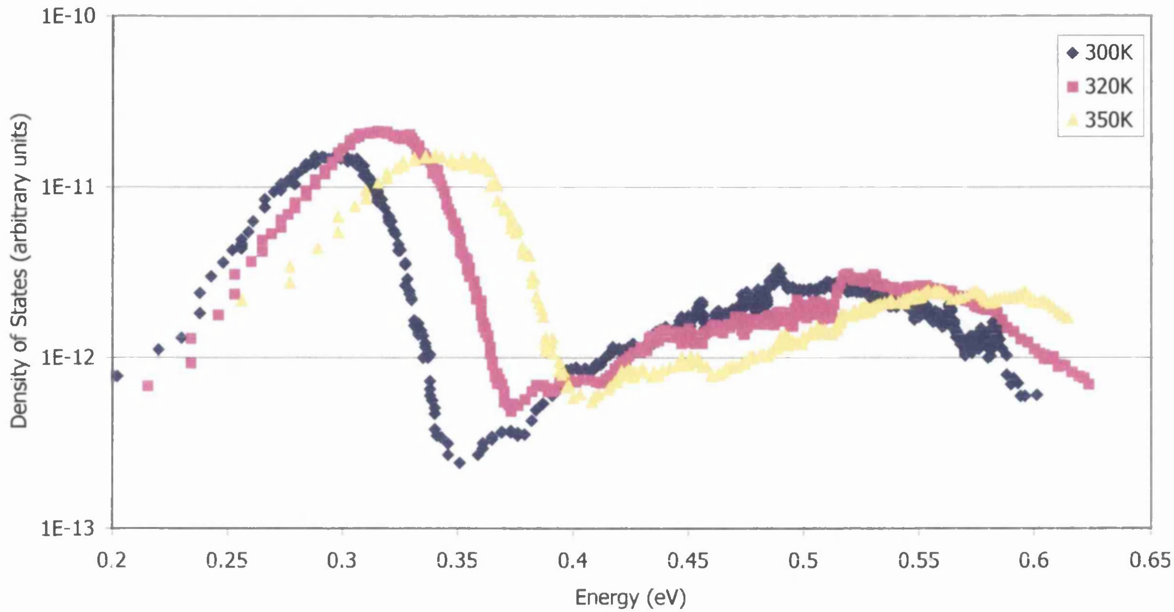

Figure 7.1.11: Calculated DOS for JMM5 at 300, 320 & 350 K.

CVD diamond specimen JMM5 has previously been identified as a material with a high degree of orientation with respect to its grain structure. Although the experimentally accessible energy range is more limited in this instance, it is evident from the data presented in Figure 7.1.11 that the two shallowest sets of localised states are present in this material. However, there is no evidence to suggest that the deepest feature identified in previous samples and normally centred at ~ 0.7 eV, is present in this sample. This suggests that this deepest feature is due to some nitrogen and / or disorder related defect, either not present in this specimen or present at low levels undetectable by the current procedure.

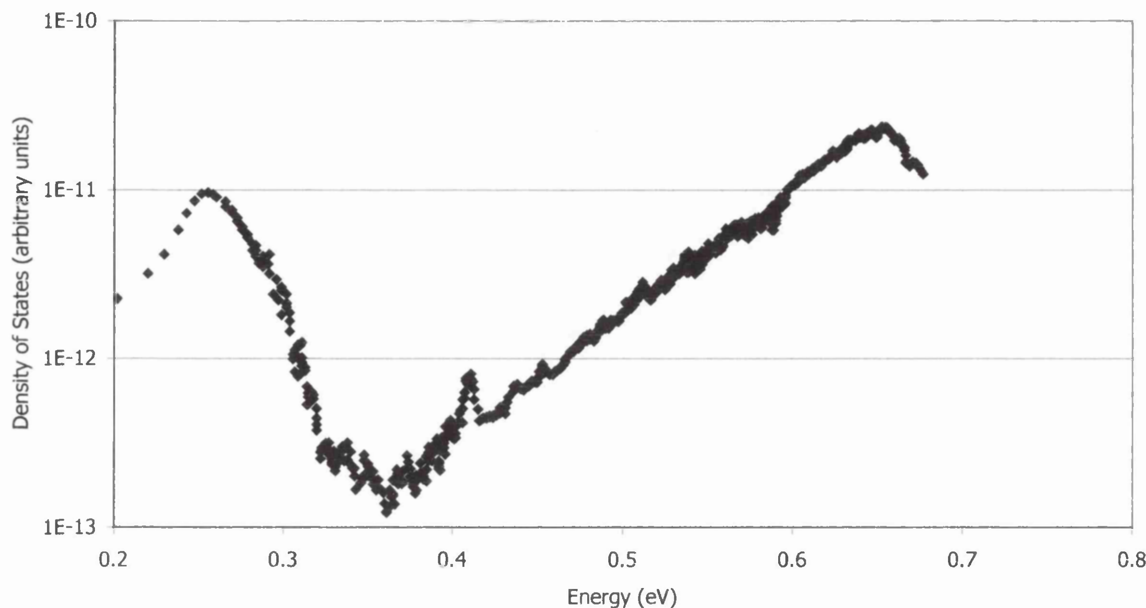

Figure 7.1.12: Calculated DOS for JMM6 at 300 K, 150 V.

CVD diamond specimen JMM6 was provided for comparison with JMM5. Both specimens were grown using identical conditions, except for the concentration of nitrogen, which was significantly greater in the case of JMM6.

The calculated density of states for JMM6 (Figure 7.1.12) is distinctly different from that for JMM5. Most notably, the deepest feature appears to have become so dominant that the middle one has become indistinguishable. Comparing the results for JMM5 and JMM6 and considering the differences in preparation and the resultant physical properties of the materials, it becomes clear that the deepest feature is related to nitrogen content. It is therefore likely that it is a result of aggregated nitrogen located at the grain-boundaries.

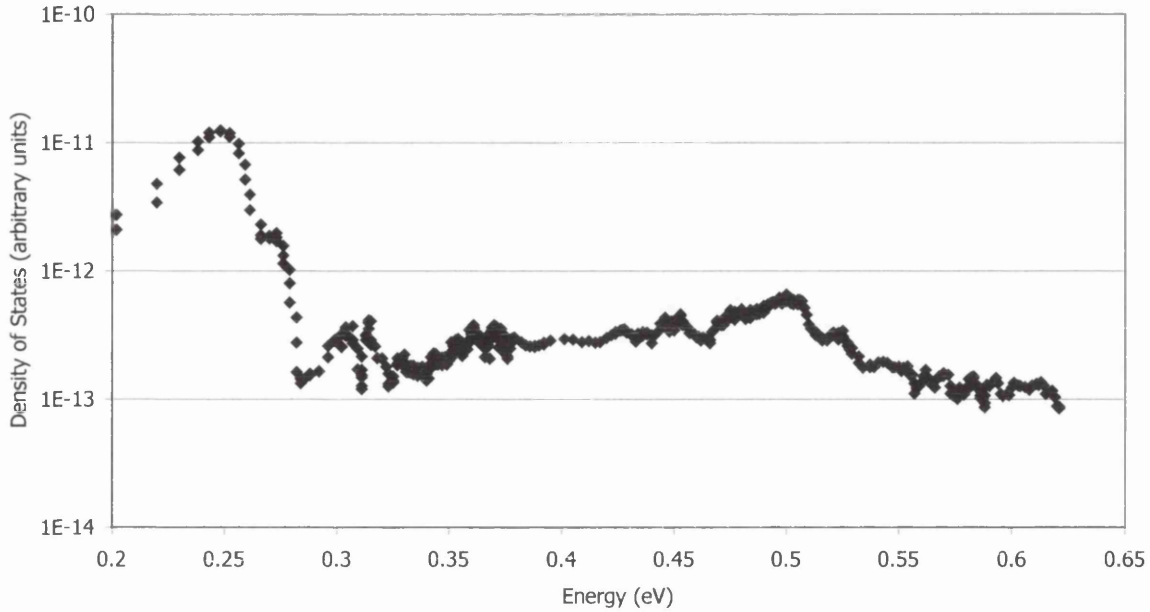

Figure 7.1.13: Calculated DOS for HPHT Type Ib Diamond at 300 K, 150 V.

Figure 7.1.13 above displays evidence that the two shallowest sets of states previously identified in most CVD diamond samples examined in this study are also present in the sample of synthetic HPHT type Ib diamond. The absence of the deepest feature would indicate similarities between the HPHT diamond and specimen JMM5. However, Type Ib diamond is characterised by its high nitrogen content, whereas JMM5 was known to have a low nitrogen content. From this, it can be deduced that the deepest feature is not only nitrogen related, but is indeed associated with nitrogen located at grain boundaries.

7.2 Residual Field Data

In a similar fashion to the TPC data, it is clear that the residual field persists over an extensive time range, as illustrated in Figure 6.2.1. Again, this infers that charge carriers have become trapped in significant concentrations of relatively deep localised states.

A complete numerical analysis of the measured behaviour is beyond the scope of the current investigation and would involve the capture into and release from various localised states of both species of carrier, their drift lengths between trapping events (which vary with time as the field decays), the ultimate recombination mechanism, etc. Nevertheless, a simple model has been developed which fits the experimental data surprisingly well and is described below.

Throughout the time period when the external field is present (t_a), the charge carriers will be injected from the electrode, and they will be free to interact with the trapping centres present in the material. Employing the same assumptions as for the 'thermalisation energy' concept, charge carriers will populate localised states according solely to their capture characteristics. However, as time passes from $t = 0$ to $t = t_a$ states shallower than the thermalisation energy (Eq. (4.3.1)) will have had sufficient time to release any trapped charge. Therefore, these states will have obtained quasi-thermal equilibrium with each other, whilst states deeper than the thermalisation energy will not have had enough time to release trapped charges. Thus, at a time t_a the energy distribution of the trapped charge $n(E)$ will be of the following form.

$$n(E) \approx C'''.N(E).f(E) \qquad (0 \le E \le E_a)$$

$$n(E) \approx C'''.N(E) \qquad (E \ge E_a)$$

Where, C''', is a constant and $f(E)$ is the Boltzmann occupation factor $\exp\left[\frac{-(E_a - E)}{k.T}\right]$, for the shallow equilibrated states.

Then, at a time t_d after termination of the applied field, it is assumed that all states shallower than $E_d = k.T\ln(\nu.t_d)$ have had sufficient time to release trapped charges, while no states deeper than this energy will have had time to do so.

Thus, the magnitude of the residual field (and therefore the size of the photo-induced discharge pulse, A) is assumed to be linearly proportional to the sum of the remaining deeper trapped charge at time t_d, i.e. to the integral of $n(E)$ over the energy range included in the model (E_d to 1 eV).

Based on the above premise, Figure 7.2.1 illustrates that the experimental data are more than adequately fitted to a function of the form:

$$A = 3.51\times10^{-3} + 6.28\times10^{-3}\exp\left(\frac{-t}{0.77}\right) + 8.71\times10^{-3}\exp\left(\frac{-t}{14.43}\right). \qquad \text{Eq. (7.2.1)}$$

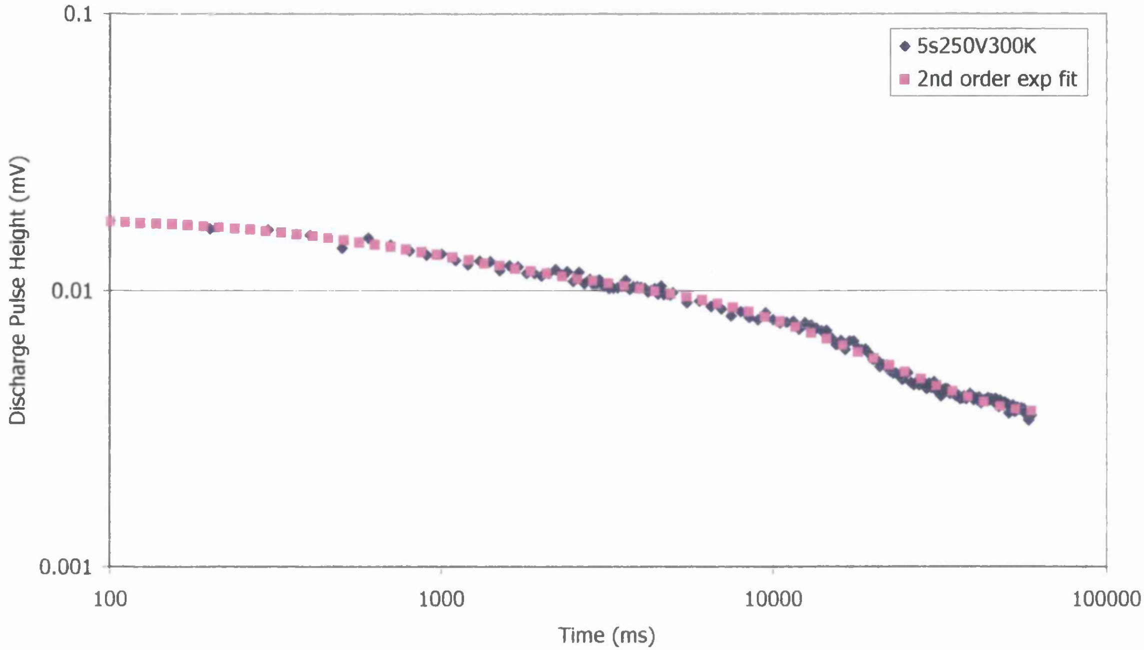

Figure 7.2.1: 2nd Order Exponential Fit to Experimental Results.

Therefore, at a qualitative level, the presence of such a reasonably sharply defined set of components infers an energy distribution of localised states possessing a reasonable degree of structure.

For the purposes of interpreting the observed decay behaviour, a simple model was adopted, similar to that employed in the transient photo-decay studies described previously. In this instance, the sum of a number of Gaussian features plus a number of deeper states was used to represent the density of localised states.

$$N(E) = N_1 \exp\left[\frac{-(E-E_1)^2}{W_1^2}\right] + N_2 \exp\left[\frac{-(E-E_2)^2}{W_2^2}\right] + N_3 \exp\left[\frac{-(E-E_3)^2}{W_3^2}\right] + N_d$$

Eq. (7.2.2)

Where, N_{1-3}, E_{1-3}, W_{1-3} are the densities, peak energies and widths of the individual components respectively and N_d is the total number of very deep states. All the deep states were positioned at an energy of 1 eV in the model, however this position has no real significance so long as these deeper states are located outside the experimentally accessible time-range. It is not necessary to include terms relating to very shallow states (e.g. an exponential bandtail) in this instance, as any trapped charge present in such features would have had sufficient time to be released before the minimum measurement time employed during this study.

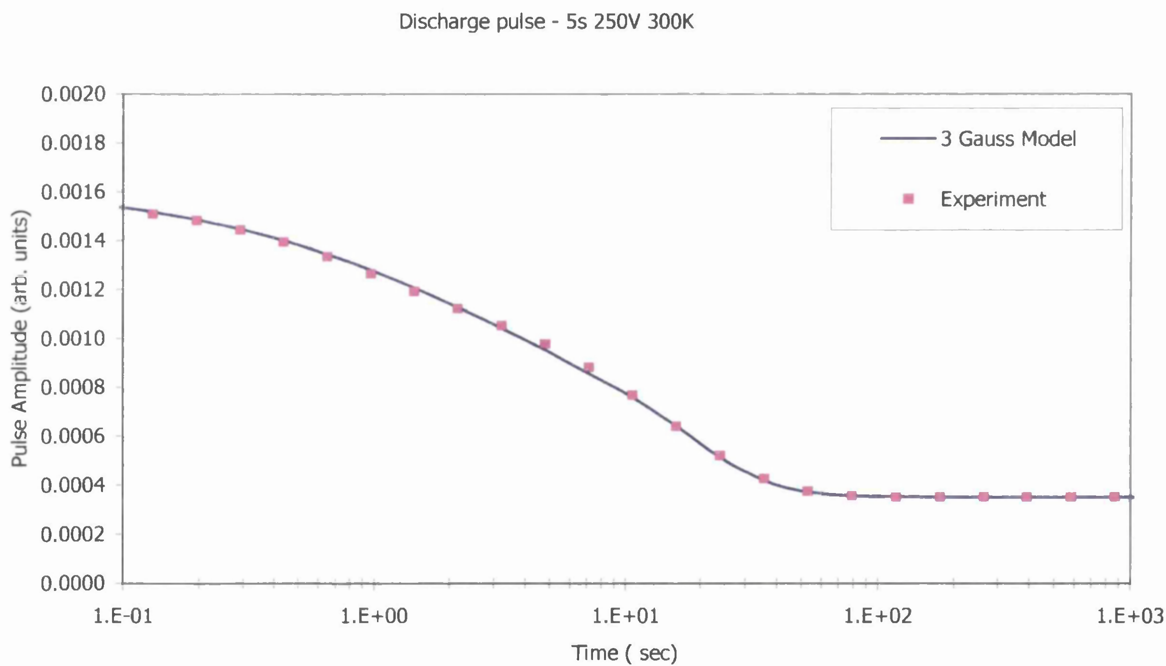

Figure 7.2.2: Time Decay of the Residual Field as Calculated from the '3 Gauss' Model Compared to the Fit to the Experimental Data.

Although this is a relatively simple approach to what would be expected to be an extremely complex decay process, the model fits the experimental data with a high degree of numerical accuracy. Figure 7.2.2 illustrates this by comparing Eq. (7.2.1)

with the predictions of the model described above. The fitting parameters in Equation (7.2.2) (Table 7.2.1 below) are subject to a low degree of tolerance, as small changes in the values results in large differences between the computed and measured values, demonstrating that selection of these parameters is far from arbitrary. For example, N_3 and E_3 determine the magnitude, sharpness and position in time of the feature located between 10 – 100 s, while N_2 and E_2 control the behaviour at short times (0.1 – 1 s). The values of N_1 and E_1 are admittedly more speculative, but nonetheless essential, as the presence of these shallow states is necessary to optimise the fit to the experimental data.

Table 7.2.1: Fitting Parameters for 3 Gaussian Model

Parameter	Amplitude N	Centre E	Width W
1	1.20×10^{21}	0.200	0.060
2	5.80×10^{10}	0.585	0.084
3	3.50×10^{9}	0.760	0.020

For the purposes of this study, E_1 and W_1 have been approximated so that E_1 is consistent with the conclusions of other authors [2] [5]. N_d is also somewhat speculative as it is primarily required to model behaviour at times greater than 100 s which exceed the current experimental range. The actual $N(E)$ for the data in Figure 7.2.2 is illustrated in Figure 7.2.3, where the red line illustrates the relative occupancies of the states immediately after a charging period of 5 s. At this stage, there appears to be reasonable qualitative agreement with the density of states

calculated from the transient photo-decay measurements. This is illustrated by the fact that the Gaussian components tend to be centred at broadly similar values for both the TPC and residual field diagnostic techniques. However, quantitatively, there are clear differences with respect to the heights and widths of the individual components. Nevertheless, agreement is considered relatively good taking in to account the very simplistic nature of the model adopted. This agreement infers that the same localised states are controlling both the transient photoconductivity and the decay of the residual field.

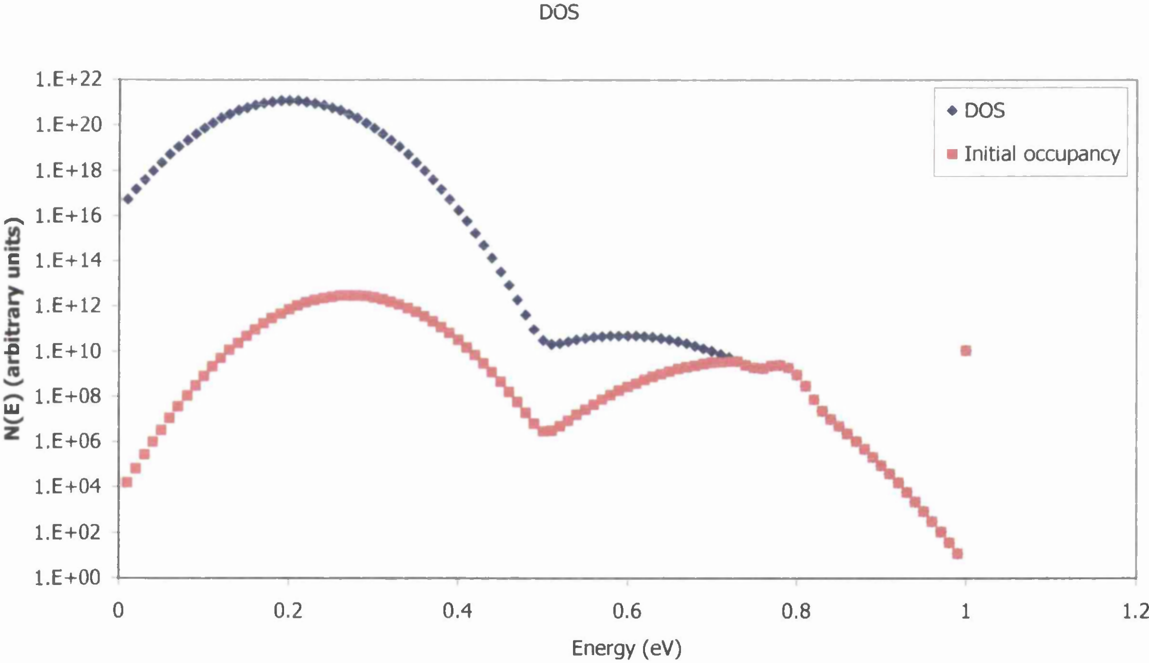

Figure 7.2.3: Energy Distribution of Localised States Developed to Model the Residual Field Decay.

UNIVERSITY OF WALES SWANSEA LIBRARY

References

[1] Marshall J M (2000) *Philosophical Magazine B* **80** 9 1705 – 1726.

[2] Nebel C E, Stutzmann M, Lacher F, Koidl P, Zachai R (1998) *Diamond and Related Materials* **7** 556 – 559.

[3] Marshall J M in *Thin Film Materials and Devices – Advances in Science and Technology – Proc. 10th International School on Condensed Matter Physics* (Eds. J M Marshall, N Kirov, A Vavarek, J M Maud, World Scientific, Singapore, 1999) p175.

[4] Marshall J M, Walters A S (1999) *Diamond and Related Materials* **8** 2118 – 2126.

[5] Main C, Reynolds S, Badran R I, Marshall J M (2000) *Journal of Applied Physics* **88** 1190-1192.

[6] Nebel C E, Münz J, Stutzmann M, Zachai R, Güttler H (1997) *Physics Review B* **55** 9786 – 9791.

8 CONCLUSIONS

This study has presented data concerning the first detailed analysis of the time dependences of the transient photoconductivity and the residual field after application of a voltage, for CVD and HPHT (Type Ib) synthetic diamond.

The data from both the transient photocurrent measurements and residual space-charge experiments have demonstrated the presence of various sets of localised defect states, located in significant concentrations at least over the experimentally accessible energy range, 0.2 – 0.8 eV. This conclusion is further strengthened by the good correlation between the density of states distributions calculated by the post-transit and the Fourier transform analysis procedures.

CVD diamond specimen JMM5 exhibits distinctly different transient photo-decay behaviour to the other CVD diamond specimens investigated during this study. The data is consistent with that observed by other authors for specimens that have been grown under low nitrogen conditions [1]. Such growth parameters result in a high degree of order with respect to the orientation of the individual grains. Therefore, it can be concluded that specimen JMM5 should be classified as highly orientated diamond (HOD). This material is different to the other CVD diamond specimens explored in this study, which are referred to merely as polycrystalline diamond (PD).

All PD specimens examined show the same general form of transient photo-decay. Although the analysis of the results indicates minor differences in the degrees of

structure in the calculated density of states, the energy positions of the identified features in the localised states do not seem to vary significantly between samples and are centred at approximately 0.25, 0.45, 0.72 eV at ~ 300 K. Additionally, it has been demonstrated that the calculated density of states can be effectively modelled by the summation of a number of Gaussian features.

Of the three sets of states identified to be present in PD, the data collected indicates that two of these are also present in the HOD and single-crystal HPHT diamond, specifically the two shallow features located at ~ 0.25 eV and 0.45 eV. This infers the third feature centred at ~ 0.72 eV is a result of the polycrystalline nature of the less ordered CVD material.

Samples JMM5 (HOD) and JMM6 (PD) are known to have been grown with different orders of magnitude of nitrogen concentration, but with otherwise identical growth conditions. The results of this study clearly demonstrate that nitrogen, either substitutional or located at grain boundaries, can have a profound effect on the photo-decay and therefore the electronic properties of CVD diamond. It is therefore reasonable to conclude that the deepest feature identified in PD is due to nitrogen defects located at grain boundaries, as this feature is not present in the nitrogen rich single-crystal HPHT Type Ib diamond. Additionally, the measurements for HPHT indicate that the two shallower sets of states are associated with the bulk material and not a result of the polycrystallinity of the CVD material.

The results of the modelling techniques detailed in this study strongly indicate that the same localised states identified from the transient photoconductivity measurements are also responsible for the decay behaviour of the residual space-charge phenomenon.

Overall, this study has demonstrated that transient photoconductivity and related studies present a powerful technique for the investigation of the defect states which may have a significant effect on the electronic properties of synthetic diamond. These defect states will have a critical role in determining synthetic diamond's effectiveness as an electronic material for commercial device applications.

References

[1] Nebel C E, Stutzmann M, Lacher F, Koidl P, Zachai R (1998) *Diamond and Related Materials* **7** 556 – 559.

9 SCOPE FOR FURTHER INVESTIGATION, AND LIMITATIONS

Firstly, it is clear that a more detailed comparison of CVD diamond specimens prepared under different, but known, conditions would be most instructive. In particular, investigations into the effect of compositional differences between samples should be investigated, in addition to other physical properties such as grain size. This would be a significant step forward on the road to developing CVD diamond material for electronic device applications.

More strongly absorbed excitation and/or the use of a thin, strongly absorbing 'launching layer' of other suitable material (e.g. a-Si:H or a-Se) on the upper surface of the specimens should aid in the identification of the relative contributions of electron and hole carriers to the photo-response characteristics. Additionally, in conjunction with the above improvements, the employment of thinner diamond films would allow significant numbers of carriers to complete their transits, potentially allowing direct determination of charge carrier mobilities and possibly lifetimes. The above improvements could also be combined with the addition of further amplification circuitry, which would again extend the experimentally accessible energy range.

Computer modelling studies of the transient photo-response of CVD diamond (currently at an early stage of development) may produce more detailed information about the distribution of localised states. Specifically, Monte Carlo simulation techniques [1] could be developed to compute transient photocurrent data for a

model density of states based on the initial findings of this study. The details of the model DOS can then be adjusted until computed and experimentally measured photocurrent evolution are in optimal agreement.

The comparison between synthetic Ib single-crystal diamond has already provided valuable information regarding the localised states affecting the electronic properties of diamond in general. It therefore seems reasonable to suggest that a further study of all the different types of both synthetic and natural diamond may well produce both scientifically and commercially important findings.

Given that it is now relatively straightforward to produce a p-type boron doped diamond material and that there is significant progress towards producing a phosphorus doped n-type material by CVD, it would be a logical progression from the current study to investigate the electronic properties of these potentially commercially important materials.

Options also exist for the investigation of other important and related materials by the techniques employed in this study. These include diamond like carbon (DLC) and microcrystalline diamond. This sort of investigation may lead to conclusions about the influence of graphitic carbon (largely located at grain boundaries) on the electronic properties of CVD diamond and associated materials.

In addition to the extension of the current techniques outlined above, the possibility also exists for the inclusion of other related techniques. These include constant

photocurrent measurements (CPM) and modulated photocurrent measurements (MPM), which have already been successfully employed by other groups on CVD diamond [2] [3] and other disordered semi-conductors [4].

There are two underlying assumptions that this study makes, which are discussed below. The first is that carrier movement takes place solely via 'trap limited band transport'. However, it is possible, and quite likely in the case of CVD diamond, that hopping transport (tunnelling between localised states in the band gap) may also play a significant role in the conduction process. At present however, the state of knowledge regarding the analysis of transient photoconductivity data does not include terms representing the role of hopping in the carrier transport process. However, computer modelling studies are currently being developed for other / ideal materials [5] that do take into account the role of hopping transport. It is therefore probable that with appropriate modification, these modelling techniques will be equally applicable to diamond and related materials and will lead to conclusions about the extent to which hopping transportation contributes to the overall conduction process.

The second major assumption is that the CVD materials behave in a homogeneous manner. That is the present study assumes that the defect related localised states are distributed evenly throughout the material. This clearly is unlikely to be the real case, as defect concentrations are likely to be far greater at grain boundaries and crystallite surfaces than inside individual grains. Additionally, any defects located inside the grain are likely to be of a significantly different nature than those located

at grain surfaces. However, as the techniques employed during this study explore a relatively large proportion of the sample at any one time, the results should be interpreted as an average value that takes into account the non-crystalline nature of the CVD material. Additionally, when the single crystal results were compared to the PD results, similar trends were identified. This would infer that defects associated with the polycrystalline nature of the CVD material do not necessarily have a significant impact on the electronic properties explored by this study. However, if small areas (e.g. ≈ grain size) of the CVD material were to be used for device fabrication, it is reasonable to expect that the grain boundaries and associated defects would definitely play a role in determining device performance.

It is the author's opinion that CVD diamond will one day become a widely used material for the production of certain electronic devices. However, theses applications will be limited to those requiring the unique and unrivalled combination of physical properties displayed by diamond. In particular, it seems reasonable to suggest that CVD diamond will be well suited to niche applications that necessitate high power handling, high frequency or high temperature operation as demonstrated by the prototype devices referred to previously. Another likely area of application for CVD diamond based devices is in situations where the operating environment is chemically or mechanically aggressive.

However, there are still several technological hurdles to overcome before CVD diamond can be fully exploited as an electronic engineering material. Currently, the volumes of material produced are too low to be commercially viable, although the

production of wafers up to six inches in diameter (and several mm thick) is now routine. Probably the most limiting factor at present is the absence of a suitable substrate for hetero-epitaxy for producing large single crystal wafers. However, research continues in this area and although unsuccessful at present the results are becoming increasingly promising. In addition to production considerations, it also needs to be highlighted that many of the properties that appear to make CVD diamond attractive for high-temperature device operation, are themselves temperature dependent. Hole mobility in particular decreases rapidly with increasing temperature ($\sim T^{2.8}$) [6]. This combined with other factors such as relatively ineffective p-type doping and slow, although promising, progress towards useful levels of n-type conductivity may mean we will have to wait some time for the commercial production of CVD diamond electronic devices. However, this study has provided significant data concerning the shallow defect states which will limit electronic conduction in both polycrystalline and single-crystal diamond. Data of this sort will be essential if any of the applications described above are to be eventually realised from synthetic diamond.

References

[1] Marshall J M, Walters A S (1999), *Diamond and Related Materials* **8** 2118 – 2126.

[2] Rohrer E, Graeff C F O, Janssen R, Nebel C E, Stutzmann M (1996), *Physical Review B* **54** 7874 – 7880.

[3] Nesládek M, Meykens K, Haenen K, Navrátil J, Quaeyhaegens C, Stals L M, Stesmans A, Iakoubovskij K, Adriaenssens G J, Rosa J, Vanêĉek M (1999), *Diamond and Related Materials* **8** 1480 – 1484.

[4] Reynolds S, Main C, Webb D P, Rose M J *in Thin Film Materials and Devices – Developments in Science and Technology* (eds. J M Marshall, N Kirov, A Vavarek, J M Maud) World Scientific (Singapore) 1998.

[5] Marshall J M (2000), *Philosophical Magazine Letters* **80** 10 691 – 701.

[6] Collins A T (1990) *in Diamond, Silicon Carbide and Related Wide Bandgap Semiconductors* (eds. J T Glass, R Messier and N Fujimori) Materials Research Society (Pittsburgh, Pennsylvania) 1990.

APPENDIX 1 LIST OF PUBLICATIONS

Localised States in CVD Diamond, Explored by Transient Photoconductivity and Residual Field Measurements, J M Marshall and A S Walters (1999), *Diamond and Related Materials* **8** 2118 – 2126.

Transient Photo-response and Residual Field Measurements in CVD Diamond, J M Marshall and A S Walters (2000), *Diamond and Related Materials* **9** 408 – 412.

BIBLIOGRAPHY

Diamond

Davies G (1984), Adam Hilger Ltd, Bristol, UK.

Diamond Films and Coatings

R F Davis ed. (1993), Noyes Publications, New Jersey, USA.

Synthetic Diamond: Emerging CVD Science and Technology

K E Spear and J P Dismukes eds. (1994), John Wiley & Sons, Inc, New York, USA.

Principles of Electrical Engineering Materials and Devices

S O Kasap (1997), McGraw-Hill, New York, USA.

Electronic Engineering Semiconductors and Devices

J Allison (1990), McGraw-Hill, London, UK.

Introduction to Solid State Physics

C Kittel (1971), John Wiley & Sons, Inc, New York, USA.

Handbook of Thin-Film Deposition Processes and Techniques

K K Schuegraf ed. (1988), Noyes Publications, New Jersey, USA.

Handbook of Chemical Vapour Deposition

H O Pierson (1992), Noyes Publications, New Jersey, USA.

Thin Film Diamond

A Lettington and J W Steeds eds. (1994), Chapman & Hall, London, UK.

Diamond, Silicon Carbide and Related Wide Bandgap Semiconductors

J T Glass, R Messier, N Fujimori eds. (1990), Materials Research Society,Pennsylvania, USA.

Diamond, SiC and Nitride Wide Bandgap Semiconductors

C H Carter Jr., G Gildenblat, S Nakamura, R J Nemanich eds. (1994), Materials Research Society,Pennsylvania, USA.

Diamond 1999 – 10th European Conference on Diamond, Diamond-Like Materials, Carbon Nanotubes, Nitrides & Silicon Carbide

J Robertson, G Gűttler, H Kawarada, Z Sitar eds. (2000), Elsevier Science S.A., Lausanne, Switzerland.